SANE's Measurement of the Proton's Virtual Photon Spin Asymmetry, A_1^p, at Large Bjorken x

Jonathan Robert Lee Mulholland
Milford, Delaware

B.A. Math, Physics, Saint Mary's College of Maryland 2004

A Dissertation presented to the Graduate Faculty
of the University of Virginia in Candidacy for the Degree of
Doctor of Philosophy

Derpartment of Physics

University of Virginia
May, 2012

Abstract

The experiment SANE (Spin Asymmetries of the Nucleon Experiment) measured inclusive double polarization electron asymmetries on a proton target at the Continuous Electron Beam Accelerator Facility at the Thomas Jefferson National Laboratory in Newport News Virgina. Polarized electrons were scattered from a solid $^{14}NH_3$ polarized target provided by the University of Virginia target group. Measurements were taken with the target polarization oriented at 80° and 180° relative to the beam direction, and beam energies of 4.7 and 5.9 GeV were used. Scattered electrons were detected by a multi-component novel non-magnetic detector package constructed for this experiment. Asymmetries measured at the two target orientations allow for the extraction of the virtual Compton asymmetries A_1^p and A_2^p as well as the spin structure functions g_1^p and g_2^p. This work addresses the extraction of the virtual Compton asymmetry A_1^p in the deep inelastic regime. The analysis uses data in the kinematic range from Bjorken x of 0.30 to 0.55, separated into four Q^2 bins from 1.9 to 4.7 GeV^2.

Contents

1 Introduction **1**

1.1 Scattering Experiments 2

2 Inclusive Lepton Scattering Formalisms **7**

2.1 Form Factors, Structure Functions, and Inclusive Scattering 7

3 Quark Parton Model **18**

4 Spin Asymmetry A_1^p **28**

4.1 Definition 28

4.2 Measurements and Models 30

5 Experimental Methods **35**

5.1 Overview 35

5.2 TJNAF 38

5.2.1 Injector 39

5.2.2 Accelerator 41

5.2.3 Beam Current Measurement 43

5.2.4 Beam Postion Monitoring 43

5.2.5 Beam Energy Measurement 44

5.2.6 Beam Polarization Measurement 44

5.2.7 Raster System 46

5.2.8 Chicane and Helium Bag 48

5.3 Target 49

5.3.1 Introduction 49

5.3.2 Dynamic Nuclear Polarization 50

5.3.3 Solid State Effect 51

5.3.4 Equal Spin Temperature Theory 53

5.3.5 Target Cryogenic and Microwave Setup 55

5.3.6 Polarization Signal Processing 58

5.3.7 Error Estimate 61

5.3.8 Lifespan of a Target Load 63

5.4 Data Acquisition System 65

5.4.1 Triggers 66

5.5 Front Tracker 67

5.6 Cerenkov Detector 69

5.7 BigCal 73

5.7.1 Clustering 74

5.7.2 Position Reconstruction 76

5.7.3 Energy Calibration 80

5.7.4 Energy Resolution 84

5.7.5 Resolution Calculation Results 85

5.7.6 Tracking through the field 88

6 Asymmetry Analysis: A_1^p 93

6.1 Calculation of A_1 from Asymmetries 93

6.1.1 Unpolarized Cross-Section 97

6.1.2 Asymmetries and Structure Functions 99

6.2 Calculation of

Physics Asymmetries $A_{\parallel}$ and A_{80° 100

6.2.1 Binning 101
6.2.2 Event Selection 104
6.2.3 Beam Charge 105
6.2.4 Livetime Correction 107
6.2.5 Radiative Corrections 111
6.2.6 Background Events 115
6.2.7 Packing Fraction and Dilution Factor 118
6.3 Combining Data Sets 125
6.3.1 Bin Averaged Kinematics 127
6.4 Calculation of A_1 132

7 Results and Discussion **137**
7.1 Systematic Error 137
7.2 A_1 Results 138
7.3 Discussion 146

A Target Lifetimes **150**

List of Figures

1.1 Structureless electron-proton elastic scattering. 4

1.2 Depiction of the angles that describe the scattering direction. 6

2.1 Diagrams that contribute to the electron vertex correction in electron-fermion scattering. 8

2.2 Inclusive scattering where the virtual photon interacts with the structure of the proton. 11

2.3 Data from SLAC illustrating the transition into deep inelastic scattering. 12

2.4 Illustration of the optical theorem. 13

3.1 $F_2^p(x, Q^2)$, the proton unpolarized structure function. 19

3.2 Baryon decuplet (angular momentum 3/2). 20

3.3 Baryon octet (angular momentum 1/2). 21

3.4 Elementary particles, consisting of leptons, quarks, and gauge bosons. 22

3.5 Graph for the interaction of a photon (momentum q) with a parton carrying momentum k inside a nucleus with momentum p. 24

4.1 World data for A_1. 33

4.2 F_2^n F_2^p ratio from BCDMS measurement. 34

5.1 Picture of BETA from the side. In this picture, the beam dump is to the left. 36

5.2 Graphical overhead view of the experiment. 37

5.3 Jefferson Lab accelerator and experimental halls. 38
5.4 Energy levels for strained GaAs. 40
5.5 Per run beam polarization as given by a fit to the Møller data. 46
5.6 Beam Raster ADC histogram. 47
5.7 Target ladder picture. 47
5.8 Zeeman energy levels for electron spin states and coupled electron-proton spin states. 51
5.9 Illustration of the population of the electron energy levels with various spin-spin reservoir temperatures. 53
5.10 Cross Section schematic of the UVA target used for SANE 56
5.11 Target ladder picture. 58
5.12 NMR circuit including the LRC components and the Q-meter used for polarization measurement [1]. 59
5.13 Stages of NMR signal processing. 61
5.14 Processed NMR signal. 62
5.15 A histogram of all run polarization values. 63
5.16 Polarization assigned to each run in the analysis. 64
5.17 Calibration constants plotted by the target load index. 65
5.18 Close up of tracker location. 68
5.19 Sketch of intended function of the front tracker. 69
5.20 Temple University fabrication diagram of the cerenkov detector. . . . 71
5.21 Events binned by Big Cal cluster location with different cuts on activated cerenkov PMT. 72
5.22 Cluster routine illustration. 75
5.23 A graph of a simple neural network. 78
5.24 Complex neural network graph. 79
5.25 SANE calorimeter nerual network. 81

5.26 Calorimeter position resolution plots. 82

5.27 Invariant mass spectrum of 2 cluster events after initial event selection. 86

5.28 The pion decay product separation angle vs the parent pion energy. . 87

5.29 Selected pion distribution for resolution study. 90

5.30 Energy spectrum of the second cluster after appropriate energy and angle cuts. 91

5.31 Two curves, the sum of which were used to fit the spectrum in figure 5.30. 91

5.32 Energy resolution curves for each configuration. 92

6.1 Diagram of inclusive scattering. 94

6.2 Definition of scattering angles and vectors. 95

6.3 Kinematic binning 180° target orientation. 103

6.4 Kinematic binning for 80° target orientation. 103

6.5 BigCal-Cerenkov correlation cut. 105

6.6 Charge per helicity asymmetry. 106

6.7 Asymmetry illustrating charge normalization swap. 108

6.8 Asymmetry illustrating no charge normalization swap. 109

6.9 Recorded triggers versus scaler counts 110

6.10 Difference in area between fit lines (y-axis) as κ (x-axis) varies. 111

6.11 χ^2 (y-axis) of the positive scaler fit as κ (x-axis) varies 111

6.12 Illustration of radiative shift in W due to shift in E. 113

6.13 Illustration of radiative shift in W due to shift in E. 113

6.14 Correction factor f_{rc} for the first Q^2 bin. 115

6.15 Correction factor A_{rc} for the first Q^2 bin. 115

6.16 Correction factor f_{rc} for the second Q^2 bin. 115

6.17 Correction factor A_{rc} for the second Q^2 bin. 115

6.18 Correction factor f_{rc} for the third Q^2 bin. 116

6.19 Correction factor a_{rc} for the third Q^2 bin. 116

6.20 HMS Data and HMS Monte Carlo simulation for carbon run# 72977. 122

6.21 Dilution factors calculated using the SLAC structure function fits with a nominal 50% packing fraction. 125

6.22 Bin distribution averages of scattered electron energy (E') for 4.7 and 5.9GeV data. 128

6.23 Bin distribution averages of polar scattering angle (θ) for 4.7 and 5.9 GeV data. 129

6.24 Bin distribution averages of Q^2 for 4.7 and 5.9 GeV data. 130

6.25 Bin distribution averages of W for 4.7 and 5.9 GeV data. 131

6.26 Coefficients for construction of A_1 from asymmetries. 136

7.1 Count asymmetries for each run. Perpendicular 4.7 GeV data. 140

7.2 Count asymmetries for each run. Perpendicular 5.9 GeV data. 140

7.3 Count asymmetries for each run. Parallel 4.7 GeV data. 141

7.4 Count asymmetries for each run. Parallel 5.9 GeV data. 141

7.5 The run averaged physics asymmetries binned in x and Q^2. Parallel 4.7 GeV data. 142

7.6 The run averaged physics asymmetries binned in x and Q^2. Parallel 5.9 GeV data. 142

7.7 The run averaged physics asymmetries binned in x and Q^2. Perpendicular 4.7 GeV data. 143

7.8 The run averaged physics asymmetries binned in x and Q^2. Perpendicular 5.9 GeV data. 143

7.9 Virtual Compton asymmetry A_1 separated by color into Q^2 ranges. . 144

7.10 Contributing terms to A_1 from the parallel and perpendicular proton asymmetries. 144

7.11 Result from this work alongside the wolrd's data for A_1. 145

7.12 Results with a nu dependent background dilution corrections. 146

7.13 SANE preliminary results alongside other A_1 measurements. 148

A.1 Target Load 1 lifespan. 150

A.2 Target Load 2 lifespan. 151

A.3 Target Load 3 lifespan. 151

A.4 Target Load 4 lifespan. 152

A.5 Target Load 5 lifespan. 152

A.6 Target Load 6 lifespan. 153

A.7 Target Load 7 lifespan. 153

A.8 Target Load 8 lifespan. 154

A.9 Target Load 9 lifespan. 154

A.10 Target Load 10 lifespan. 155

A.11 Target Load 11 lifespan. 155

A.12 Target Load 12 lifespan. 156

A.13 Target Load 13 lifespan. 156

List of Tables

5.1 Chicane Settings for different beam energies. 49

5.2 Table of critical energies for Cerenkov emission in the detector tank (N_2 at 1 atm). 71

5.3 Percent Energy Resolution for each Experimental Setting. 88

6.1 Experiment Settings Date and Run Breakdown 103

6.2 Material thicknesses that contribute to radiative effects. 116

6.3 The contribution to the systematic error from the positron background. 118

6.4 Packing fractions and simulated and experimental yield for sample ammonia runs. 123

6.5 The packing fractions calculated for various runs. 124

6.6 Data table structure for run-level data processing. 134

Acknowledgments

To repeat a metaphor that, I am sure, has been used thousands of times in dissertation acknowledgments: completing a thesis is a marathon–not a sprint. Maybe it was more so in my (and my fellow graduate student in the trenches, James Maxwell's) case than in others. Due to a seemingly impossible number of delays, complications, and problems– many of which seemed insurmountable– the experiment and the analysis were far more arduous and took far longer than anyone had expected.

Nuclear physics is by no means easy. Obviously, mastering the technical aspects and the physical principles that were needed to make SANE a success required a lot of hard work and aptitude. However, in my opinion, skills and knowledge were not the most important factor in the success of SANE. More important to the success of such an ill-fated experiment was the willingness of the collaboration members to bear disappointment and weather frustration over and over again and yet still press on. For me, the fortitude that allows me to so persevere cannot be maintained in a vacuum and nourished only by a sense of duty or desire for personal gain. The ability to push on and remain at best guardedly optimistic or at worst doggedly persistent in the face of extreme difficulty was dependent on a support network of people around me. Some members of the collaboration were sources of constant encouragement, interested in figuring out what would work, while everyone else was dwelling on what would not. In this regard, Mark Jones and Oscar Rondon stand out in my memory of the experiment. During the experiment, James Maxwell was a constant companion-at-arms during the sometimes twenty-four hour work day. It turns out commiseration is not synonymous with despair, and it can be in some cases necessary and healthy. I received much love and support from my friends and family, especially from my parents, Ralph and Vicki Mulholland, and from my partner Katharina Richard. The sense of self worth that comes from being cared for is invaluable when faced with adversity. The difficulty of this experiment has made it clear to me that any and all

enterprises rise or fall based not only on the capability of the people involved, but also on the quality and character of those people–as well as the network of people to which they are connected.

In my education and training, Donal Day, Donald Crabb, and Oscar Rondon were absolutely invaluable. Between the three of them I was privileged to have access to a body of knowledge and experience that is both elite and unique. The senior graduate students in the UVA target group upon my entry, Josh Peirce and Nadia Fomin, were also indispensable with respect to my development as a physicist.

The work that made SANE a success was done by many people. The SANE collaboration, including especially the spokespeople, were the primary actors. The collaboration as a whole holds responsibility for the experiment's design, implementation, and subsequent analysis. The Jefferson Lab staff, notably the in-house target group, were absolutely essential to the experiment's execution. If I have neglected to mention anyone, I beg your forgiveness.

I take a moment now to reiterate a point and indulge in pedantry. In my graduate career, I have seen physicists participate in inexplicably self-centered behavior. I have received inscrutable communications and been confronted with bizarre resistances to cooperation. Science and, in some cases, the fair treatment of other people have been regarded as secondary to personal gain and advancement. Not only is this behavior repugnant, but it is self defeating. The fact that SANE collected *any* data at all depended on exactly the opposite qualities that are displayed by some members of physic departments and communities. Effective communication, cooperation, and, above all else, regard for others transformed SANE from a failure into a success. I thank everyone in the collaboration that displayed those qualities. I will continue to practice including those qualities in my own work, and ask forgiveness for those times that I fall short of the ideal.

Chapter 1

Introduction

Like curious children taking apart a watch, physicists over the years have broken up the matter the universe is composed of into smaller and smaller pieces. As in disassembling a watch, its not until we can see all the pieces individually that we begin to suspect how the composite whole comes together to function. A child disassembling a watch has the advantage of being able to tell when all the parts have been deconstructed into their indivisible parts. Not so for physicists. Several times it was thought that science had uncovered the basic building blocks of the universe.

In the 1800's, science raced to construct a table of fundamental elements from which all materials were composed. Upon closer inspection, to continue the watch analogy, gears within gears appeared. The very structure of the periodic table suggested that the atoms the elements were composed of could be broken down into smaller units. Atoms were discovered to be composed of protons, neutrons, and electrons. Later, it was discovered that even the tiny protons and neutrons possessed an internal structure. The parton model was proposed to explain scattering phenomena that indicated sub-nucleonic particles. Although the progression of the inquiry into the nature of matter suggests an infinite regress– or perhaps ingress, for now science has settled at the partonic level.

Today the parton model has evolved into the quark model, in which the nucleons are composed of quarks and gluons governed by color forces described by *quantum chromodynamics*. The structure of the proton– how the quarks are organized and move within the proton, is the topic of this work. That structure can be probed and information about it inferred from the scattering of electrons from protons.

The experiment described in this thesis is just such a scattering experiment. The experiment was labeled as E-07-003 and executed at the Jefferson Lab National Accelerator Facility (JLAB). It is nicknamed and hereafter referred to as SANE– Spin Asymmetries of the Nucleon Experiment. Herein is described the motivations, the techniques, and the results of one of the analyses SANE was designed to facilitate– namely the determination of the virtual Compton proton asymmetry, A_1^p.

1.1 Scattering Experiments

When conducting measurements, it is necessary to use a measuring tool on the scale of that which is being measured. For example, one should use a yardstick to measure the length of a bolt of cloth that is to be cut– not a jeweler's caliper. One could use a caliper, but it would be difficult and time consuming. As length (or energy) scales of the object or phenomena being measured increase or decrease dramatically, choosing the correct instrument of measurement becomes a necessity rather than a convenience. To examine fingerprints, one needs a magnifying glass. The viewing of immune cells and their inner workings requires a microscope.

Progressing to even smaller length scales requires one to consider not only the measurement apparatus, but also the medium with which the apparatus functions. Microscopes and magnifying glasses rely on the scattering of light off an object, and the subsequent gathering of that light. If one wants to delve into smaller and smaller length scales–into the worlds of crystalline structure, atoms, and nuclei, one needs to

be aware that light will only resolve objects of a size that is on the order of the light's wavelength.

In 1911 the Rutherford backscatter experiment, overseen by Ernest Rutherford and executed by Marsden and Geiger, determined that the size of the atomic nucleus of gold is no larger than 10^{-14} m. The charge and weight of the nucleus was known; so they postulated that the size of the individual charge carriers is on the order of a femtometer, which is close to the contemporary measurement of 0.877 ± 0.007 fm for the charge radius of the proton [2]. In order for light to resolve an object that small, one would need wavelengths on the order of a femtometer or smaller. Light of this wavelength has a frequency around 10^{22} Hz, and energy ten orders of magnitude greater than that of x-rays.

Rather than attempt to harness such high energy light, nuclear physicists take advantage of that fact that matter also has a wavelength associated with it. This wavelength, called the de Broglie wavelength, is inversely proportional to the momentum of a particle:

$$\lambda_{\text{deBroglie}} = \frac{h}{p}. \tag{1.1}$$

Like light, a particle, when scattering from an object, resolves structure on the order of its wavelength.

High energy particles can have extremely small de Broglie wavelengths, and charged particles are much easier to generate and direct than photons. By using these high energy particles in accelerator experiments, an experimentalist can choose the length scale being probed by adjusting the parameters of the accelerator that determine the particle energy and momentum.

Having an appropriately scaled measurement instrument is not enough. It is necessary to have a functional theory of interaction to help one understand and to put into context the quantities gleaned by one's device: enter relativistic quantum field theory (RQFT). RQFTs provide physicists a framework to think about and

understand particle interaction. Consider quantum electro-dynamics (QED), which is a subclass of the larger category of RQFTs. The QED electron-proton scattering process can be represented by a diagram (Fig. 1.1). In the figure, an incoming electron (e^-) approaches the proton (p^+) and emits a photon (γ) which changes the electron's energy, scattering it. The proton absorbs the photon; this changes the proton's direction as well.

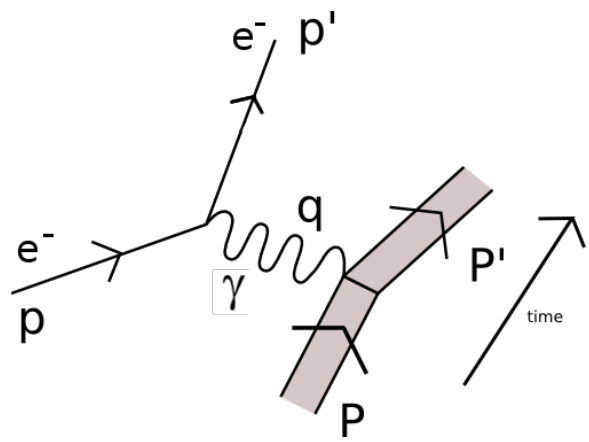

Figure 1.1: Structureless electron-proton elastic scattering. An electron incoming with momentum p^μ scatters from proton with initial momentum P^μ. The recoiling particles have corresponding momenta p'^μ and P'^μ; $q^\mu = p^\mu - p'^\mu$

.

In this model the electron does not interact directly with the proton. The electron-nucleon interaction (and indeed according to QED any interaction via the electromagnetic force) is mediated by a photon. The photon energy is determined by the change of energy of the scattered electron, this in turn determines the resolving power of the experiment. For an incoming electron of energy 5 GeV that scatters and is detected with energy 1 GeV, one calculates the wavelength of the mediating photon to be of order 10^{-17} m– small enough to resolve the proton within the nucleus and even small enough to interact with whatever substructure the proton has. The change in energy of the scattered electron gives the experimenter a dial to adjust what size features of the proton one is probing. The scattering of a beam of mono-energetic electrons from a target produces scattered electrons at a wide variety of angles and energies.

By quantifying the rates of interaction (i.e. counting scattered electrons) at different mediating photon energies, the experimenter can establish probability of interaction at different length scales within the proton. This scale-dependent probability of interaction is effectively a roadmap of the features of the proton. The inclusive scattering this work is concerned with uses the quantities shown in the Fig. 1.2 to describe the measurement.

To first order in QED, the scattering of an electron off of a proton can be approximated by the differential Mott cross-section. The differential cross-section is a function that describes the probability of an event that results in an electron being detected at a particular energy and angle relative to the incoming beam. The Mott formula in particular gives the cross section for the scattering of a spin 1/2 particle interacting with a massive target through a Coulomb potential.

$$\frac{d\sigma}{d\Omega} = \frac{\alpha^2}{4E^2}\frac{(1-\beta^2\sin^2\frac{\theta}{2})}{\sin^4\frac{\theta}{2}}, \tag{1.2}$$

The incident electron's energy is E and $\beta = \frac{v}{c}$ is the ratio of the incoming electron velocity to c, the speed of light. The fine structure constant, α, is related to the strength of the interaction between the electron and proton. The scattering angles are shown in Fig. 1.2. The above equation provides a quantification of the process pictured by Fig. 1.1. In the limit that the particles being measured are highly relativistic, which is the case in high energy electron scattering experiments like SANE, the Mott cross section can be written

$$\frac{d\sigma}{d\Omega} = \frac{\alpha^2}{4E^2}\frac{\cos^2\frac{\theta}{2}}{\sin^4\frac{\theta}{2}}. \tag{1.3}$$

There is a single photon mediating the interaction, meaning that the interaction between the two particles is strictly electromagnetic in nature. If one conducts an experiment with low resolution (ie. the 4-momentum transfered by the virtual photon

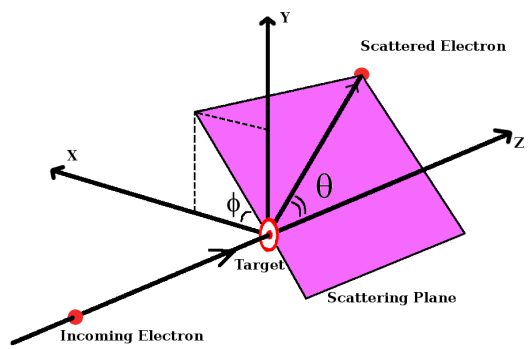

Figure 1.2: Depiction of the angles that describe the scattering direction. Polar angle θ and azimuthal angle ϕ along with the z axis (initial direction of electron momentum) define a scattering plane.

stays relatively low, and consequently probes only the gross features), an experimenter will find that the rates in her detectors match those predicted by the Mott cross-section. As the resolution of the probe increases, the behavior of the scattered particles will deviate from the Mott formula. These deviations are indicative of the substructure of the nucleon, and require a more general treatment than a two vertex QED calculation.

A vertex in which the nucleon absorbs a photon and changes momentum is clearly an oversimplification. Two subjects need to be discussed in order to understand the measurement SANE made. The first is how structure functions and form factors are used to parameterize and describe unknown interactions. Structure functions are used to generalize the photon-proton vertex to encompass more than a simple QED photon exchange with a point-like particle. Secondly, one needs an understanding of inclusive measurements and how the structure functions calculated from the data relate to the nature of the nucleon. These issues are discussed in chapters 2 and 3. Chapter 4 discusses the quantity A_1^p, the virtual photon asymmetry of the proton, the measurement of which is the main topic of this thesis. The methods of measurement are detailed in chapter 5. Following that are the chapters describing the data analysis, results, and the conclusions that can be drawn from this body of work.

Chapter 2

Inclusive Lepton Scattering Formalisms

2.1 Form Factors, Structure Functions, and Inclusive Scattering

In QFT, the cross section for a process can be written as the product of phase space factors, momentum and energy conserving delta functions, and what is called an *invariant matrix element*. All quantities are averaged over the appropriate momenta and averaged(summed) over initial(final) spin states. The only part of the cross section which is dependent on the physics of the process being examined is the invariant matrix element, $\mathcal{M}$. Therefore, the discussion will focus on calculating $\mathcal{M}$. By knowing $\mathcal{M}$, one can immediately obtain a cross section. The matrix element for an electron scattering off of a heavy point-like fermion is

$$\mathcal{M} = e^2[\bar{u}(p')\gamma^\mu u(p)]\frac{1}{q^2}[\bar{u}(P')\gamma_\mu u(P)], \tag{2.1}$$

where $u(k)$ is the Dirac spinor for a fermion with 4-momentum k. Using this matrix element to calculate the cross section returns, as expected, the standard Mott cross section. The first factor comes from the electron-photon vertex in Fig. 1.1, and the second from the photon-proton vertex.

One might wonder if the interaction could take a different form. Consider only the electron-photon vertex; one can think of it as the first order term in a perturbation series. Including higher order terms in perturbation theory corresponds to including more diagrams as shown in Fig. 2.1. Each extra diagram includes more virtual photon exchanges in the e-γ vertex, and each new diagram introduces another factor of α, the electromagnetic coupling constant. The coupling constant is $\alpha \approx 1/137 < 1$, so each term in the series contributes less to the total sum.

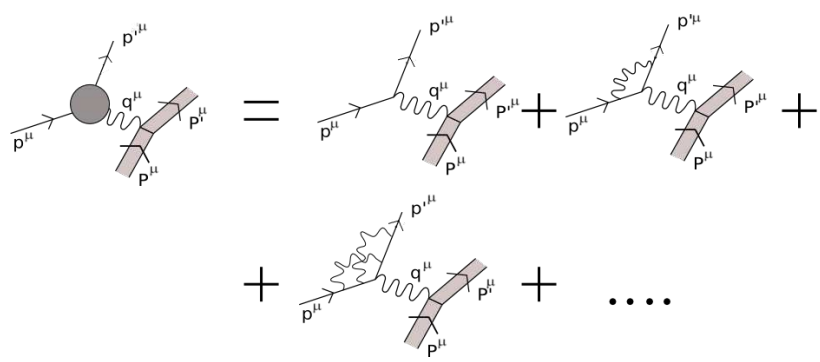

Figure 2.1: Diagrams that contribute to the electron vertex correction in electron-fermion scattering.

The right hand side of the equality in Fig. 2.1 can be written explicitly using the Feynman rules for QED, if one picks an order in α at which to terminate the sum. Or if one want to represent the sum over all orders, you can write the vertex on the left hand side as an unknown function Γ^μ, writing the matrix element as

$$\mathcal{M} = e^2[\bar{u}(p')\Gamma^\mu(p,p')u(p)]\frac{1}{q^2}[\bar{u}(P')\gamma_\mu u(P)]. \tag{2.2}$$

While one cannot explicitly calculate $\Gamma(p,p')$ without specifying an order in α, arguments based on Lorentz invariance, parity, and the Ward identity can be used to

show that it must be written in the following form:

$$\Gamma^{\mu} = \gamma^{\mu} f_1(q^2) + \frac{i\sigma^{\mu\nu} q_{\nu}}{2m} f_2(q^2). \tag{2.3}$$

The functions, $f_1(q^2)$ and $f_2(q^2)$, are known as form factors. They are parameterizations of the unknown correction to the electron vertex. The experimenter can now measure the q^2 dependence of the cross section in order to extract f_1 and f_2 from the data. Once data on f_1 and f_2 have been collected, one can use that data to calculate electron properties. For example, $f_2(0)$ is related to the anomalous magnetic moment of the electron, the precise calculation of which and subsequent experimental verification is one of the great triumphs of 20th century physics.

The above example illustrates how one can express phenomenology due to unknown processes or interactions as a general function of kinematics in the cross section formula. In the case of electron scattering, this function can be calculated by extending the QED calculation to higher orders of perturbation in α. For the nucleon, the exact form of interaction (which is very complicated due to the composition of the nucleon), is unknown, but the interaction can still be measured and explored through the use of form factors because of their generality. The structure functions, which the SANE data allow access to, are the inelastic analogs of the form factors and will be explored later.

This chapter will discuss the basics of inclusive electron scattering. Inclusive in this case means that the final state of the target is not detected, and consequently the measurement *includes* all the different reactions of the electron with the target, $ep \rightarrow e'X$ (where X is any final state). If one keeps the energy transfer low enough, that energy is absorbed as a change in momentum; the final state is strictly determined by the kinematics of the electron. That is, the electron and hadron are elastically scattered off of one another. If the energy transfer is increased, it is possible to excite

nucleon resonances, induce pion production or a range of other processes. A scattering process in which one of the latter reactions occur is referred to as being inelastic. In either regime, data is commonly presented and analyzed using the inclusive variables presented below. Refer to Fig 2.2 for a diagram of the reaction.

Let p^μ be the incident electron's four momentum, and p'^μ be the detected scattered electron's four momentum. Take the z-axis to be in the direction of $\vec{p}$ (i.e. the z-axis is parallel to the experiment's electron beam). The angle between the scattered electron's 3-momentum and the z-axis is θ. The difference in the electron's four momenta is $q^\mu = p^\mu - p'^\mu$, and one uses the following definitions:

$$Q^2 = -q^\mu q_\mu, \tag{2.4}$$

$$\nu = E - E' \equiv p^0 - p'^0,$$

$$x_{bj} = \frac{Q^2}{2M\nu}, \text{ and}$$

$$W^2 = 2M\nu + M^2 - Q^2.$$

The square of the momentum transfer, Q^2, is the mass of the virtual photon that interacts with the hadron. The photon is off-shell and not required to have $Q^2 = 0$. As the mass of the particle mediating an interaction is related to the range of the interaction, Q^2 indicates the length scale over which the probe is sensitive in the hadronic system. As Q^2 increases, the length scale of the interaction shrinks. The energy transfer ν is the energy carried by the virtual photon and can be thought of as the resolution of the virtual probe, much as the frequency of real light in microscopy is related to the optical resolution of the device. The constructed variable x_{Bj} is called the Bjorken x scaling variable. In this text x will be used interchangeably with x_{Bj}, and it x will always refer to the Bjorken x variable unless otherwise specified. Bjorken x will be shown later to be related to the momentum carried by the quarks within the

hadron in the Bjorken scaling limit. W is the missing mass– i.e. the invariant mass of the undetected final hadronic state, which can be calculated simply from 4-momentum conservation, given the initial kinematics and the electron's final momentum. When $W = M$, the scattering is elastic–the final hadronic state is a recoiling proton. There exists a hierarchy of resonances and hadronic states, such as the Roper resonances and the Δ states to which the nucleon can be excited. These particles and states, when plotting scattering cross sections as a function of W, are seen as peaks centered around their masses. The kinematic region in which these peaks exist is known as the "resonance region." As W increases, the resonance phenomena become less common, and the cross section smooths as a continuum of reactions begin to contribute and the proton breaks up during the reaction. The region in which this continuum of states contribute and the resonances disappear is called the "deep inelastic scattering"(DIS) region. Fig. 2.3 shows the behavior of the cross sections in the transitional region between the resonances and the continuous DIS spectrum.

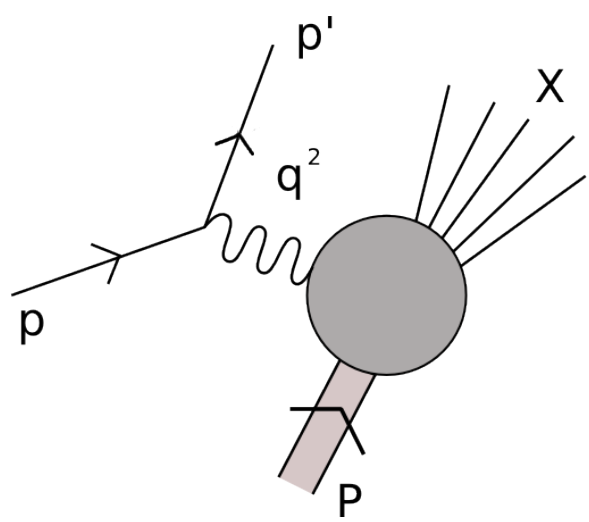

Figure 2.2: Inclusive scattering where the virtual photon interacts with the structure of the proton.

The general form of the cross section for elastic scattering can be obtained from factors in the same manner as in the first part of this chapter. For elastic scattering, it is assumed that the first order electron vertex well describes that part of the interac-

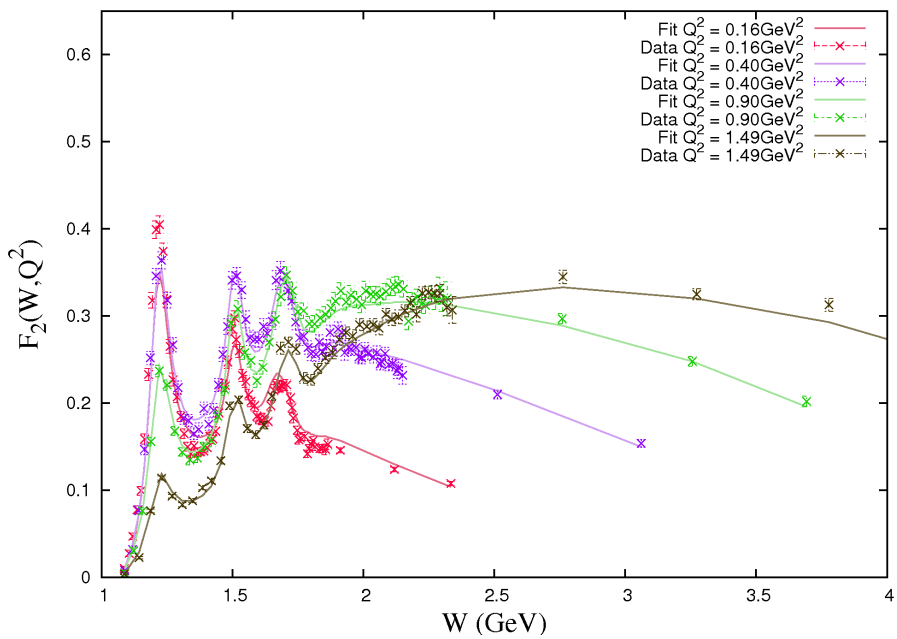

Figure 2.3: Data from SLAC illustrating the transition into deep inelastic scattering. Beyond $W = 2$GeV peaks in the proton structure function $F_2^p \sim \sigma^p$ smooth out into into a continuum. The fits to the data originate from Ref. [3].

tion. The unknown process that needs to be parameterized is the proton interaction vertex represented as a blob in Fig 2.2. Using a similar matrix element as in Eq. 2.2,

$$\mathcal{M} = e^2[\bar{u}(p')\gamma^\mu u(p)]\frac{1}{q^2}[\bar{u}(P')\Gamma_\mu(Q^2)u(P)], \tag{2.5}$$

with the proton vertex

$$\Gamma^\nu = F_1^p(q^2)\gamma^\nu + F_2^p(q^2)i\sigma^{\nu\alpha}\frac{q_\alpha}{2M}. \tag{2.6}$$

The functions $F_1^p(q^2)$ and $F_2^p(q^2)$ are the proton elastic form factors. Superscripts denote that the quantity describes the proton–analogous functions describe the neutron and deuteron. Elastic scattering is commonly expressed in terms of the Sachs form factors:

$$G_E(Q^2) = F_1(Q^2) - \frac{Q^2}{4M^2}F_2(Q^2) \tag{2.7}$$

and

$$G_M(Q^2) = F_1(Q^2) + F_2(Q^2), \tag{2.8}$$

where

$$\tau = \frac{Q^2}{4M^2}. \tag{2.9}$$

The differential electron proton elastic cross section in terms of the Sachs form factor is:

$$\frac{d\sigma}{d\Omega} = \left(\frac{d\sigma}{d\Omega}_{Mott}\right)\left\{\frac{{G_E}^2(Q^2) + \tau {G^2}_M(Q^2)}{1+\tau} + 2\tau {G_M}^2(Q^2)\tan^2\frac{\theta}{2}\right\}, \tag{2.10}$$

which is known as the Rosenbluth formula. The form factors are called the "electric" and "magnetic" form factors respectively, because at $Q^2 = 0$ the equalities $eG_E^{p,n}(0) = q^{p,n}$ and $G_M^{p,n}(0) = \mu^{p,n}$ are obtained. The charge of the proton(neutron) is $q^{p(n)}$, μ is the magnetic moment, and e is the magnitude of the electron charge. The Fourier transforms of these form factors furthermore yield the charge and magnetization density of the nucleons in the non-relativistic regime.

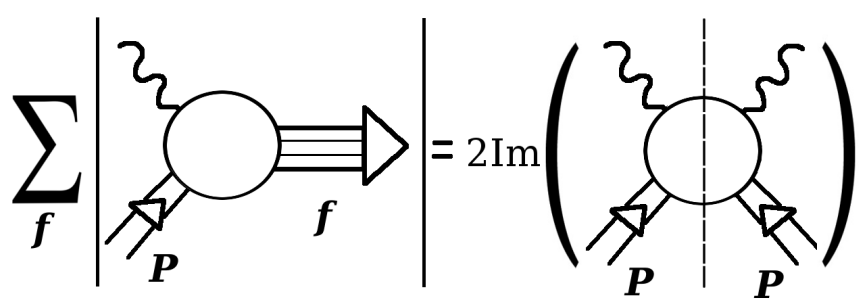

Figure 2.4: Illustration of the optical theorem.

Now, if the form factors $G_{E,M}^{p,n}$ can provide a description of elastic scattering, what

then of inclusive DIS? The difficulty in describing inclusive DIS is that the final state is unknown. Without a known final state, one can't write down a Feynman diagram, and one has no framework to describe one's measurements. In order to calculate the cross section for inclusive DIS, one turns to the optical theorem. The optical theorem relates the matrix element for a process $a \to b$ to the sum over possible final states, f, of the product of matrix elements for $a \to f$ and $b \to f$. Let $a = b = \gamma P$ (forward Compton scattering), and the matrix element for a sum over all final states can be related to the to the matrix elements for Compton scattering. This is illustrated in Fig 2.4. See Greiner [4] or Peskin and Schroeder [5] for a more detailed discussion on the use of the optical theorem. This particular application of the optical theorem gives

$$|\mathcal{M}(ep \to e'X)|^2 = \frac{e^4}{q^4} L_{\mu\nu} W^{\mu\nu}, \tag{2.11}$$

where $L_{\mu\nu} = \bar{u}(k')\gamma_\mu u(k)\bar{u}(k)\gamma_\nu u(k')$ is the leptonic tensor, $W^{\mu\nu}$ is given by the hadronic part of the foward Compton matrix element (right hand side of Fig 2.4), and X indicates the inclusion of all final states. Summing over final and averaging over intitial lepton spin states, one has

$$L_{\mu\nu} = 2[p_\mu p'_\nu + p'_\mu p_\nu - g_{\mu\nu} p \cdot p']. \tag{2.12}$$

The hadronic tensor is, for unpolarized forward Compton scattering, of the form

$$W_{\mu\nu} = \left(-g_{\mu\nu} + \frac{q_\mu q_\nu}{q^2}\right) W_1(Q^2, \nu) + \left(P_\mu - q_\mu \frac{P \cdot q}{q^2}\right)\left(P_\nu - q_\nu \frac{P \cdot q}{q^2}\right) \frac{W_2(Q^2, \nu)}{M^2}, \tag{2.13}$$

where W_1 and W_2 are functions of the Lorentz invariant Q^2 and the energy transfer ν. This is completely general, and all of the unknown interactions are parameterized in $W_{1,2}$, which are known as the structure functions for inclusive unpolarized lepton-

nucleon scattering. The cross section for inclusive scattering can be written explicitly in terms of the structure functions:

$$\frac{d^2\sigma}{dE'd\Omega} = 4E'^2 \frac{\alpha^2}{(Q^2)^2} \left(2\sin^2\left(\frac{\theta}{2}\right) W_1(Q^2,\nu) + \cos^2\left(\frac{\theta}{2}\right) W_2(Q^2,\nu) \right). \tag{2.14}$$

The tensors in equations 2.13 and Eq. 2.12 describing unpolarized scattering include an implicit average over the initial spin state. If one allows for the possibility of a definite initial spin state, the average can be removed, and

$$L_{\mu\nu} = 2[p_\mu p'_\nu + p'_\mu p_\nu - g_{\mu\nu} p \cdot p' + i\epsilon_{\mu\nu\alpha\beta} s^\alpha q^\beta]. \tag{2.15}$$

The first part of Eq. 2.15 is the same as Eq. 2.12 and the imaginary term is anti-symmetric in μ and ν. Since Eq. 2.12 is symmetric in μ and ν one can break up $L_{\mu\nu}$

$$L_{\mu\nu} = L^S_{\mu\nu} + L^A_{\mu\nu}, \tag{2.16}$$

where S and A indicate symmetric and anti-symmetric terms respectively. The hadronic tensor, without the initial spin average, breaks down similarly into

$$W_{\mu\nu} = W^S_{\mu\nu} + W^A_{\mu\nu}, \tag{2.17}$$

with $W^S_{\mu\nu}$ the same as equation 2.13 and the antisymmetric part

$$W^A_{\mu\nu} = i\epsilon_{\mu\nu\alpha\beta} q^\alpha \left[G_1(\nu,Q^2) S^\beta + \frac{G_2(\nu,Q^2)}{M^2} (S^\beta P \cdot q - P^\beta S \cdot q) \right]. \tag{2.18}$$

Then for polarized scattering, the cross section is proportional to $L^A_{\mu\nu} W^A_{\mu\nu} + L^S_{\mu\nu} W^S_{\mu\nu}$. The part symmetric in μ and ν is the same as in Eq. 2.14. The part anti-symmetric in μ and ν is only accessible in polarized scattering, and involves the structure functions G_1 and G_2. Usually when describing polarized DIS, one uses the spin structure

functions g_1 and g_2 defined as

$$g_1(x, Q^2) = M^2 \nu G_1(\nu, Q^2), \text{ and} \tag{2.19}$$

$$g_2(x, Q^2) = M \nu^2 G_2(\nu, Q^2). \tag{2.20}$$

Since the symmetric part of the cross-section is insensitive to the target and lepton spin, in a calculation of the difference in cross sections for a spin flip on the target, the symmetric terms cancel out. By measuring difference in cross sections or asymmetries, it is possible to extract the spin structure functions g_1 and g_2. The cross section difference between reactions that have electron spin $\vec{s}$ and proton spin $\vec{S}$ and reactions that have electron spin $-\vec{s}$ and proton spin $\vec{S}$ is

$$\begin{aligned} \Delta\sigma &= \frac{8m\alpha^2 E'}{q^4 E} \left[(q \cdot S)(q \cdot s) + Q^2 (s \cdot S)\right] M G_1 \\ &+ \frac{8m\alpha^2 {E'}^2}{Q} \left[(s \cdot S)(P \cdot q) - (q \cdot S)(P \cdot s)\right] \frac{G_2}{M}. \end{aligned} \tag{2.21}$$

A cross section difference of this type can be measured by an experiment in which there is a rapid beam helicity flip (as exists at Jefferson Lab). Events can be sorted by the helicity state of the beam, and the two cross sections calculated using the two sets of events then subtracted. However, measuring a cross section difference only gives a linear combination of the structure functions. If one wants to extract them separately, one can take another cross section difference measurement after rotating the target spin 90°. With the relative angle between the target spin and electron spin changed, the factors multiplying the structure functions in 2.21 change. The structure functions can then be calculated via linear combinations of the two cross section difference measurements. A similar method can be used with cross section asymmetry measurements, and is described in detail in section 6.1.

To reiterate: the spin structure functions and the unpolarized structure functions contain all the "interesting physics" of the interaction. The "interesting physics" being the part of the scattering process that is inexpressible in terms of formal Feynman diagrams because the precise structure of the nucleon is unknown. The behavior of the functions gives one a window into the sub-structure of the proton. The interpretation of the structure functions in terms of the constituent quark model will be given in the next chapter.

Chapter 3

Quark Parton Model

Early SLAC measurements of the structure functions led to the postulation that nucleons are composed of partons– point-like particles. Measurements of the dimensionless structure functions

$$F_1(x, Q^2) = MW_1(\nu, Q^2) \tag{3.1}$$

and

$$F_2(x, Q^2) = \nu W_2(\nu, Q^2) \tag{3.2}$$

revealed that, in the limit of $\nu \to \infty$ and $Q^2 \to \infty$ but $x = \text{Const}$, they depended only on x. This limit is known as the Bjorken scaling limit, and in that limit the structure functions have no Q^2 dependence. Fig. (3.1) shows the available data for F_2^p and illustrates the scaling phenomena. Weak Q^2 dependence is indicative of QCD interaction. Recalling that Q^2 provides the scale of the spatial interaction, it was suggested that if DIS scattering is independent of the length scale, then whatever object the virtual photon is probing has no extent and behaves like a free point-like particle. The scaling behavior of the nucleon structure functions was predicted earlier in the late 1960's by Bjorken in Ref. [6]. Scaling and its experimental confirmation provided the impetus to create the parton model. This model suggests that the nucleon is

composed of point-like free particles with momentum parallel to the proton's. These particles are what absorb the virtual photon during scattering. In the scaling limit, we can write the structure functions, $F_1(Q^2, x)$ and $F_2(Q^2, x)$, as their corresponding asymptotic value in this limit, $F_1(x)$ and $F_2(x)$.

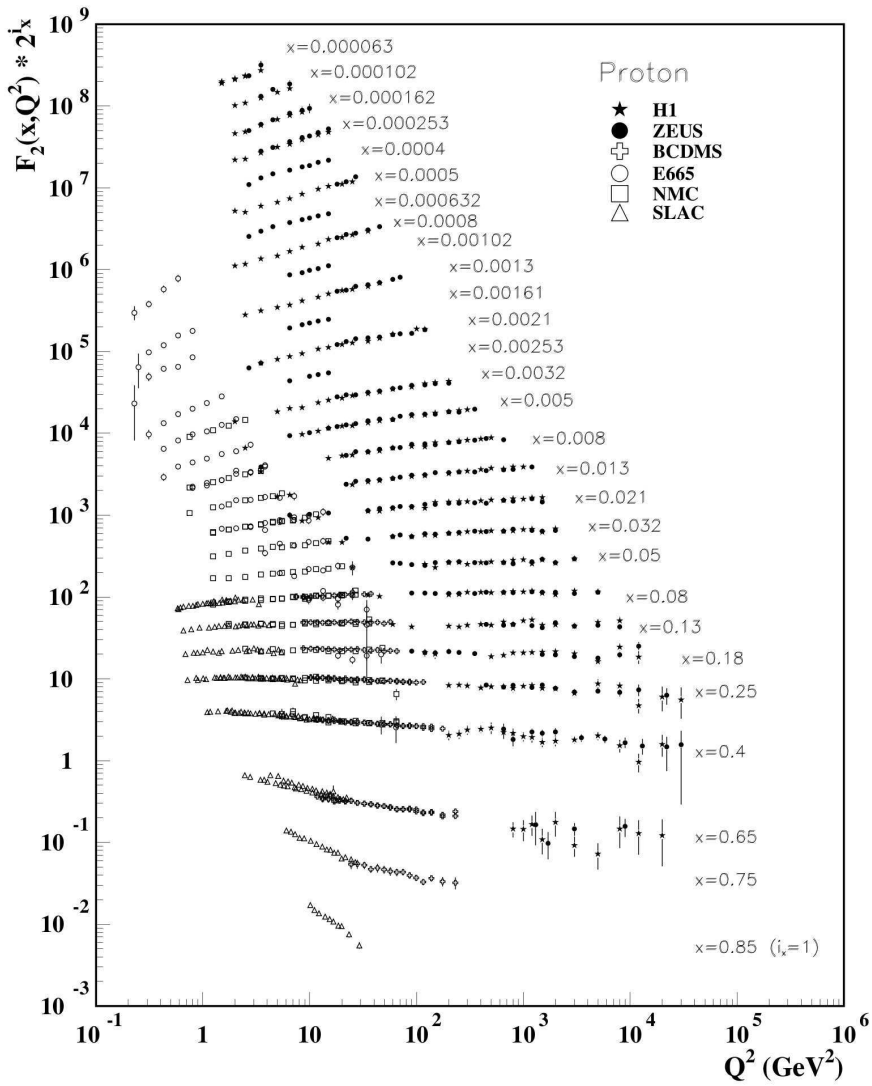

Figure 3.1: $F_2^p(x, Q^2)$, the proton unpolarized structure function. Graphic taken from Ref [2]. See reference for data sources. The data shown is collected into groups with common x_{bj} values, which is indicated by a label next to the group. The structure function F_2 shows only a very weak dependence on Q^2 for each x_{bj} value.

In addition to the discovery of scaling, new baryons and resonances of the nucleon were being found and cataloged at the time. These degrees of freedom of the nucleon

implied by the family of nuclear resonances and the limitations imposed by the Pauli exclusion principle led to the development of the quark model– quarks being a type of parton. The resonances and particles produced from scattering experiments (eN, π^+N, etc.) in the resonance region can be explained by assuming that the observed baryons are composed of 3 particles (now called quarks) each with spin 1/2 and fractional charge. Each baryon is a different 3 particle combination of three quark types– u(up), d(down), or s (strange). Tables of the known baryons and the quarks are shown below in Figs. 3.2, 3.3, and 3.4.

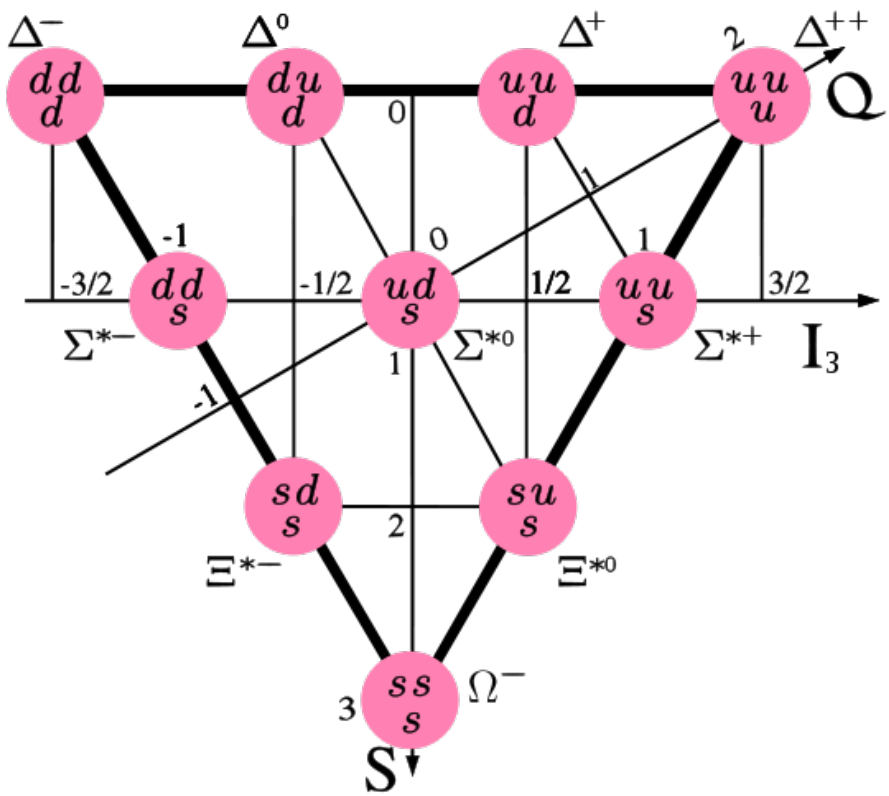

Figure 3.2: Baryon decuplet (angular momentum 3/2): Arrows indicate directions of increasing strangeness (S), isospin (I_3), and charge (Q).

The existence of certain baryons, if the quark model is correct, necessitates a new property to be assigned to quarks. For example, the Δ^- of charge $-e$ and spin 3/2 is composed of three down quarks. The only quantum number that the quarks have to distinguish themselves is spin, and the total spin of the system (3/2) requires that

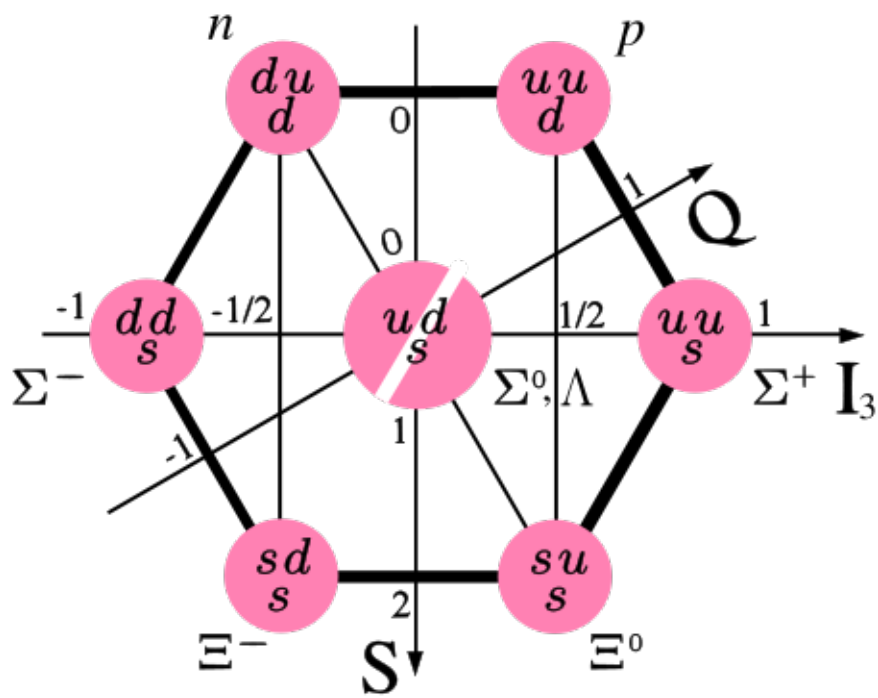

Figure 3.3: Baryon octet (angular momentum 1/2): Arrows indicate directions of increasing strangeness (S), isospin (I_3), and charge (Q).

the quarks it is made up of have aligned spins. Since the quarks are fermions, this violates the exclusion principle, as each fermion is in an identical quantum state. In order to allow this state to exist, it was postulated by Gell-Mann that quarks have the property of *color*. Each quark has a color assignment of $R, \bar{R}, G, \bar{G}, B$, or $\bar{B}$, with the bar indicating the corresponding anti-color state. (RGB stands for red, green, and blue respectively)

The quarks interact via the weak and electromagnetic force. However, a model of the proton requires some other mechanism for explaining the interaction that forms nucleonic bound states. A theory of a force that interacts through color charge was developed in order to explain quark-quark interactions: quantum chromodynamics (QCD). QCD is a field theory based on SU(3) color symmetry. While important to quark interactions, the strong nuclear force (the name given to the force described by QCD and which mediates interaction between color charged particles) becomes

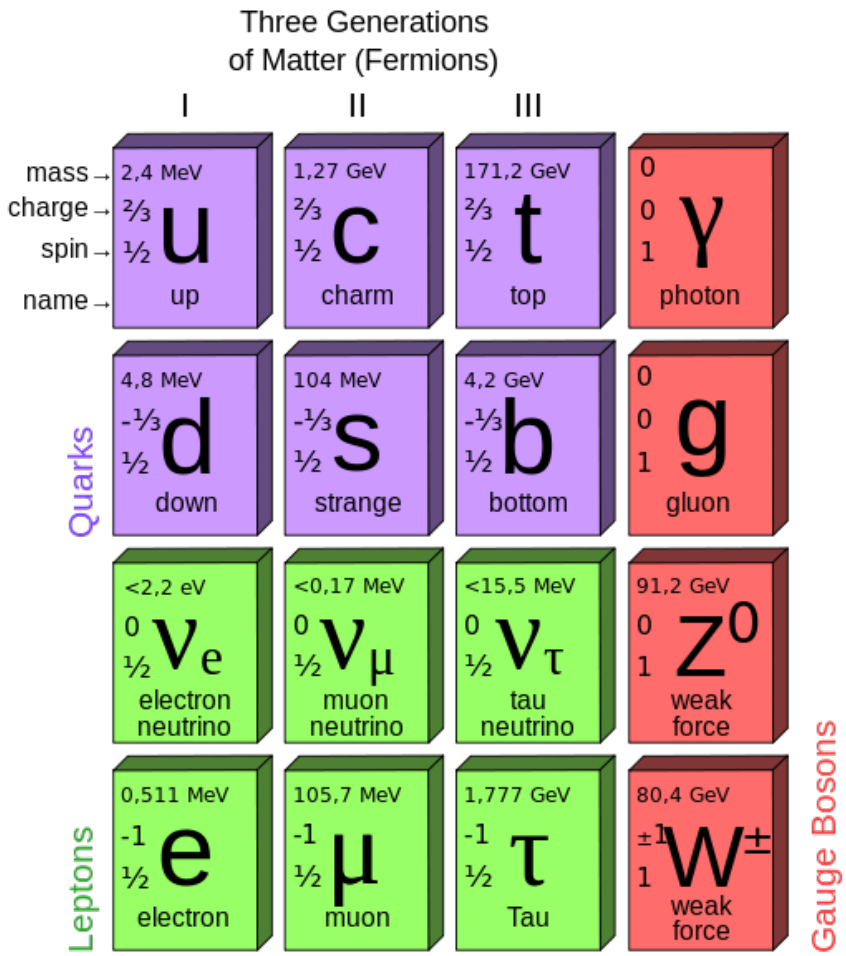

Figure 3.4: Elementary particles, consisting of leptons, quarks, and gauge bosons. Masses, charges, and spins are given. Anti-particles exist for each of the fermions. (attribution of graphic unknown)

weaker the closer particles are to one another; so at some small length scales, the strong force is negligible. This phenomenon is call *asymptotic freedom*. Because of the inverse relationship between the strength of quark color interation and length, there are some regimes in which QCD plays very little role in scattering. These QCD interactions show up only as a small Q^2 dependent correction. Much success has been had in explaining the nucleon using a constituent quark model (CQM) with free quarks in the so called impulse-approximation, which ignores the strong interaction altogether.

The picture painted by the CQM is that the nucleon is made up of three constituent quarks (uud for proton and udd for neutron), and a sea of quark anti-quark pairs ($u\bar{u}$, $d\bar{d}$, and $s\bar{s}$). The scaling property of the structure functions implies that the scattering process involves only a parton and the incident virtual photon. One wonders why this is a justifiable picture, considering *something* must be holding the partons together. It turns out that DIS occurs in a regime in which interactions take place "on the light cone." The participants in the process are separated by a light-like interval, and are thus isolated from one another. This means that the DIS scattering effectively takes a snapshot of the proton fast enough that the quark-quark interactions are negligible. An exposition of this idea follows:

The definition of the hadronic tensor can be written down as

$$W^{\mu\nu} = \frac{1}{4M} \sum_{\sigma} \int \frac{d^4\xi}{2\pi} e^{iq\cdot\xi} \langle p, \sigma \mid \left[J^{em}_{\mu}(\xi), J^{em}_{\nu}(0) \right] \mid p, \sigma \rangle, \tag{3.3}$$

where $[J^{em}(\xi), J^{em}_{\nu}(0)]$ is the commutator of the electromagnetic current between the two space time points ξ and 0. Eq. 3.3 can be expressed in terms of *light-cone variables*. Let a set of light cone variables a^+ and a^- be constructed from a variable a by $a^{\pm} = (a^0 \pm a^3)/\sqrt{2}$. The 4 momentum light-cone variables are then re-written

$$q^+ = -\frac{Mx}{\sqrt{2}} \tag{3.4}$$

$$q^- = \frac{(2\nu + Mx)}{\sqrt{2}}. \tag{3.5}$$

In the Bjorken limit, q^+ remains the same, but $q^- \to \sqrt{2}\nu$, since the energy transfer grows while $x = Q^2/2M\nu$, remains constant. So in the Bjorken limit, $q^- \to \infty$. This implies that

$$\xi^+ \to 0 \tag{3.6}$$

$$|\xi^-| < \frac{\sqrt{2}}{Mx}. \tag{3.7}$$

Writing Eq. (3.3) in terms of the light cone variables,

$$W_{\mu\nu} = \int d\xi^- e^{iq^+\xi^-} \int d\xi^+ d^2\xi_T e^{iq^-\xi^+} \langle p,\sigma \mid \left[J^{em}_\mu(\xi), J^{em}_\nu(0)\right] \mid p,\sigma\rangle. \tag{3.8}$$

The above integral vanishes except for contributions due to singularities of the integrand. The integrand is singular at $\xi^+ = 0$, and therefore DIS is dominated by $\xi^+ \simeq 0$. See Ref. [7] for a detailed argument; the length scale which DIS is probing in the Bjorken limit is not that of physics of small length scales but rather physics at $\xi^2 = 0$ space time intervals. That is, physics on the light cone. Events lying on a light cone can obviously not affect one another without violating causality, and so in the impulse approximation, we assume that the virtual photon is sampling a collection of free non-interacting partons.

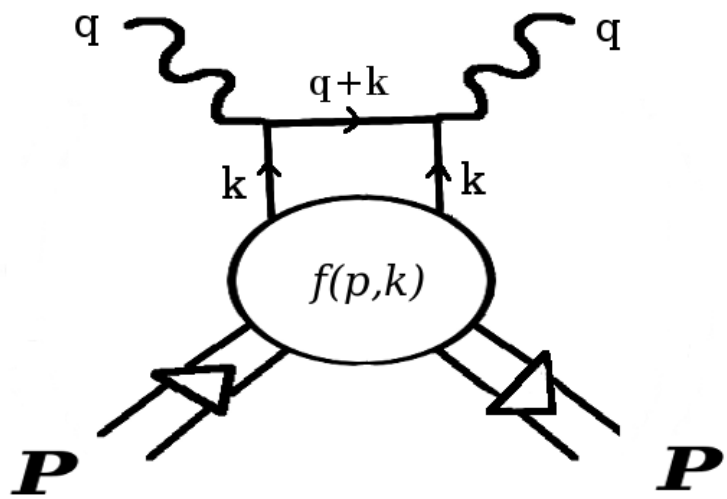

Figure 3.5: Graph for the interaction of a photon (momentum q) with a parton carrying momentum k inside a nucleus with momentum p.

The tensor for the interaction of a photon with a free parton is easy to write down. From Fig 3.5 it is

$$W_{\nu\mu}(q,p) = \sum_i \sum_s \int d^4k f^i_s(p,k) w^i_{\mu\nu}(q,k) \delta[(k+q)^2] \tag{3.9}$$

The sum is over quark flavors, i, and helicties, s, and where f is the corresponding quark momentum distribution. Using the substitution $x_i = k^+/p^+$, so that x_i is the fraction of proton light cone momentum carried by the struck quark, and expanding the photon-quark electromagnetic vertices, $w^i_{\mu\nu}$, one has

$$\begin{aligned} W_{\mu\nu}(q,p) &= \textstyle\sum_i e_i^2 \int \frac{d^4k}{2M\nu}[f^i_+(p\cdot k) + f^i_-(p\cdot k)]\delta(x_i - x) \\ &\quad \times[2k_\mu k_\nu + k_\mu q_\nu + q_\mu k_\nu - g_{\mu\nu} k\cdot q]. \end{aligned} \tag{3.10}$$

Going to the proton rest frame and setting $\nu = \mu = 2$, one gets from eq. (2.13) $W_{22} = W_1$. Using the differential $d^4k = \frac{\pi}{2}\frac{dx}{x}dk^2 dk_T^2$ the structure function $F_1(x)$ can be calculated in terms of the quark momentum distributions functions:

$$\begin{aligned} F_1(x) &= \tfrac{1}{2}\textstyle\sum_i e_i^2 q_i(x) \\ &= \tfrac{1}{2}[\tfrac{4}{9}(u(x) + \bar{u}(x)) + \tfrac{1}{9}(d(x) + \bar{d}(x)) + \tfrac{1}{9}(s(x) + \bar{s}(x))] \end{aligned} \tag{3.11}$$

where

$$q_i(x) = \frac{\pi}{4}\int dk_T^2[f^i_+(p\cdot k) + f^i_-(p\cdot k)]. \tag{3.12}$$

The distribution function $q_i(x)$ is the probability of finding a quark of flavor i with momentum fraction x (the quark has 3-momentum $|\vec{k}| = x|\vec{p}|$).

Most measurements cannot accesses particular quark distribution functions. Since the quarks are inextricable from one another, measurements sample quantities that are sums of the distribution functions, like F_1. The integral over these quantities can be predicted based on known or presumed facts about nucleon structure, and the integrals can be calculated from data, given a measurement over a wide enough kinematic range. For example, since the proton(neutron) has 2(1) up quarks and 1(2) down quark, an integral over F_1 should give the following:

$$2\int_0^1 dx F_1^{\mathrm{p}}(x) = 2\frac{4}{9} + 1\frac{1}{9} + 0\frac{1}{9} = 1, \text{ and} \tag{3.13}$$

$$2\int_0^1 dx F_1^{\mathrm{n}}(x) = 2\frac{1}{9} + 1\frac{4}{9} + 0\frac{1}{9} = \frac{2}{3}. \tag{3.14}$$

The spin structure functions also have interpretations in the quark model. The first SSF is the sum over the helicity differences of each quark flavor:

$$g_1(x) = \sum_i e_i^2 (q_i^+(x) - q_i^-(x)). \tag{3.15}$$

At momentum fraction x, $g_1(x)$ is the probability of finding a positive helicity quark minus the probability of finding a negative helicity quark weighted by the quark charge. So if at high x in the proton the quark distribution functions are dominated by completely polarized up quarks (which experiments suggests [8]), then the polarized structure function would approach $e_u(1-0) = 2/3e$ as $x \to 1$. The second unpolarized structure function can be obtained using the Callan-Gross relationship:

$$F_2(x) = \sum_i e_i^2 x q_i(x). \tag{3.16}$$

This is all assuming that one can model the nucleon as bunch of co-linear free partons. Notice that QCD principles were not invoked during the above discussion. Measuring the structure functions and their moments and seeing where the predictions of the CQM break down sheds light on the regimes in which QCD plays a part in the structure of the proton. This is usually seen as additional Q^2 dependence that violates scaling. That the free quark model works even a little is dependent on the phenomena of aymptotic freedom. That is that the strong force becomes weaker on short length scales, and negligible at small enough length scales. The second polarized structure function g_2 does not have an interpretation in the CQM. Indeed, the data from g_2, unlike the data for the unpolarized structure function, on which flavor decomposition has been performed [9] [10], the quark distribution functions cannot be explained outside the framework of the strong interaction. Additionally there has been much

work in trying to explain these structure functions with what is called the *operator product expansion* (OPE : see most texts on QFT for treatment [5], [8], or [11]) as well as perturbative quantum chromodynamics (pQCD) [12] [13] [14].

The data from SANE is used herein to extract the asymmetry $A_1^p(x)$, discussed in more detail in the next chapter. The shape of the asymmetry is connected to the shape of the quark distribution functions. Much work has been done to extract the individual flavor distribution functions [9] [10], but $A_1^p(x)$ can provide information on the quark behavior without resorting to the model dependent extractions. Consequently, $A_1^p(x)$ and in particular its limit as $x \to 1$ can be used as a test of the CQM and the current understanding of the composition of the proton.

Chapter 4

Spin Asymmetry A_1^p

4.1 Definition

Consider a polarized electron scattering from a polarized proton. Form the asymmetry between opposite spin orientations for the proton:

$$A = \frac{\frac{d^2\sigma^{\Uparrow\uparrow}}{d\Omega dE'} - \frac{d^2\sigma^{\Downarrow\uparrow}}{d\Omega dE'}}{\frac{d^2\sigma^{\Uparrow\uparrow}}{d\Omega dE'} + \frac{d^2\sigma^{\Downarrow\uparrow}}{d\Omega dE'}}. \tag{4.1}$$

The $\Uparrow$ indicates positive orientation of the nucleon along a chosen spin axis, and $\Downarrow$ indicates a negative orientation. The denominator is simply twice the unpolarized cross section. The numerator depends on the scattering behavior for the different relative spin orientations. The analysis section shows how one can use the measured asymmetries A_{80° and $A_{\nparallel}$ ($\nparallel$ is being used to denote anti-parallel or 180°) to obtain the virtual photon asymmetries A_1^p and A_2^p.

The asymmetries A_1^p and A_2^p are analogous to the cross section asymmetry in Eq. 4.1, and are formed by using the different angular momentum states in virtual Compton scattering instead of electron angular momentum states. Break the Feynman diagrams from inclusive electron scattering into two separate processes: 1. An

electron emits a virtual photon with 4-momentum q^μ, 2. the nucleon absorbs a virtual photon. Thinking of the scattering process in that way, one can factor the cross section into two terms: the cross section is the product of the probability that an electron emits a virtual photon with kinematics described by ν and Q^2, and the probability that a nucleon will absorb a photon in that kinematic range. The measured quantities describing those processes are the virtual photon flux, $\Gamma(\nu, Q^2)$, and the absorption cross section for a virtual photon, $\sigma(\gamma)$, respectively.

The virtual flux and photon absorption cross section depend on the polarization state of the virtual photon. Massless particles are allowed to have angular momentum number values of $m = 1, -1$, that is spin only aligned or anti-aligned with their momentum. These states represent transverse polarization states for photons. In the case of a virtual photon, its invariant mass need not be zero, which means longitudinal $m = 0$ states are also allowed. The inclusive cross section can be decomposed into

$$\frac{d\sigma}{d\Omega dE'} = \Gamma_T \sigma_T(\gamma) + \Gamma_L \sigma_L(\gamma), \tag{4.2}$$

where L and T indicate the longitudinal or transverse photon polarization state respectively. The ratio of transverse to longitudinal photon flux is given by the kinematics of the electron, $\Gamma_L = \epsilon \Gamma_T$ with

$$\epsilon = \frac{1}{1 + 2(1 + \frac{\nu^2}{Q^2}) \tan^2 \frac{\theta}{2}}. \tag{4.3}$$

Looking at only the virtual photon and its interaction with the target, A_1 can be defined as the asymmetry between the photo absorption cross section for scattering with transverse photons that are either aligned or anti aligned with the target spin.

$$A_1^p(\gamma) = \frac{\sigma_T^{1/2} - \sigma_T^{3/2}}{\sigma_T^{1/2} + \sigma_T^{3/2}}. \tag{4.4}$$

An asymmetry can similarly be formed using the interference term between the T and L states:

$$A_2^p(\gamma) = \frac{\sigma_{TL}}{\sigma_T}. \tag{4.5}$$

The subscripts on σ indicate that the photon angular momentum is oriented along its direction of motion (T), or perpendicular to the direction of motion (L). The target nucleon polarization is measured along the same axis as the photon momentum, and the superscripts indicate the total angular momentum of the system. Unlike the electron cross section asymmetry given in Eq. 4.1, the expression for A_1^p makes its dependence on the angular momentum of the final state manifest. If the final state is a quark or proton, angular momentum conservation requires that $\sigma_T^{3/2} = 0$, which means $A_1 = 1$. If the final state is a Δ, since the Δ has spin 3/2, both $\sigma_T^{3/2}$ and $\sigma_T^{1/2}$ are non-zero. The relative probability between producing a Δ with $|S = 3/2, S_z = 3/2 >$ from a $|s_1 = 1/2, s_{1z} = 1/2, s_2 = 1, s_2z = 1 >$ state and producing a Δ with $|S = 3/2, S_z = 1/2 >$ from a $|s_1 = 1/2, s_{1z} = 1/2, s_2 = 1, s_2z = -1 >$ state is 1/3. So given $\sigma_T^{1/2} = \frac{1}{3}\sigma_T^{3/2}$, we have $A_1^p = -1/2$ for that particular reaction. This example shows that the asymmetry is related to the spin interaction between the target and the probe. However, A_1^p is not defined for a particular process; it is an inclusive absorption cross section asymmetry and kinematic dependent. The actual calculation and prediction of $A_1^p(x, Q^2)$ is not so simple.

4.2 Measurements and Models

The spin asymmetry A_1(from here out, A_1 and all other asymmetries and structure functions will be assumed to refer to the asymmetry associated with the proton unless otherwise stated) can be extracted from electron asymmetry measurements as long as the photon flux can be calculated in the kinematic region of interest.

The asymmetry in the absorption cross section for the different helicities arises

from the spin dependent interactions of the photons with the structure of the proton. The structure functions that describe the spin dependent behavior of proton scattering are the spin structure functions first appearing in Eq. 2.18. The virtual photon asymmetry is, in terms of the SSFs,

$$A_1 = \frac{g_1}{F_1} - \frac{Q^2 g_2}{\nu^2 F_1}. \tag{4.6}$$

As mentioned in chapter 2, the structure functions can be accessed via measurements of cross section asymmetries at target polarizations ninety degrees apart– say $A_\parallel$ (with target spin aligned with the beam helicity) and $A_\perp$. Data that gives one the structure functions can be used to calculate a linear combination of the two, and the exact expression of A_1 in terms of the measured asymmetries $A_\parallel$ and $A_\perp$ can be found in section 6.1.2.

Performing a measurement with a target polarization perpendicular to the beam helicity is technically challenging, and for many experiments, [15], [16], [17], and [18], A_1 has been approximated using the relationship

$$A_1 \approx \frac{g_1}{F_1} \approx D A_\parallel, \tag{4.7}$$

where D is a known quantity depending on kinematic variables (see section 6.1). This approximation is good as long as the perpendicular asymmetry is small in that region. The existing measurements of $A_\perp$ indicate that this is the case, and its contribution is further suppressed by a small kinematic factor (see section 6.1). Experimental measurements of g_2 and $A_\perp$ [19], [20], [21], [22] suggest that this approximation is reasonable.

Only three previous experiments have collected data that allow for the direct determination of A_1 using $A_\perp$ [23] [22] [24]. The data from SANE includes perpendicular and parallel asymmetries; a direct calculation of A_1 will be shown later. Such

a calculation of A_1 and a measurement of the contribution of $A_\perp$ is necessary as most models and interpretations of A_1 assume that equation 4.7 is a good approximation. If Eq. 4.7 holds, A_1 can be written as a ratio of the sums of polarized and unpolarized quark distribution functions. If in some region of x the contribution of $A_\perp$ becomes large, most models of $A_1(x)$ will break down.

The existing world data for A_1 provides fairly good coverage of the Bjorken x region up to 0.5. The asymmetry being Q^2 independent is also very well supported by these data. It has been suggested that there is a weak $1/ln(Q^2)$ dependence, but a review on the subject of polarized DIS [11] argues that the data are inconclusive at present. A collection of world data is shown in figure 4.1. Marked on the plot is the $A_1 = 5/9$ line, which is predicted by the naive CQM. If A_1 is approximately g_1/F_1, then we can write A_1 in the CQM model as

$$A_1 = \frac{\frac{4}{9}\Delta u + \frac{1}{9}\Delta d}{\frac{4}{9}u + \frac{1}{9}d} \tag{4.8}$$

by using Eq. 3.15 and Eq. 3.11. Consider the anti-symmetrized wave function of a nucleon composed of 3 spin half particles–two with identical flavor, and one gets $\Delta u = 4/3$ and $\Delta d = -1/3$. Counting two up quarks and one down quark gives

$$A_1^{\mathrm{CQM}} = \frac{5}{9}. \tag{4.9}$$

The CQM does not predict the x- dependence of A_1, but as we move toward higher x, the effects of sea quarks become less pronounced. The valence quarks become the most prominent contributors to the quark distributions functions. Based on the CQM, A_1 might eventually flatten out and approach 5/9. The current high x data set does not appear to be approaching this limit.

Perturbative QCD calculations predict a limiting value of 1 for A_1 as $x \to 1$ [12] [13] [14]. There has also been work done in trying to explain the behavior of A_1 and

the quark distribution functions $u(x)$, $d(x)$, etc. in terms of a more complex quark model that takes into account relativistic effects and interactions like quark hyperfine splitting. One prediction for A_1 by N. Isgur [25] is shown in Fig 4.1 as a band, the width of which represents the variation available in the model due to the adjustment of tuning parameters.

The limit $A_1(x \to 1) = 1$, which is by now assumed by most in the field, has been a guideline used by many theories attempting to model nucleon structure. However, that limit has not been *confirmed* by experiment. SANE's data pushes well past the $x = 0.5$ mark with much higher statistics than any of the previous experiments with model independent extractions.

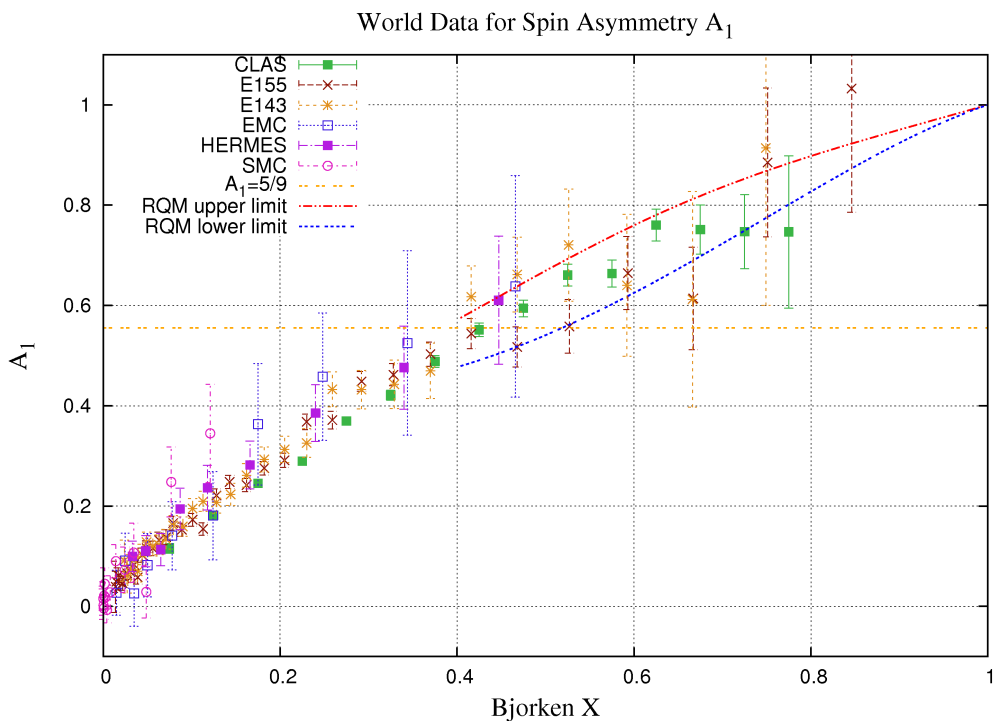

Figure 4.1: World data for A_1, CQM prediction of 5/9, and the RCQM bounds from Ref. [25]. Data from SMC: [20] [26] EMC: [15] [27] HERMES: [16] CLAS: [17] [28] E155: [24] E143: [19] [22].

Flavor decompositions have been performed on data including deuteron and proton targets by taking advantage of isospin symmetry. These decompositions allow for the calculation and modeling of the individual quark distribution functions or combi-

nations of the functions. The ratio of the neutron and proton unpolarized structure function $F_2(x)$ in the quark model is

$$\frac{F_2^n}{F_2^p} = \frac{1 + 4d^p(x)/u^p(x)}{4 + d^p(x)/u^p(x)}. \tag{4.10}$$

Data for this ratio is plotted in Fig. 4.2 from Ref. [29] and [30]. The ratio approaches the limit of 1/4 as $x \to 1$, which is indicative of a negligible down quark contribution to the composition of the proton. If $A_1(x)$ approaches 1 at high x, then the scattering process is dominated by high momentum up quarks with angular momentum aligned with that of the proton.

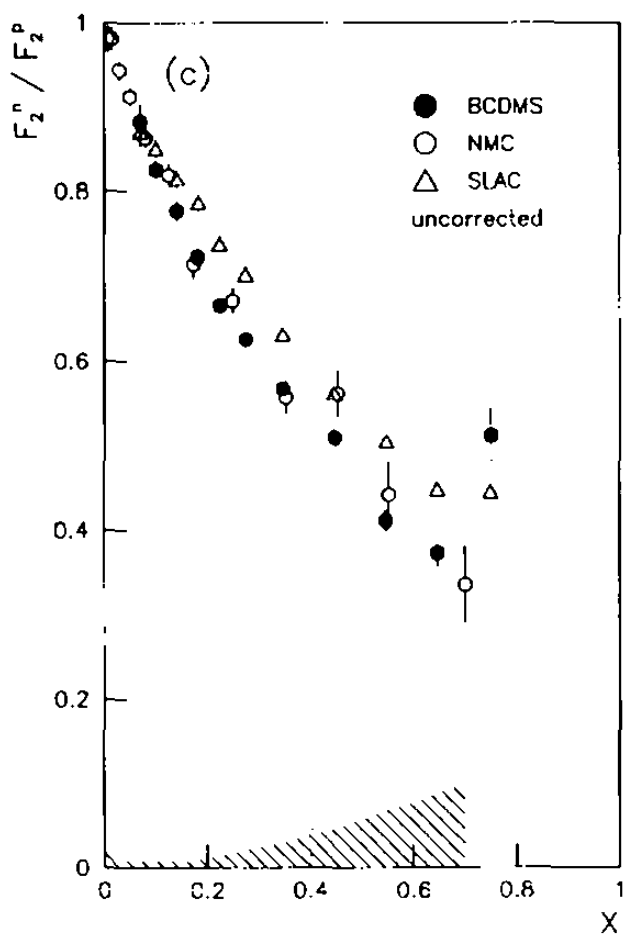

Figure 4.2: Data from the the BCDMS collaboration, SLAC, and the NMC collaboration. Plot from BCDMS paper [29]. Newer data at Ref. [31].

Chapter 5

Experimental Methods

5.1 Overview

SANE was an inclusive measurement of electron scattering off of a polarized ammonia target. The quantity being measured is the asymmetry between beam helicities at two different target orientations. The calculation of A_1 requires asymmetry (Eq. 4.1) data for parallel and near perpendicular target polarization. The most basic needs for performing such a measurement are a polarized target that can change orientation, a polarized beam, and a detection apparatus. The SANE experiment was performed at Thomas Jefferson National Laboratory (JLab) in Hall C of the Continous Electron Beam Accelerator Facility(CEBAF). The facility provides a polarized electron beam. The University of Virginia furnished a polarized solid ammonia target that was oriented such that the target protons were polarized anti-parallel to the beam direction and at 80° with respect to the beam direction. (The geometry of the coils prevented the target field from being rotated to exactly 90°, as the coils would block the acceptance of the detectors)

A new detector package was constructed for this experiment. The new device is called BETA, Big Electron Telescope Array. BETA is a large acceptance multi-

detector apparatus for electron detection. The standard Hall C magnetic spectrometer was also used for parasitic data collection and for measurements necessary for dilution factor calculation and calibration of BETA. The measurement was broken into four configurations–different combinations of beam energy and target polarization (see section 6.2.1).

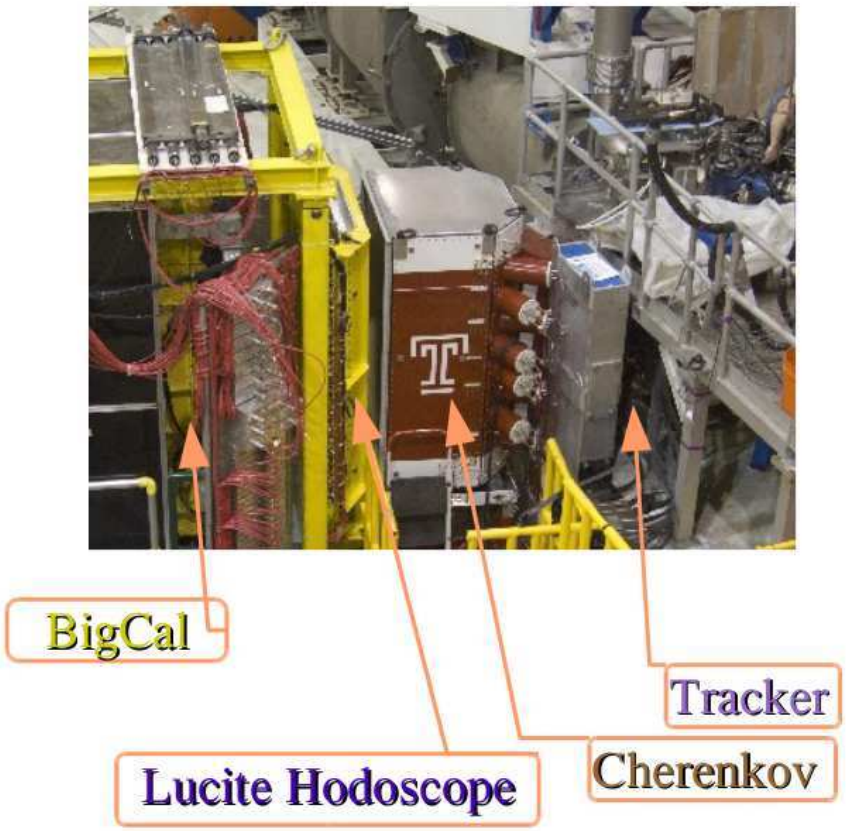

Figure 5.1: Picture of BETA from the side. In this picture, the beam dump is to the left.

The apparatus is described in order from the target out: BETA is composed of a plastic scintillator hodoscope(Norfolk State U.), a nitrogen gas Cerenkov detector (Temple U.), a lucite hodoscope (NC A&T Stat U.), and a large lead glass calorimeter (GEP III collab.). The calorimeter is divided into roughly 4 cm $\times$ 4 cm glass blocks, each with a photomultiplier tube to detect the light from electromagnetic showers. This apparatus is sufficient for establishing the angle and energy of a scattered par-

ticle. The hodoscope and tracker provide additional position information for more precise tracking. The Cerenkov detector provides particle identification. Use of the Cerenkov detector as one half of the data acquisition (DAQ) trigger ensures that BETA is only collecting data from electrons (or positrons) scattered from the target. The detector was positioned such that the central scattering angle is at 40°, and its coverage extends from about 30° to 50° in the horizontal plane at beam height. These systems will be described in more detail along with the target and beamline in this chapter.

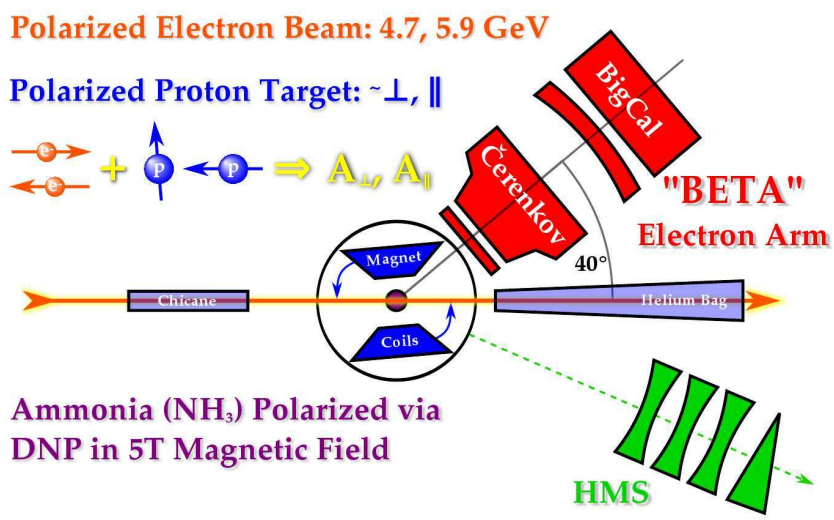

Figure 5.2: Graphical overhead view of the experiment. The beam line is depicted coming from the left, passing through the target, and then through the helium bag. BETA is shown in red and positioned at a scattering angle of 40°. The Hall C spectrometer was positioned at various angles on the opposite side of the beam. The electrons are polarized aligned or anti-aligned with the electron momentum. The magnet coils, which determine the target proton polarization, can be rotated so that their axis is parallel or near perpendicular(shown here) to the beamline (80°). (Image used with permission from [32])

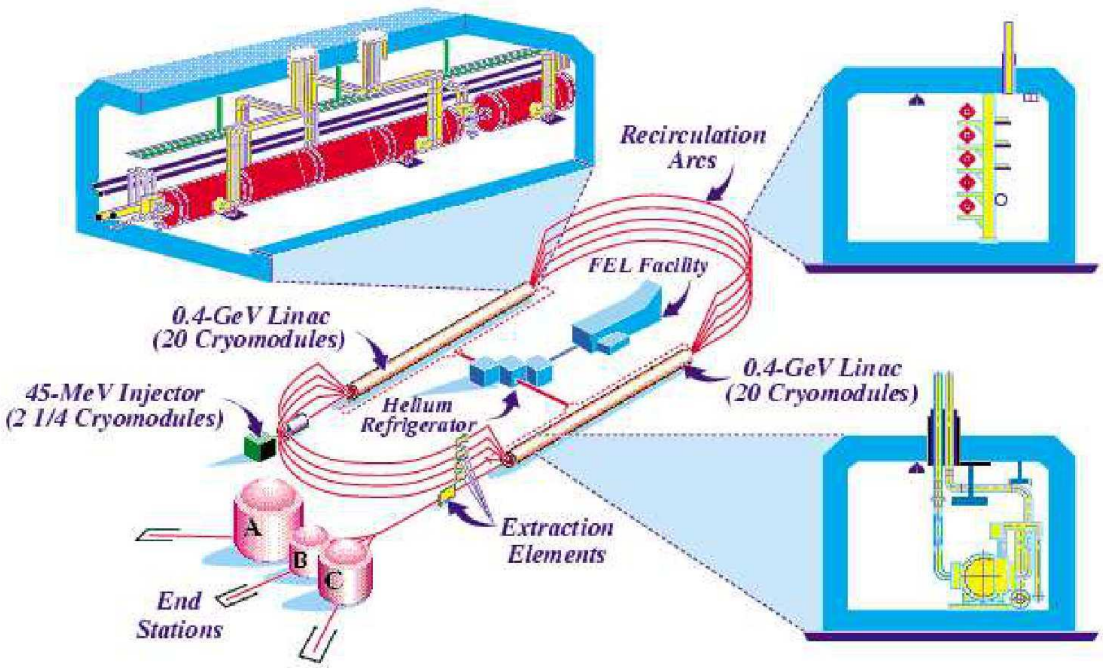

Figure 5.3: Jefferson Lab accelerator and experimental halls.

5.2 TJNAF

The Thomas Jefferson National Accelerator Facility (TJNAF) is home to a high intensity electron accelerator, CEBAF: continuous electron beam accelerator facility. It is capable of providing a continuous beam of polarized electrons to three separate experimental halls. The accelerator is designed with a footprint similar to that of a racetrack, with acceleration taking place along the straightaways. The electrons are re-circulated and accelerated again with each pass through the beam line. Jefferson lab can supply different currents to each hall, and different but correlated energy to each hall.

The polarized electrons are produced and provided with their initial acceleration and polarization direclty at the injector. Infrared light excites electrons from a photocathode, which are then accelerated in a DC field, focused, and pre-accelerated in rf cavities on their way to the main linacs. Once in the main accelerator track,

the electrons are accelerated through a series of rf cavities along the linear stretch of the Jlab accelerator complex. After the initial trip through the linac, the electrons are separated vertically by energy, and magnetically guided through the turns in the accelerator, after which they are sent through the second linac. The electrons are circulated through the accelerator up to five times. Each circulation gains an electron up to 1.2 GeV. Once accelerated to their final energy, they are separated magnetically from the main beam and routed to an experimental hall.

5.2.1 Injector

The polarized electron source is a DC photogun with a mechanically strained gallium arsenide photocathode. In a DC photogun style electron source, a laser pulse excites electrons from a metal or semi-conductor via the photoelectric effect. The photocathode from which the electrons are excited sits at a large constant negative electric potential. The electrons, once free of the photocathode, accelerate away from the photocathode and thereafter can be prepared for injection into the accelerator. Because the photocathode is at a very high potential, positively charged particles or ions will accelerate back towards the photocathode. Ionization can occur when the laser light or electrons come into contact with air molecules or the material components of the injector. The ensuing impingement of the ions on the photocathode can significantly reduce the life of the photocathode, and it is therefore necessary to operate the photogun in a hard vacuum.

The excitation of electrons from the gallium arsenide wafer occur when electrons are excited out of the valence band of the material and up into the conduction band by photons from a laser beam. In gallium arsenide, the energy level of the conduction band actually sits above the energy of an electron in the vacuum, and so conduction band electrons escape from the material and accelerate away from the photocathode.

The transition being excited is that from the conduction band's P state into the

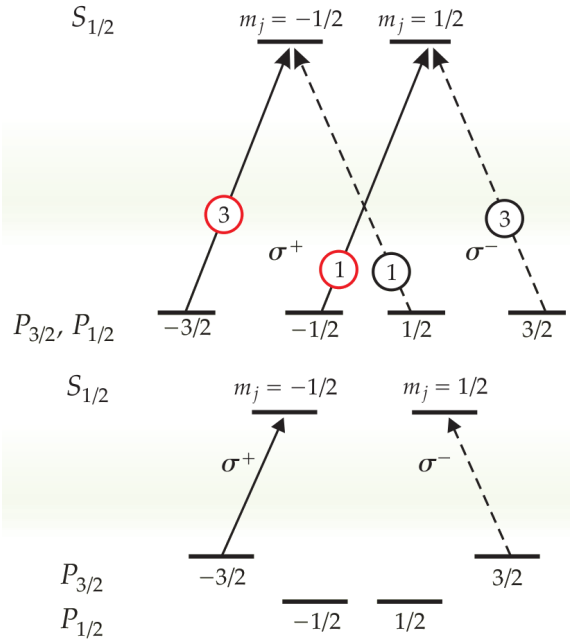

Figure 5.4: Top: electron energy levels in GaAs. Solid lines indicate transitions due to positive helicity photons, and dashed lines mark transitions inducable by negative helicity photons. The numbers in circles indicate the relative probability of a transition. Bottom: electron levels in a strained GaAs wafer. Here the mechanical straining of the substrate lifts the degeneracy in the P states. Image from reference [33].

valence band S state. The $P_{3/2}$ and $P_{1/2}$ states are degenerate, and when the gallium arsenide is illuminated with polarized light of the appropriate helicity, the electrons from the $P_{3/2}(m = -3/2)$ state are excited to the $S_{1/2}(m = -1/2)$ state and the $P_{1/2}(m = -1/2)$ state to the $S_{1/2}(m = 1/2)$ state. The coupling of the angular momentum of the states makes the $P_{3/2}(m = -3/2)$ to $S_{1/2}(m = -1/2)$ transition three times more likely. The coupling of angular momentum states leads to an ejected electron polarization of no more than 50%. By eliminating the degeneracy between the $P_{3/2}$ and the $P_{1/2}$ states, one can preferentially excite the $P_{3/2}$ transitions, populating only the $S_{1/2}(m = -1/2)$ state (or $m = -1/2$, depending on the light helicity).

Mechanically straining a gallium arsenide lattice lifts the degeneracy of these states, and JLab achieves close to 90% polarization at the injector site by using circularly polarized light from fiber lasers with a wavelength of 780 nm incident on a

strained gallium arsenide wafer.

Three separate diode laser systems are used simultaneously for electron production. The diode laser oscillators are rf gain-switched to produce an optical pulse train. The pulses from the three lasers are out of phase by 120° and have a frequency of 499 MHz. The result is a train of electron bunches accelerating away from the cathode at a frequency of 1497 Mhz, which is the operational frequency of the accelerator. Every third electron bunch is produced by the same laser and sent to the same hall at the end of the accelerator. In this manner the polarization and current delivered to a particular hall can be adjusted by changing the polarization and intensity of a single laser. The relationship between the intensity of light and the number of electrons ejected at the photocathode is given by the quantum efficiency (QE):

$$I = \frac{\gamma}{124} P \cdot QE. \tag{5.1}$$

The current in mA of the ejected electrons, I, is dependent on the wavelength, γ, in nanometers; the power, P, in Watts; and the quantum efficiency, QE. The quantum efficiency degrades over time and varies with the incident wavelength.

The helicity of the beam is flipped pseudo-randomly using a Pockels cell that changes the helicity of the incident laser light at a rate of 30 Hz. A halfwave plate can be inserted to induce an overall helicity swap. The pseudo-random helicity ordering and the halfwave plate are used as controls to check for systematic effects in experiments like SANE that require polarized electrons.

5.2.2 Accelerator

The linear accelerator portion of the JLab electron beam line is composed of a series of superconducting radio frequency resonator cavities. The cavities are designed to oscillate at a frequency of 1497 MHz. The electrons to be accelerated enter the cavities

in bunches at this frequency, and the phase of the field oscillation is fixed such that the electric field in the cavity peaks for maximum acceleration when an electron bunch is present in the cavity. The cavities are part of a larger accelerator component called a "cryomodule". Each cryomodule is composed of 8 cavities that together provide about 30 MeV of energy to the electrons. Each cryomodule is connected to a dedicated 5 kW klystron that provides a 1497 Mhz rf driving signal to the cryomodule. The straightaways on the Jlab track each have 20 cryomodules for a total of 1.2 GeV of energy gained upon one circulation (normally referred to as a "pass").

Groups of electrons with differing energies can be accelerated at the same time in a linac. Once the electrons leave the injector, they are already highly relativistic. Changes to their energy produce virtually no change in their velocity. This allows electrons to be re-circulated through the linacs, to remain in phase with electrons of different energies, and continue to be accelerated at the accelerator operating frequency. There is a separate arc beamline for each of the five possible electron energies in the beamline. The electrons are steered magnetically around the accelerator arc after being separated by a spreader magnet into the component energies.

At the southern end of the linac, the beam is extracted and separated by an rf separator. Based on the phase of an electron bunch within the 499 Mhz cycle, that bunch is deflected from the beamline to one of the three experimental halls.

Beam quality tests and measurements are performed by the accelerator crew before the beam enters the hall. In addition to the measurements made in the accelerator beamline, each hall has its own dedicated beam diagnostics. In particular: current, beam position, beam polarization, and beam energy measurements can be accomplished post main beamline separation.

5.2.3 Beam Current Measurement

During normal operation, the so-called "Beam Current Monitors" (BCM1 and BCM2) are used to measure the current of the beam entering the hall. These devices both use the same measurement technique. They are rf cavities constructed to oscillate at 1/3 of the accelerator operational frequency. Specifically, their TM_{010} mode of oscillation is the same as the electron bunch frequency in the Hall C beam. A pickup antennae and accompanying electronics convert the signal caused by the excitation of the cavity to a DC voltage. That voltage signal is then sent through a voltage-to-frequency converter and then to a scaler that is read out by the DAQ system every two seconds. The cavity was designed so that the TM_{010} mode is the operational frequency of the accelerator, because the cavity response at this mode is insensitive to the beam position.

The BCMs have a gain that drifts slowly over time. Consequently, it is necessary to recalibrate them periodically to ensure that accuracy of real-time measurement of the current. In order to calibrate the BMCs, a third beam current measurement device is used. An Unser style current monitor with a stable gain was used to obtain an absolute measurement of current and calculate the correct gain for the BCMs. The Unser has an unstable zero offset, which makes it unsuitable for real time monitoring of the beam. Periodic calibrations are performed using the Unser in order to check the gain of the BCMs. The Unser is a parametric current transformer and is described in Ref. [34].

5.2.4 Beam Postion Monitoring

The beam position is monitored using rf cavities similar to the BCMs. Four antennae are attached to the cavity, and the position of the beam within the cavity can be calculated from the signal from the four antennae. Using this technique, the position of the beam at a BPM can be determined to within 1 mm. A more precise measurement

of the beam position along the hall beam line can be determined using the superharp system–a set of two vertical and one horizontal wires strung on a frame that can be scanned across the beam. The signal induced in the wires as the frame moves them across the beam path can be used to calculate the position of the beam to within 20 μm [35]. More information on the the BPMs can be found at [36].

5.2.5 Beam Energy Measurement

The measurement of the energy of the electrons entering the hall is accomplished by using the beamline itself as a magnetic spectrometer. The beam being sent to Hall C is magnetically guided along an arc from the rf separator into the experimental hall. During an energy measurement, the magnetic components within the Hall C arc that adjust the beam profile and focus are switched off, and only the dipole magnets used for steering are left functional. Superharp position monitors placed at the beginning and end of the arc can determine the beam's position pre- and post-deflection. The precise beam position and knowledge of the magnetic field integral along the path of the beam allow for an accurate calculation of the beam momentum. Once this momentum measurement is complete, the quadrupoles and sextupoles can be switched on. Another BPM in the midpoint of the arc can then measure the fluctuation of the beam's position about a central point, and that fluctuation can be related via the absolute calibration to the electrons fluctuation about the central energy. The precision of this energy measurement is $\approx 5 \times 10^{-4}$ $(\delta p/p)$. A more detailed description of the energy measurement procedure can be found at [37].

5.2.6 Beam Polarization Measurement

Theoretically the polarization of the electrons ejected from the photocathode can be determined solely from the diode laser polarization. However the polarization of the beam entering the experimental hall is affected by spin precession and by inefficiencies

in the beamline during circulation. The electron precesses during its trip around the accelerator, and the final polarization at the hall depends on a complex combination of the number of passes, the Wien filter angle, and the acceleration per pass to each of the halls. Consequently it is necessary to have an accurate measurement of the polarization in the Hall C beamline. A Møller polarimeter was constructed for this purpose [38].

Møller scattering is the scattering of two electrons from one another ($e^- + e^- \rightarrow e^- + e^-$). Its cross section is easily calculable, as it is a pure QED process between two leptons. If one introduces a polarization to the target and incident electrons that is collinear with the incident electron momentum, the cross section for the process is

$$\frac{d\sigma}{d\Omega} = \left[\frac{\alpha(4 - \sin\theta^2)}{2m_e\gamma\sin\theta^2}\right]^2 [1 + P_b P_t A_{zz}(\theta)] \tag{5.2}$$

in the center of mass frame. The beam and target polarization is P_b and P_t respectively. The factor in square brackets is the unpolarized cross section. The second term contains the polarization dependent effects. $A_{zz}(\theta)$ is called the analyzing power and is a function of the scattering angle θ. It is a maximum at $\theta = 90°$. Clearly the cross section asymmetry for scattering with parallel and anti-parallel target spins is equal to the product of the analyzing power, the target polarization, and the beam polarization. The analyzing power is determined solely by the scattering angle. The target is an iron sheet passively polarized by using a 4 T magnetic field, and the polarization of the target is consequently well understood and quantifiable. Thus by measuring the cross section asymmetry, the beam polarization can be easily calculated.

Møller data was taken periodically throughout the experiment. One cannot assume that during an experimental run that the beam polarization is that of the most recent Møller measurement. The beam energy drift can cause a significant change in the beam polarization. Dave Gaskell performed a fit to all of the good Møller data

for the experiment. So for a given number of passes, the beam polarization can be expressed as a function of beam energy, Wien angle, and the quantum efficiency as reported by the accelerator. The fit, documentation for the fit, and a talk on the Møller polarimeter can be found in the SANE wiki [39]. The polarization measurements by experimental run are shown in Fig 5.5.

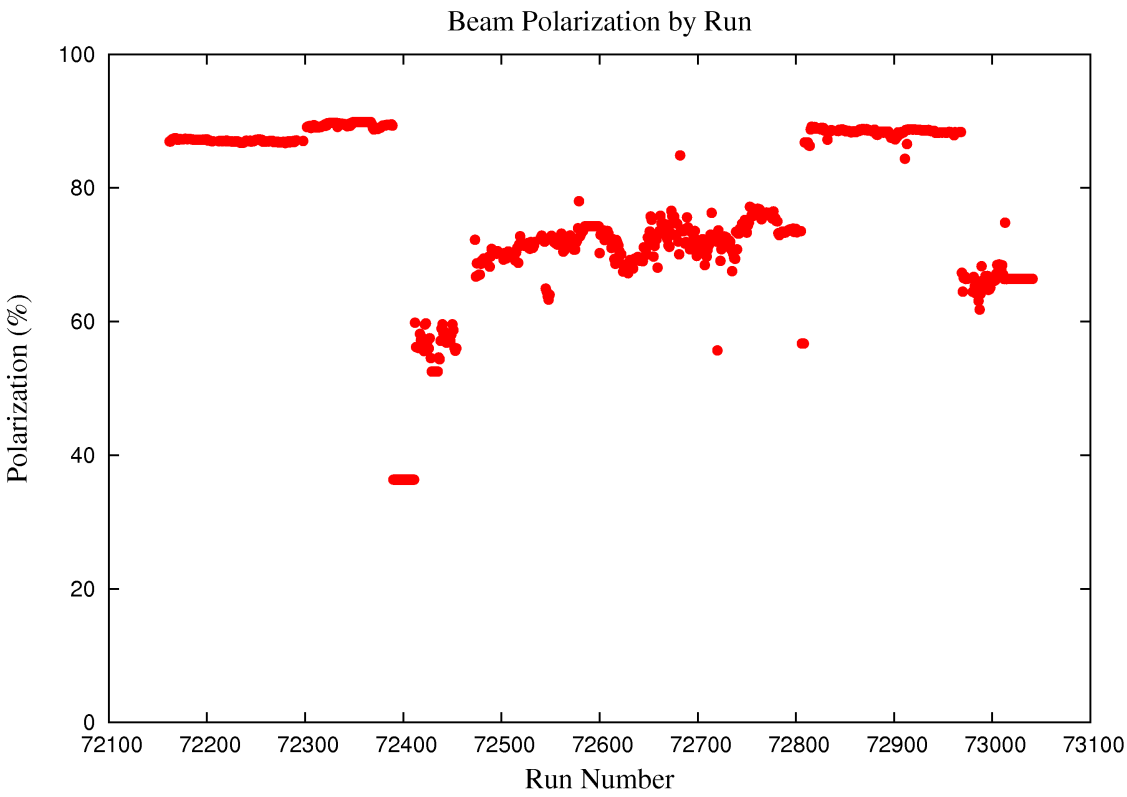

Figure 5.5: Per run beam polarization as given by a fit to the Møller data.

5.2.7 Raster System

Experiments that use solid polarized target require a raster system to disperse the beam over the target's beam-facing surface area. The the standard JLab raster spreads the beam over 2 mm $\times$ 2 mm. The target, which will be discussed in detail later, is a cylinder of frozen ammonia beads with a diameter of approximately 2.5 cm. The coil that serves as a pickup for the polarization measurement is a single loop

about a half inch in diameter, embedded directly in the target material. The coil of thin tubing samples the polarization in a region around it. The beam damages the target material as it passes through. This damage to the material causes depolarization of the material over time. Spreading the beam out with a wider raster reduces the radiation induced depolarization rate. Spreading the beam uniformly over most of the target ensures that the coil is embedded in the material being impinged upon by the beam. The spread of the beam is accomplished using two deflecting magnets driven by three signal generators to create a spiral pattern that maintains a constant beam flux over the area it sweeps out. This spiraled raster pattern fills a circle of diameter 2 cm.

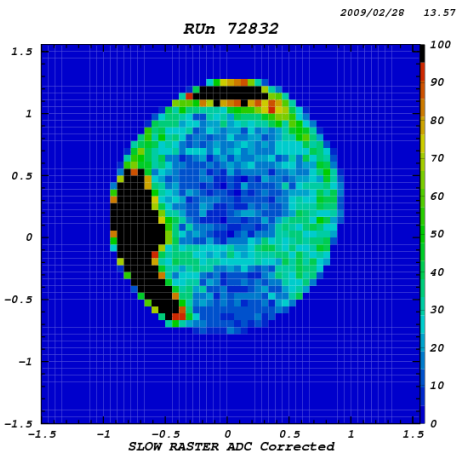

Figure 5.6: Run 72832 events binned by slow raster ADC y vs x values. This run was to confirm target ladder location. One can see in the image the top of the microwave horn, 10mm hole, and 8mm hole in the aluminum frame.

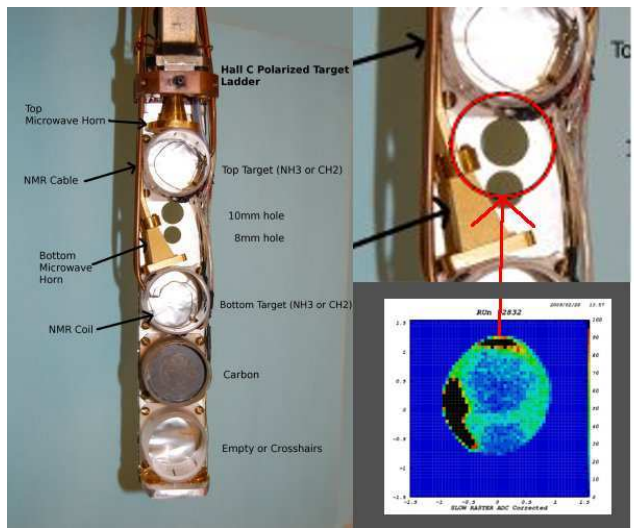

Figure 5.7: Left: Target ladder Top Right: Close-up of the of the 10mm and 8mm holes Bottom Right: Events binned by slow raster ADC values. The beam spot location for this image is circled on the picture above.

The signals driving the magnets are sent to ADCs and recorded by CODA (section 5.4). The raster signal data allows for the calculation of the beam position within the raster given a time stamp. Plotting the x versus y position of the raster for events in the main detector produces an effective photograph of the target. The width of

the slow raster can be checked by imaging a 10mm hole in the aluminum frame of the target at low current. The picture in Fig. 5.6 shows the histogram of slow raster ADC signals for a run targeting the 10 mm hole in the target ladder for location confirmation. The histogram was also sliced and profiled in order to obtain a direct measurement of the raster width.

More details on the slow raster design and set up can be found in [40].

5.2.8 Chicane and Helium Bag

The magnetic field of the target is strong enough to change the trajectory of the beam. For unpolarized targets or when the magnet is aligned with the beam direction, the unscattered (or shallowly scattered) particles continue through the target in a straight line to the beam dump. The beam dump is designed to absorb these particles, and it is shielded from the rest of the hall in order to minimize the radiation exposure in the hall. Exposure of any other part of the hall to the beam would create a radiation hazard. For the 80° field configuration, an electron approach from the beam line would result in its deflection in the target field such that for some beam energies the electrons would never hit the target and the beam would be deflected into the floor.

When the target is oriented such that the field is parallel or anti-parallel to the beam line, no change in the beam's trajectory occurs ($\vec{v} \times \vec{B} = 0$). When the target field is oriented 80° relative to the beam, the beam is bent downward. The target was installed and kept for the entire experiment at the same level as the beamline. Two dipole magnets were placed in the hall along the beam line just upstream from the target. The first dipole was positioned so that it bent the beam downwards, and the second so that it bent the beam upwards towards the target. The approach of the electrons to the target was changed so that as they entered the target field from below and were deflected, the angle of approach became horizontal just at the center of the target. A low current dump was constructed to absorb the deflected beam in the 80°

Beam Energy	BE$\int Bdl$	BZ $\int Bdl$	Target $\int Bdl$
4.7 GeV	1.002 Tm	0.513 Tm	1.521 Tm
5.9 GeV	1.002 Tm	0.519 Tm	1.521 Tm

Table 5.1: Chicane Settings for different beam energies. BZ is the label for the first magnet and BE the label for the dipole magnet closest to the target.

configurations. The field settings for the chicane magnets is shown in table 5.1.

To prevent hazardous ionization and activation of the air in the hall, the beam passing through the hall must be shielded from the surrounding atmosphere. Normally this is accomplished with an evacuated beam pipe similar to what is upstream of the target. Rather than build different evacuated housings for each energy setting (as would be required because of the energy dependent deflection in the target field), a large, nearly conical mylar bag filled with helium encompassed the beam's path to the beam dump.

5.3 Target

5.3.1 Introduction

The SANE target was a frozen ammonia target provided by the UVA solid polarized target group. The system is composed of several subsystems. A large superconducting magnet provides the field in which the protons in the target material are polarized. A refrigeration system maintains the temperature necessary for polarization of the material. The technique used to polarize the material uses microwaves to induce spin flips. An NMR system measures the polarization of the target in real time.

Ammonia ($^{14}NH_3$) was used as the target material. Only events from the hydrogen nuclei in ammonia are relevant for SANE analysis, so one might wonder why not use molecular hydrogen in order to avoid dilution due to the inclusion of the nitrogen

nuclei. Molecular hydrogen, when cooled, devolves into a magnetically inert state with spin zero, and is therefore unpolarizable. Hence, one must look elsewhere to molecules containing hydrogen. Ammonia has a high free proton density, good polarization characteristics, and good resistance to radiation damage. These characteristic will be discussed as they relate to the experiment in the following sections. First the mechanism used to polarize the target will be described.

5.3.2 Dynamic Nuclear Polarization

The application of a magnetic field to particles with magnetic moments splits the existing energy states into additional Zeeman energy levels. If we assume the particles themselves are weakly interacting, the ratio of the populations of these states within a field of strength B, and a temperature T is given for spin 1/2 particles by the Boltzmann distribution:

$$\frac{N_\uparrow}{N_\downarrow} = \exp\left(\frac{-\mu B}{k_B T}\right) \tag{5.3}$$

where $N_{\uparrow(\downarrow)}$ is the number of particles in the aligned(anti-aligned) state. The polarization as typically defined by

$$A = \frac{N_\uparrow - N_\downarrow}{N_\uparrow + N_\downarrow} \tag{5.4}$$

is then given by

$$P = \tanh \frac{\mu B}{2k_B T}. \tag{5.5}$$

For a 5 T field and a refrigeration system that can keep the system at 1 K, the thermal equilibrium polarization is approximately 0.3% for the protons and 93% for electrons– the difference being due to the much weaker magnetic moment of the proton. Clearly a mechanism other than brute force polarization is needed for increasing the proton polarization to a value at which spin asymmetries are detectable. Dynamic Nuclear Polarization(DNP) can accomplish this by driving transitions that transfer electron polarization to the nuclear species in the material. There are two mechanisms that can

effect this transfer. The first, the *solid state effect*, is the dominant process in materials with low electron density and discrete energy levels. It works through the driving of otherwise forbidden transitions. DNP in materials with a high electron density is more accurately described by the heating and cooling of thermal spin reservoirs.

Both mechanisms will be described below. The solid state mechanism is a straightforward intuitive way to think about DNP, and is most often valid for chemically doped substances. The polarization of materials such as NH_3 and LiD, which are irradiated in order to create paramagnetic centers, proceeds through the *equal spin temperature* mechanism.

5.3.3 Solid State Effect

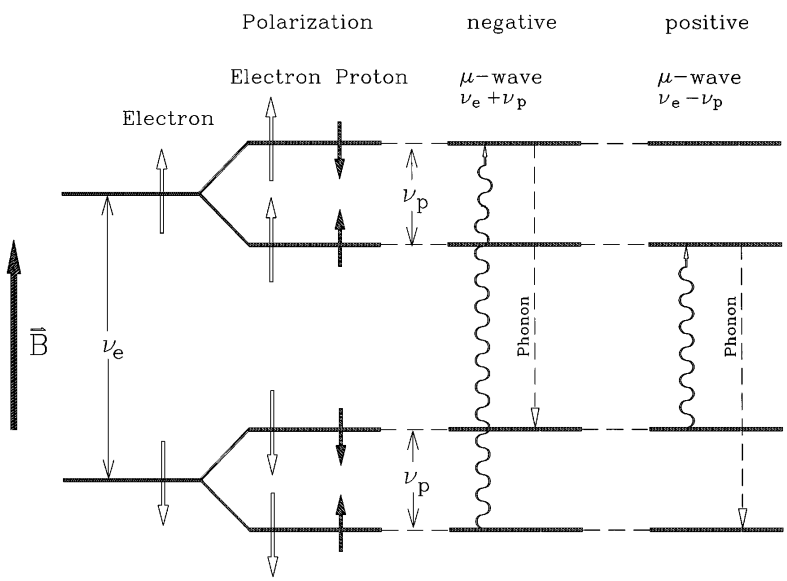

Figure 5.8: Zeeman energy levels for electron spin states and coupled electron-proton spin states. Filled arrows denote electron orientation. Open arrows denote electron spin states. The microwave driven transition is indicated by the wavy lines, and the dashed line shows the decay via phonon exchange with the lattice. Graphic from Ref. [1].

The application of a magnetic field to target material splits an electron or proton energy level into two Zeeman energy levels. The electron and proton populations are

split between the new states with their spins aligned or anti-aligned with the magnetic field. The distribution of the population between these states is given by equation 5.3 for thermal equilibrium. In order to polarize the protons in the material, one could attempt to drive the NMR transition between the Zeeman levels, flipping the proton spin. Such an attempt would actually result in zero polarization, because the transition probability for a proton to move between the Zeeman levels when excited by a field at that frequency is equal for either direction.

In addition to Zeeman energy levels, hyperfine splitting occurs when electrons couple to protons. This splitting, which results in four different levels for a coupled electron-proton pair, is shown in figure 5.8. If one drives a transition that flips both spins of the coupled pair (Fig. 5.8), the electron will quickly decouple and relax back into its previous state, leaving the proton behind in its new spin state. The electron is then free to couple to another proton and repeat this process, gradually populating the proton Zeeman level. This mechanism relies on the difference in proton and electron relaxation times. The proton has a relaxation time of about 30 minutes at 1 K [1]. The electron has a relaxation time on the order of seconds. Thus the rate of population decay of a proton state is much lower than the population increase rate, which is only limited by the much shorter electron transition timescale. Thus the population of a given proton Zeeman state decays slowly towards the thermal equilibrium value, while at a much higher rate relatively small number of paramagnetic electrons continue to couple and facilitate the transition of other protons within the material to the desired spin state. Using this mechanism also allows for reversal of proton polarization simply by adjusting the microwave frequency to drive the other double spin-flip transition, without the need to adjust any other system parameters (such as the magnetic field). Figure 5.8 shows the two sets of transitions associated with positive and negative polarization.

Protons are polarized in a region local to the free electrons. The polarization

spreads across the material through a mechanism called "spin diffusion" [1]. Protons coupled to each other via the material lattice can undergo an energy conserving double spin flip. Thus, neighboring particles can swap polarization states, and the polarization achieved in the region local to the free electron can diffuse through the material.

5.3.4 Equal Spin Temperature Theory

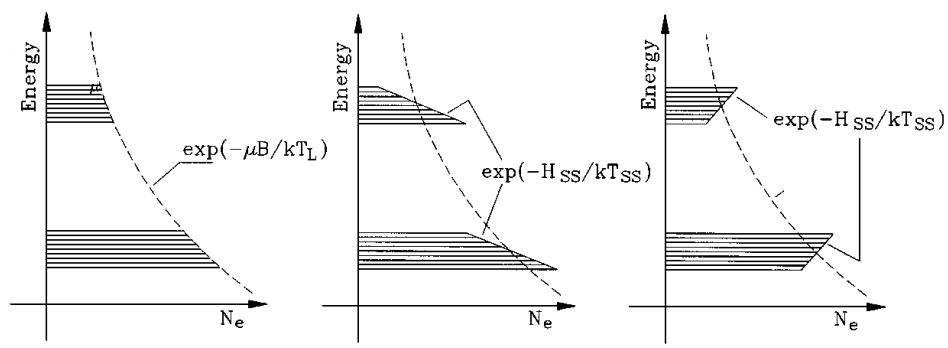

Figure 5.9: Illustration of the population of the electron energy levels with various spin-spin reservoir temperatures. In all graphs $T_L = T_{Ze}$. Left: The spin-spin reservoir is in thermal equilibrium with the latice, $T_L = T_{ss}$ Middle: Positive spin-spin reservoir temperature with $T_{ss} > T_L$ Right: Negative spin-spin reservoir temperature with $T_{ss} < T_L$. Graphic from Ref. [1].

In the Solid State Effect model described above, polarization is transferred from the electrons to the protons via a hyperfine coupling and the driving of a transition whose energy level is determined by the magnetic moment of the species involved. This model predicts that if there were more than one spin species in the material (say a nucleus), then that species would reach maximum polarization only when irradiated by the frequency corresponding to the energy gap between the states bridged by the spin-flip. In materials with a high electron density, this is found not to be the case. For example, in ammonia the polarization of the nitrogen nuclei is observed to be dramatically increased while driving the transition that polarizes the proton [1].

The equal spin temperature theory describes a different mechanism through which polarization occurs and predicts the simultaneous polarization of species with different magnetic moments.

With high concentrations of electrons, the spin-spin interactions, while weak, cannot be ignored, as they result in a smearing out of each of the Zeeman levels of the electron as shown Fig. 5.9. Rather than a discrete state, there is around each Zeeman level a band of energy levels occupied by the electrons. The distribution of states resulting from the spin-spin interaction are described by a Hamiltonian, H_{ss}, and a characteristic temperature T_{ss}. Writing down the Boltzmann distribution for these bands, one obtains $\exp(-H_{ss}/k_B T_{ss})$, which is illustrated in figure 5.9. Similarly the proton(electron) distribution between two Zeeman levels is described by a characteristic temperature $T_{Zp(e)}$ and Hamiltonian $\mu_{p(e)}B$. Given enough time for relaxation and no excitation from radiation, these three thermal reservoirs will fall into thermal equilibrium with the lattice of temperature T_L; the temperatures will equalize, giving the thermal equilibrium polarization from the first part of this section– equation 5.5 with T being the lattice temperature.

During DNP, the microwave radiation is absorbed by the electron spin-spin reservoir, and thermal contact between it and the proton Zeeman reservoir leads to polarization. Specifically, energy $h(\nu_e - \Delta)$ is absorbed from the microwave field. The energy $h\nu_e$ transitions an electron between Zeeman energy levels, while a $h\Delta$ quanta is absorbed by the spin-spin interaction(SSI) reservoir. The absorption of Δ by the SSI resevoir leads to a heating or cooling of the reservoir depending on the sign of Δ. The spin temperature T_{ss} shifts accordingly as the population redistributes itself within the bands, and this can lead to positive or negative T_{ss}.

Thermal contact between the SSI reservoir and the proton Zeeman reservoir leads to the equalization of T_{ss} and T_{Zp}. The process that causes the heat exchange between the two reservoirs is a spin flip of two electrons of opposite spins. This spin flip does

not change the energy of the electron Zeeman reservoir, but the spatial rearranging of the electrons leads to an energy loss (or gain) by the spin-spin interaction reservoir. This exchanged energy is absorbed by the proton Zeeman reservoir, changing the spin populations accordingly. Thus the energy exchange between the reservoirs brings T_{Zp} to T_{ss}. T_{ss} is determined by the microwave cooling, and so the microwave cooling is a direct handle on the polarization of the proton. Furthermore higher intensity microwaves increase the polarization rate, provided the refrigeration system can handle the increased thermal load.

If there is any process that provides thermal contact between the spin-spin interaction reservoir and another Zeeman reservoir, the spin species associated with that reservoir will be polarized as well. Evidence for this contact has been seen in frozen ammonia where nitrogen polarization occurs during the driving of transitions to polarize the hydrogen nuclei. Polarization for any body with a magnetic moment $g_i\mu_i$ in the material is given by

$$P = \tanh \frac{g_i \mu_i B}{2k_B T_{ss}}. \tag{5.6}$$

The final polarization is given by that specie's magnetic moment and the SSI temperature. Hence in ammonia, once the proton's polarization is determined, the spin-spin temperature can be calculated, and the nitrogen nucleus polarization determined. The observed nitrogen polarization data fits this model neatly and can be seen in reference [1].

5.3.5 Target Cryogenic and Microwave Setup

An Oxford made 5 T magnet provided the target field for polarizing the target. The magnet is a super-conducting Helmholtz style magnet with a cryostat that serves as a liquid helium supply for the target refrigeration system. The cryostat liquid helium

and nitrogen was supplied by the JLab Central Helium Liquefier. Helium from the magnet cryostat was siphoned into the ^{4}He refrigerator to cool the target.

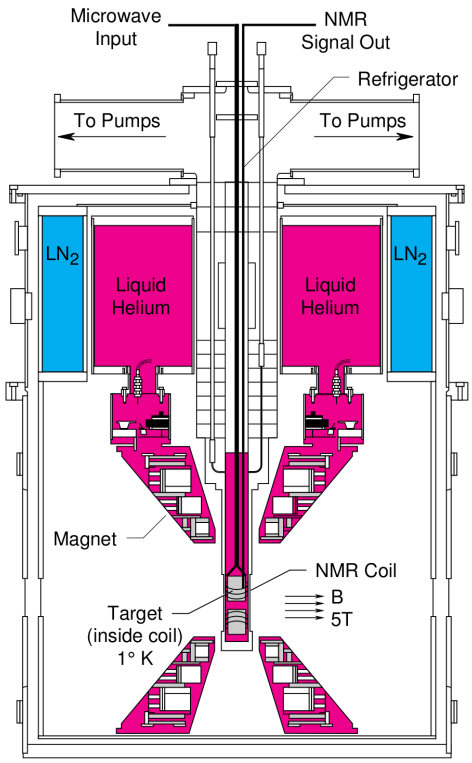

Figure 5.10: Cross Section schematic of the UVA target used for SANE

The refrigerator is a ^{4}He evaporation fridge with cooling power of about 2 W and an operating temperature around 1 K. This cooling power is needed to remove heat from the beam (about 0.45 W at 80 nA) and heat from the microwaves used for DNP (about 1 W). The removal of the evaporated helium is accomplished with a set of mechanical pumps and roots blowers. The target material sits in a pool of liquid helium that is cooled by evaporation. The helium removed from the target nose reservoir is replenished by drawing helium from the cryostat and sending it through a series of heat exchangers and then into the nose. The heat exchangers are cooled by the gas being pumped out of the refrigerator, so that the 4 K helium drawn out of the magnet cryostat and condensed in the separator of the fridge is cooled before

it gets to the 1K reservoir in the nose wherein sits the target material.

Through the central shaft of the refrigerator is the "target insert." The target insert houses connections for the NMR, the microwaves, thermometry, and heater wire. At the bottom of the insert is an aluminum ladder that holds target cups. Figure 5.11 shows the target ladder for one of the inserts. The target cups are cylinders 1.145 inches deep with a diameter of 1.12 inches, containing beads of frozen ammonia. A cross section of the target setup is shown in Fig. 5.10

The microwave transmission horns can be seen above each of the target cups. Inside of each cup is a loop of wire used as NMR pickup antennae. A carbon cell is used for collecting data for calculation of packing fractions. The bottom cell can be empty, or it can contain wire cross hairs for use in positioning. The 10mm and 8mm holes can similarly be used in positioning, see 5.2.7. Platinum and chip resistors on the side of the target cups and thermocouples inside of the cups are used for temperature measurement. Details on the construction of the insert and the instrumentation used can be seen in the UVA target group's internal documentation [41].

The microwave energy used in polarization is carried to the target through waveguides in the target insert. The microwaves were generated in an Extended Interaction Oscillator (EIO) tube at a frequency around 140 GHz and can be tuned using a mechanical bellows by ± 2 GHz in order to drive the positive or negative polarization transition. The EIO tube and accompanying microwave equipment were placed on a platform just above the cryostat and controlled and monitored remotely during the experiment. The microwave frequency and power were monitored during the running by a target operator. The frequency at which optimal polarization is achieved shifts while polarization is building up and while beam is being applied to the target. The local field around the nuclei and free radicals is affected by the free radical density. The density changes as the beam damages the target material. The changing local field causes a shift in optimal microwave frequency for polarization. It is necessary

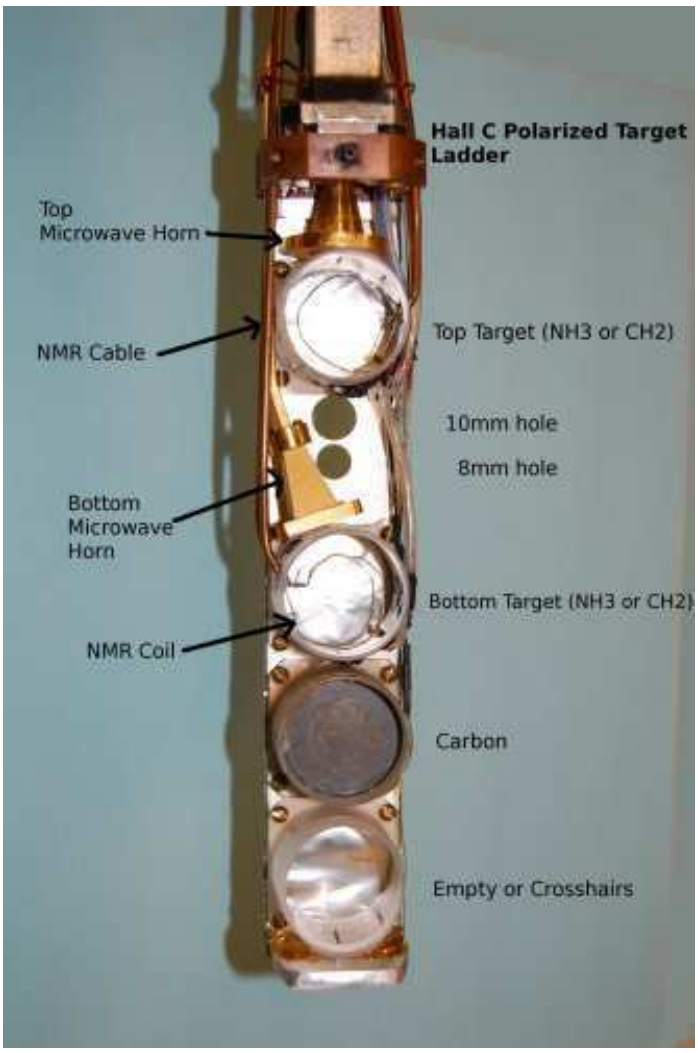

Figure 5.11: Target ladder.

to monitor the polarization and continually adjust the microwave frequency in order maintain maximum polarization. An adjustment of a few megahertz approximately every half hour was sufficient to prevent unnecessary decay in polarization.

5.3.6 Polarization Signal Processing

The measurement of the polarization was accomplished by measuring a nuclear magnetic resonance signal at the Larmor frequency of the proton at 5 T. The NMR measurement was taken using a Q-meter connected to a resonant circuit (Fig. 5.12). The inductor of the circuit is a coil placed directly in the target material. If the

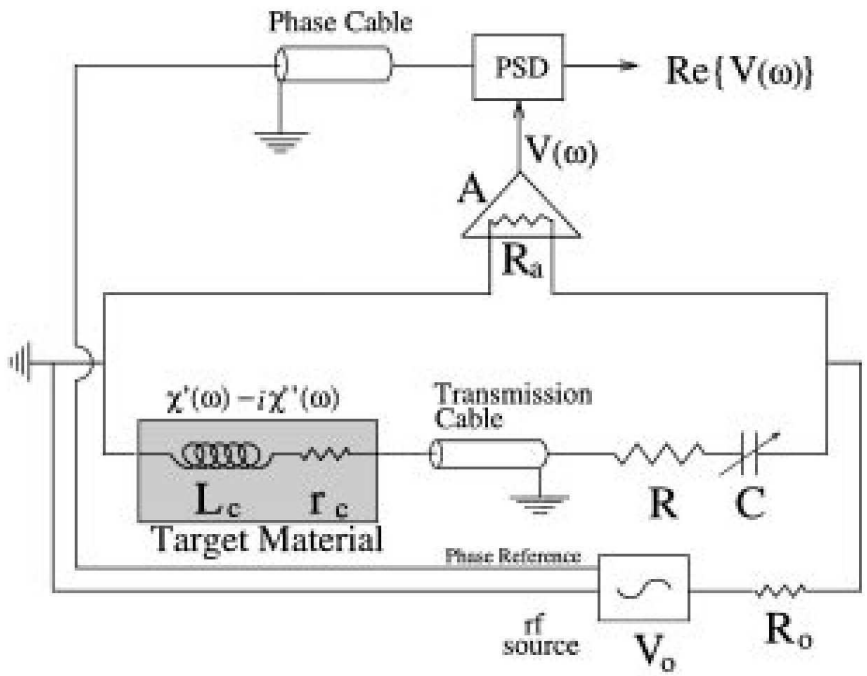

Figure 5.12: NMR circuit including the LRC components and the Q-meter used for polarization measurement [1].

NMR coil has inductance L_C and resistance r_C, then the impedance of the coil will be $Z_C = r_C + i\omega L_C(1 + 4\pi\eta\chi(\omega))$. The inductance of the coil is modified by a factor $\eta\chi(\omega)$, with η being the filling factor and $\chi(\omega)$ the susceptibility of the material. The susceptibility can be broken down into an absorptive and dispersive term: $\chi(\omega) = \chi'(\omega) - i\chi''(\omega)$. The integral over the absorptive part of the impedance is proportional to the polarization of the material:

$$P \sim \int_0^\infty \chi''(\omega) d\omega. \tag{5.7}$$

An RF signal is sent to the LRC circuit, and the response of the circuit measured by the Q-meter. The RF signal's frequency is modulated about the Larmor frequency of the proton. The absorptive part of the output signal is isolated by a phase sensitive detector that uses the input RF as a phase reference. The output signal has Q-curve contribution from the Q-meter circuit itself. This Q-curve contribution can be

separated out by measuring the circuit response with the Larmor frequency shifted outside the range of the modulation by lowering the magnetic field. Once the Q-curve is measured, it can be subtracted out, and the result should be the integral from eq 5.7 times a calibration constant that depends on the state of the NMR circuit. The calibration constant can be determined by doing a polarization measurement while the material is at a known polarization. A signal measurement while the system is at thermal equilibrium, provides this. The polarization is determined by the temperature and field (Eq. 5.5).

During the production runs, the material is measured about every thirty seconds by the NMR system. The coils in the material carry a frequency modulated signal with a central frequency of 213 MHz (The Larmor frequency of a proton in a 5 T field) and sweep range of 400 kHz on either side. The frequency sweep is linear in time with a period of 1 ms. The NMR output signal is the sum of the Q-curve and the frequency dependent response of the circuit due to the polarized target material, Eq. 5.7. Figure 5.13 shows the Q-curve; the raw NMR signal from which the Q-curve is subtracted, and the polynomial fit to the signal ends. The polynomial signal is necessary, as during the run the signal can gain a dc-offset and the Q-curve may change slightly due to temperature variations in the circuit. In order to process the averaged signal from a 30 s sweep, the baseline is subtracted, a fit is performed to the ends of the signal, and the resulting curve is subtracted from the signal to remove any DC offset or slight changes to the Q-curve. The result is a processed signal like that shown in Fig. 5.14. The integral is taken over the filled in area from Fig. 5.14, and the polarization is calculated by multiplying the area by the calibration constant obtained in the most recent thermal equilibrium measurement. Polarization measurements are taken on intervals at about 30 s to 60 s depending on the noise in the signal. For the analysis, a beam charge weighted average of the polarization is taken for each run. That run is then assigned a target polarization value equal to

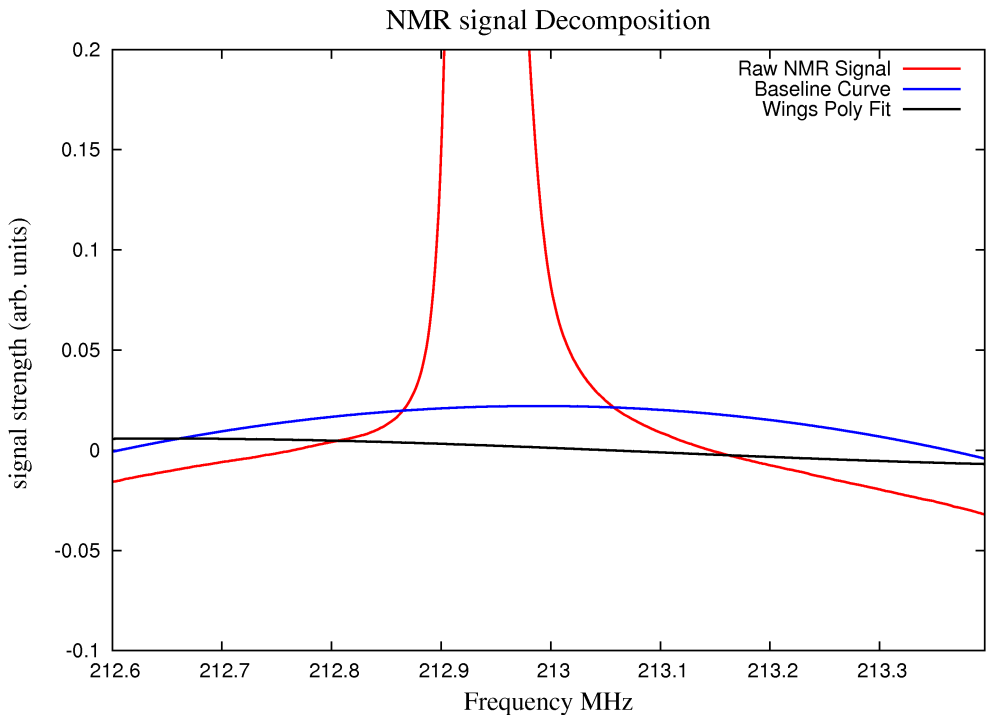

Figure 5.13: Stages of NMR signal processing. The area under the peak in the center of the raw NMR signal is the quantity of interest. The curve the raw signal sits on is the "baseline curve" plus the "poly fit" curve. These two curves are subtracted from the raw signal to obtain a curve that is proportional to the absorptive term in the material's magnetic susceptibility.

that average. A cut on beam current was placed at 60 nA when including data in the average. The polarizations assigned to each run are binned in Fig. 5.15. A plot of the charge averaged polarization for each run used in the data analysis is shown in Fig. 5.16. The average for the entire experiment is 68%.

5.3.7 Error Estimate

When measureing the constant relating the NMR signal area to the polarization, one must be sure that the system has reached thermal equilibrium (TE). Failing to wait for thermalization before taking the measurement, or fluctuations in temperature during the measurement, will cause the calibration constant to be incorrect by some amount, depending on how close the system was to TE at the measurement time or the

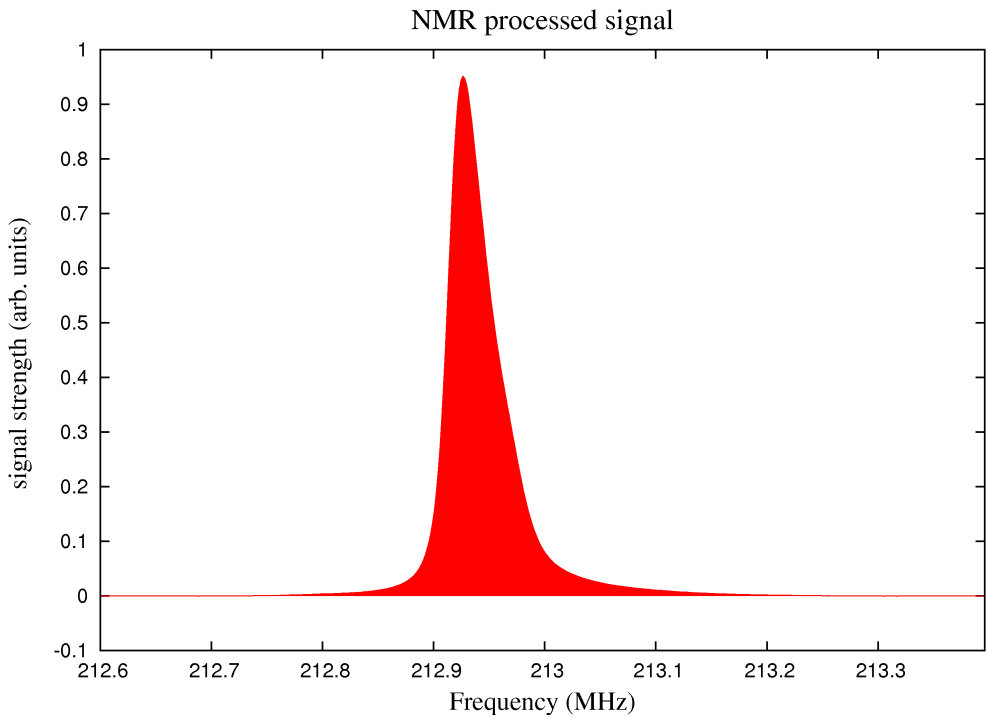

Figure 5.14: Processed NMR signal. The integral of shaded region is proportional to the right-hand side of Eq. 5.7.

magnitude the fluctuation. The sample spread over an individual measurement gives about a 3% error in the polarization calculation. Those uncertainties are generally smaller than the variation between different TE measurements for the same material.

Looking at the calibration constants (see Fig. 5.17), one can see that for a single target load there can be a significant spread in the TE measurement. This spread is the primary source of uncertainty in the calculation of the proton polarization. The variation between TE measurements results can be due to a number of things: shifting of target material near the coils, taking a measurement away from thermal equilibrium, or a large change in the Q-meter circuitry temperature. The error in the polarization is estimated to be the error propagated from the calibration constants. An error in each target load calibration constant is taken to be either the statistical error of the measurement when only one TE measurement exists or the standard deviation of the points where there are multiple TE measurements for single loads.

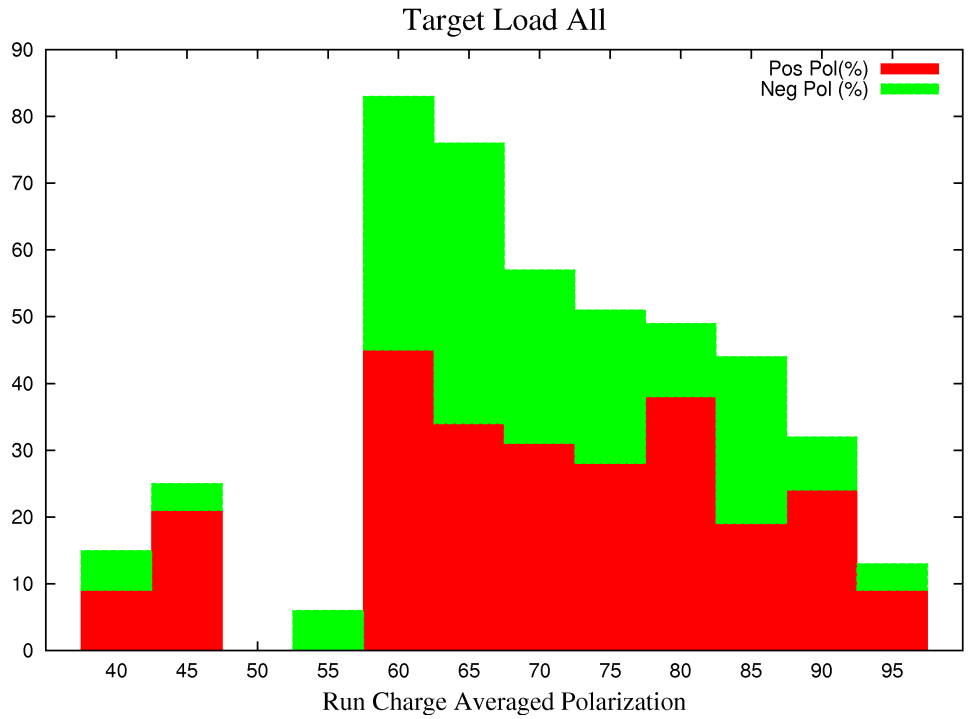

Figure 5.15: A histogram of all run polarization values. Negative and positive polarizations are distinguished by color.

The calibration constant used is the error weighted average of all TE measurements for a load. An overall conservative error is used and estimated to be the average of the standard deviations of the target load TE measurements. This gives a relative error estimate in calibration constant of 4.1%, which is adopted as a conservative relative error for the polarization.

5.3.8 Lifespan of a Target Load

The beam damages the target material during the experiment through spallation and ionization. The damage inhibits DNP processes, and lowers the maximum achievable polarization with the available cooling power and microwave power. The inhibition of DNP occurs because the damage produces a variety of radicals that interact with the protons and increase their relaxation rate. As damage occurs over a series of runs, the number of these radicals continues to increase. It is possible to rid the target material

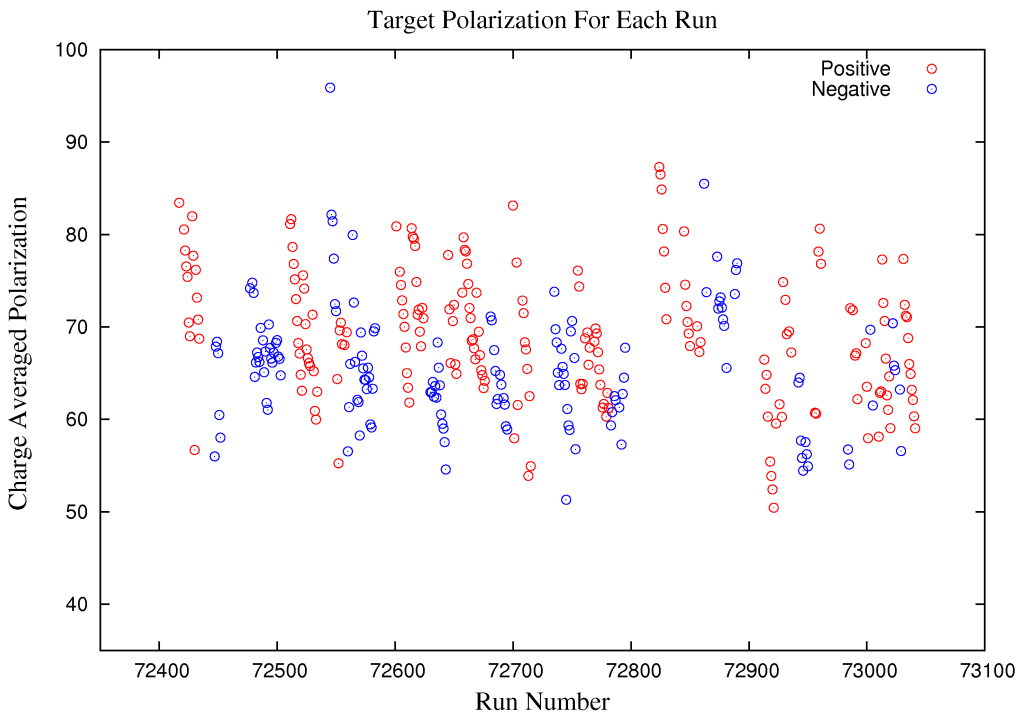

Figure 5.16: Polarization assigned to each run in the analysis.

of these radicals in a process called "annealing." During an anneal, the temperature of the material is raised to slightly above liquid nitrogen temperatures. Heating the material for about 30 minutes at 90-100 K decreases the inhibiting radical density and lowers the relaxation rate of the protons in the material, thus raising the possible maximum polarization back to essentially its starting value. The depolarization rate per charge is also slightly increased. Consequently, the material must be changed once the depolarization rate is high enough to cause the time cost of more frequent anneals to be greater than the time cost of uninstalling the insert from the fridge, swapping in new material, and reinstalling the insert. An in depth look at radiation damage can be found in [42], and [1] gives a description of the damage mechanism and a comparison of damage in various materials.

The life time of target load all the target loads is shown in Appendix A. The target polarization continually decreases while the beam is on. The beam heating interferes with the polarization process, and during the beam down times, the lowered target

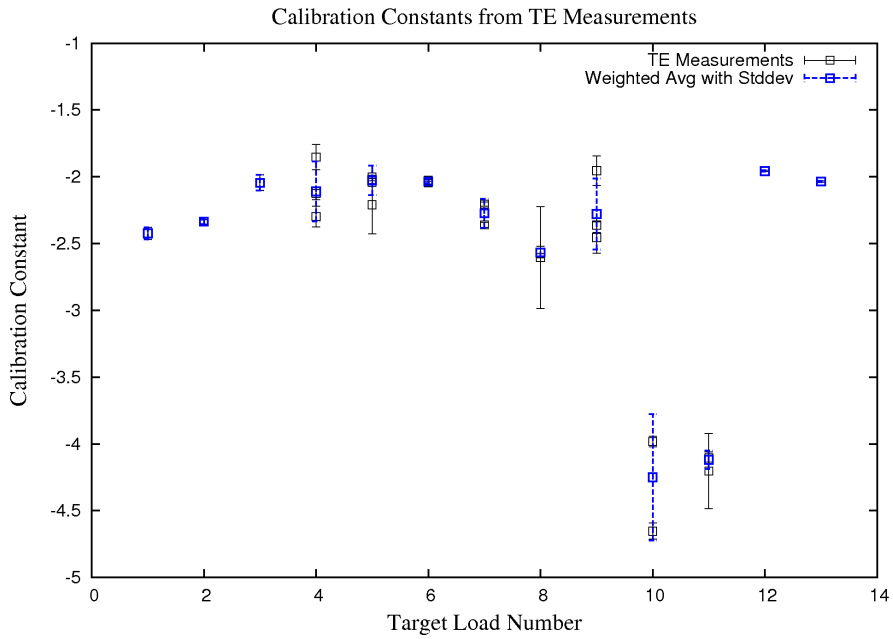

Figure 5.17: Calibration constants plotted by the target load index. The errors shown are the statistical error in the TE measurement. The separate measurements are shown along with a point represented the error weighted average when multiple measurements exist for a single target load.

temperature allows an increase in polarization. Rises in polarization during a run run is indicative of beam down time or beam trips. The microwaves were tuned by hand, as the optimal polarization frequency shifts with the radiation dose on the target. Gradual rise or unexpected fall of the target polarization during the experiment runtime is due to sub-optimal tuning of the microwaves. In a few cases, the polarization of the material drops off suddenly, and that is due to the loss of helium in the target cavity. The beam and microwave heating immediately destroys the polarization in the absence of refrigerant.

5.4 Data Acquisition System

Data collected during the experiment consisted of several different classes of information: Detector signals that had been processed using ADCs and TDCs; target in-

formation, which was collected by an independent DAQ computer; scaler quantities, which are used to keep track of trigger and helicity counts; and EPICS (Experimental Physics and Industrial Control System) data, which contains information pertaining to beam and accelerator operation such as BPMs, BCMs, and magnet currents.

Read Out Controllers(ROCs) read in information from the various data sources above and prepare them for read out by the Event Builder. The Event Builder accepts information from all the ROCs and organizes the data from the same trigger into an "event" in a data file for post processing. EPICS information was collected every thirty seconds, and the scaler information every 2 seconds, consequently subsequent events may contain redundant scaler or EPICS data. The triggering of the read write process by the Event Builder was controlled by the Trigger Supervisor.

The raw event files are stored on long term storage tape and copied to disk for processing. For higher level analysis, the event files are decoded, and relevant information is selected and written to ZEBRA data files that can be accessed with PAW and HBOOK routines.

5.4.1 Triggers

The Trigger Supervisor (TS) has several trigger inputs. When one of them reads a positive logical signal, the ROCS are directed to dump the data from the memory bank correlated in time with the logical signal received by the TS. The Event Builder also receives a signal from the TS, indicating with which trigger type that event should be marked. The TS input can be any discriminated or logical combination of discriminated detector signals as required by the experiment. See reference [43] for a complete description of the TS and any early Hall C thesis (J. Arrington's for example; citation [44] gives the url for JLAB Hall C's theses list) for a more complete description of the Hall C data acquisition set up and CODA (CEBAF Online Data Acquisition System).

For the SANE data, a coincidence between the calorimeter and the Cerenkov detector was primarily used as the main analysis trigger. Multiple other triggers exist as well. The relevant trigger types are described below.

- BETA1 : an above threshold signal in one of the calorimeter's groups of 64 PMTs. This trigger does not include particle discrimination, and events from this trigger could be any particle depositing energy in the calorimeter

- BETA2 : an above threshold signal in one of the calorimeter's groups of 64 PMTs and an above threshold signal from the sum of the 8 PMTs in the Cerenkov Detector. The calorimeter signal was used as a timing gate for receiving the Cerenkov detector signal to ensure coincidence. This trigger is intended to catch only electrons (or positrons) emitting Cerenkov radiation in the nitrogen tank and then depositing energy in the calorimeter.

- PION : an above threshold signal in two of the calorimeter's groups of 64 PMTs. One must be from the bottom half of the detector and one must be in the top half. A hit registering in the top and bottom half was required in order to ensure that only events with adequate cluster separation were recorded.

- HMS : a hit registered in the Hall C high momentum spectrometer– 3/4 scintillators and a cerenkov signal.

- HMS & BETA1: a coincidence between the two triggers described above. This trigger is intended to record the proton and electron from an *ep* elastic event. An analysis of these events is being performed by another collaborator.

5.5 Front Tracker

The front tracker was composed of three planes of plastic scintillators (Bicron BC-408) placed 55 cm away from the target cell. From nearest the target to furthest,

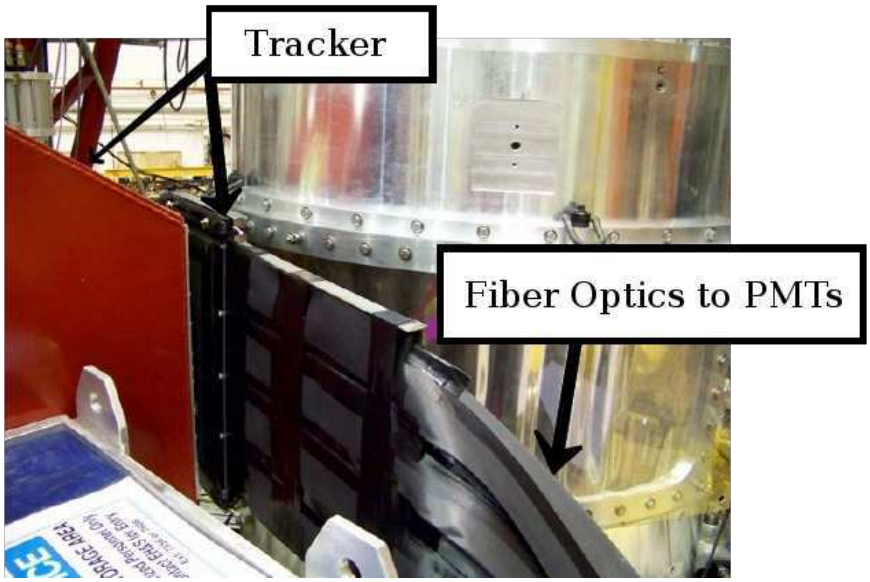

Figure 5.18: Close up of tracker location. The Cerenkov Detector (red) is to the left. On the side opposite of the Cerenkov Detector is the target scattering chamber. The actual tracker planes are hidden in the photo by the Cerenkov Detector entrance.

the planes are composed of 73, 128, and 129 side by side $3 \times 3\text{mm}^2$ strips. The first plane contains strips running vertically for horizontal tracking. The second and third are offset vertically from one another by 1.5 mm, and the strips run horizontally for vertical tracking of particles. Light produced upon the passage of a particle through one of the strips is carried by a fiber optic cable attached to the end of each of the bars to multi-channel PMTs.

The tracker was intended to discriminate electrons and positrons by detecting the vertical deflection caused by the target field (see figure 5.19). The extremely high rates caused by low energy background circulating through the target field makes the tracker data difficult to use. Since the positron dilution is only a very small correction, the full analysis of the tracker data was deferred until later.

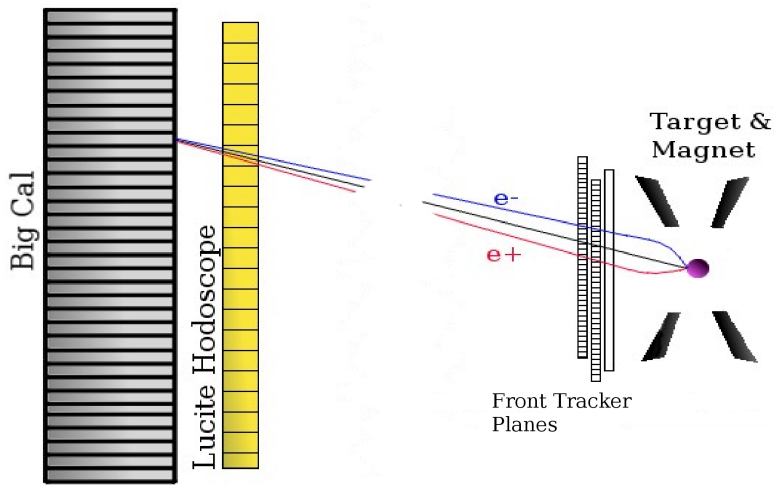

Figure 5.19: Sketch of intended function of the front tracker. View is from the side of the detector package. The black line is extrapolated by connecting the beam location for an event and the reconstructed particle hit in the calorimeter. The blue line is the path an electron would take when scattered and deflected by the field before impacting the calorimeter. The red line is that of a positron striking the same position on big cal. The sketch is not to scale and used only to illustrate the detection of the vertical deflection of electrons and protons by the front tracker.

5.6 Cerenkov Detector

Next in order, moving away from the target, was the entrance window to the nitrogen tank of the Cerenkov detector. The index of refraction of the pure nitrogen environment at atmospheric pressure was $n = 1.000297$. Cerenkov radiation is emitted when the speed of a particle exceeds the speed of light in the medium it is traveling in, $c_n = c/n$. The energies at which a Cerenkov radiation would occur in the detector tank are given in Table 5.2. With a maximum beam energy of 5.9GeV, only scattered electrons and positrons reach the threshold energy required to emit Cerenkov radiation.

The emission of Cerenkov radiation occurs at an angle $\theta = \cos^{-1}(c_n/v)$ for a particle traveling at speed v. The electrons detected will all be traveling close enough to the speed of light that the argument of $\cos^{-1}$ is $1/n$, and so the Cerenkov radiation will be emitted almost parallel ($\theta = 1.4°$) to the flight of the particle. Taking advan-

tage of this fact, eight mirrors were designed such that each mirror will reflect every ray traced from the target to the mirror's surface to a PMT dedicated to that mirror. Hence there are 8 PMTs in the detector.

Half of the mirrors were toroidal and half of the mirrors were spherical, and each was tested prior to construction to ensure the light gathered from the target location would be focused on the dedicated PMT's photocathode. The mirrors were coated to reflect 150 to 250nm light. Theoretically, with mirrors capable of reflected light within that wavelength range and a gas radiator length of 125cm, relativistic electrons should emit somewhere near one hundred photo-electrons as they travel through the gas tank [45]. The PMT detection efficiency peaks at about 330 nm, and so the production rate is much smaller. During calibration using a photodiode, the one photoelectron peak was clearly visible above and distinct from the ADC pedestal. During operation, a PMT averaged around 12 photoelectrons per event with as many as 60 being detected for some events.

Since each PMT only receives light from one of the mirrors and each mirror covers a unique solid angle, an ADC signal from one of the Cerenkov detector's eight PMTs is correlated with one of eight regions on the calorimeter. The requirement of a correlation of an energy deposition in a calorimeter region with a matching the active Cerenkov PMT eliminates background coincidentals (see the Section on event selection: 6.2.2).

The distribution of hits in the calorimeter with cuts on particular mirrors are shown in figure 5.21. The binned events are one cluster BETA2 triggers with energy higher than higher than 1.3 GeV with correlational cuts on the mirror number and cluster location. Because of the mirror design, correlating the mirror signal and bigcal location ensures that the event was an electron or positron that came from the target.

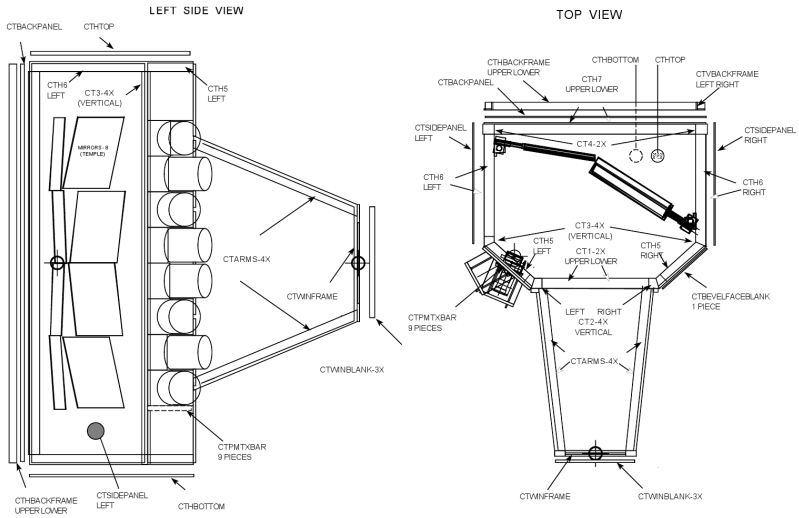

Figure 5.20: Temple University fabrication diagram of the cerenkov detector.

Particle	E_c
$e^{\pm}$	21.64MeV
$\pi^{\pm}$	5.91GeV
$p^{\pm}$	39.7GeV

Table 5.2: Table of critical energies for Cerenkov emission in the detector tank (N_2 at 1 atm).

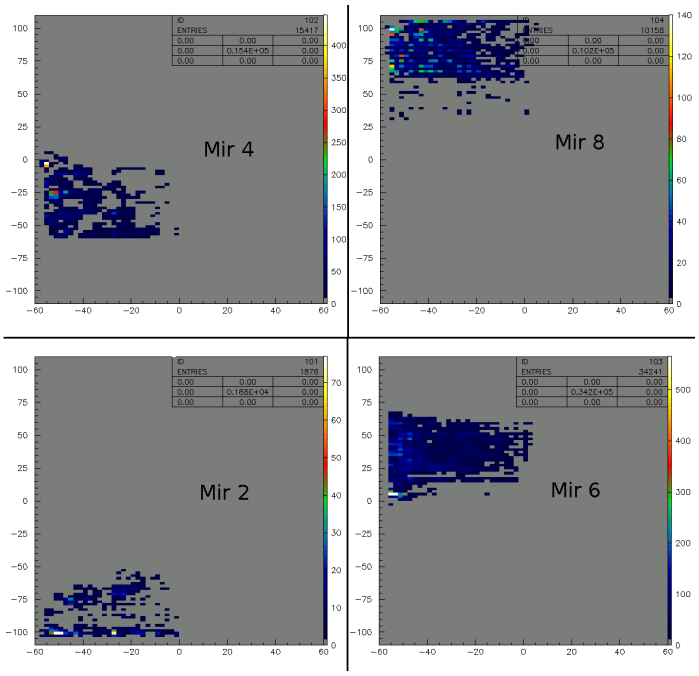

Figure 5.21: Events binned by Big Cal cluster location with different cuts on activated cerenkov PMT. The mirrors selected here are the even numbered ones which are the mirrors closest to the beam (smaller scattering angles).

5.7 BigCal

The calorimeter, nicknamed BigCal, is a segmented lead glass calorimeter ten radiation lengths deep capable of absorbing all of the energy of an incident electron and determining its hit location based on the energy distribution among its segments. The face of BigCal was positioned 335 cm from the target for a coverage of 235 msr. It was composed of 1722 lead glass blocks in two section. The bottom part is a 32×32 array of $38 \times 38 \times 450\text{mm}^3$ blocks. The top part is a 30×24 array of $40 \times 40 \times 400\text{mm}^3$ blocks. The electron radiation length in lead glass is 2.74cm, meaning the calorimeter will absorb 100% of the electrons energy while *bremsstrahlung* is the dominant energy loss mechanism–which is down to about 15MeV. Each block was wrapped in a light tight sheath (aluminized mylar), and coupled in the back to a photomultiplier tube. There was an aluminum absorber in front of the blocks to prevent low energy photon impingement, reducing background rates. When a high energy electron hits the calorimeter, it causes an electromagnetic shower within the block. The electron scatters at small angles within the glass, emitting *bremsstrahlung* radiation. These photons pair convert, and Cerenkov radiation is emitted by the resulting positrons and electrons. These electron and positrons in turn scatter, creating more photons and more e^+e^- pairs. The amount of Cerenkov light emitted by the shower is proportional to the amount of energy deposited in the lead glass [45]. The photomultiplier tube coupled to the rear of each block collects this light, and the signal from it is used to determine the energy deposited in that block.

One half of the analysis' primary trigger, BETA2 (see section 5.4), was a composite signal from BigCal. The signal from each PMT was sent to a bank of ADCs. Sums of ADC signals from eight rows of eight contiguous blocks are added to form sums of 64 blocks. These sum of 64 signals are discriminated and the discriminated signal split: one logic signal branch was used for triggering; the other is sent to a TDC for timing measurement. The DAQ and wiring for BigCal was identical to that in GEP-III, and

a complete description of the electronics and hardware associated with BigCal can be found in its documentation [46] or A. Puckett's thesis [47].

The *Moliere* radius (within which 90% of the particles energy is deposited) of lead glass is 4.7 cm, so a shower from an electron will span several calorimeter blocks. Event data from the calorimeter consists an ADC signal from each block and hit times associated with the groups of 64 blocks in which the hit was registered. To make sense of this data, several tasks must be completed:

(a) clustering

(b) position reconstruction

(c) energy reconstruction

(d) scattering angle determination.

5.7.1 Clustering

Clustering refers to the grouping of signals from individual blocks. For an event, each cluster should include only signals caused by the energy deposited by a single particle. This means differentiating nearby electron hits and avoiding including low energy background, while not excluding signals associated with a DIS electron.

Clustering is performed by software on an event by event basis after the run data file has been generated. A list of block indices with corresponding ADC values is given for each event. All blocks with less than 10 MeV deposited are rejected in order eliminate background events and noise from pedestals. The block ADC signals are ranked in descending order of the energy deposited for that event. The top of the list is taken as the center of the first cluster (that would be the block with a 1.2 GeV signal in the middle of the blue region of Fig. 5.22). All blocks in the list within a 5×5 grid centered on the first block are added to the first cluster and removed from the list. If there are still blocks in the list, the top one in the truncated list is assigned

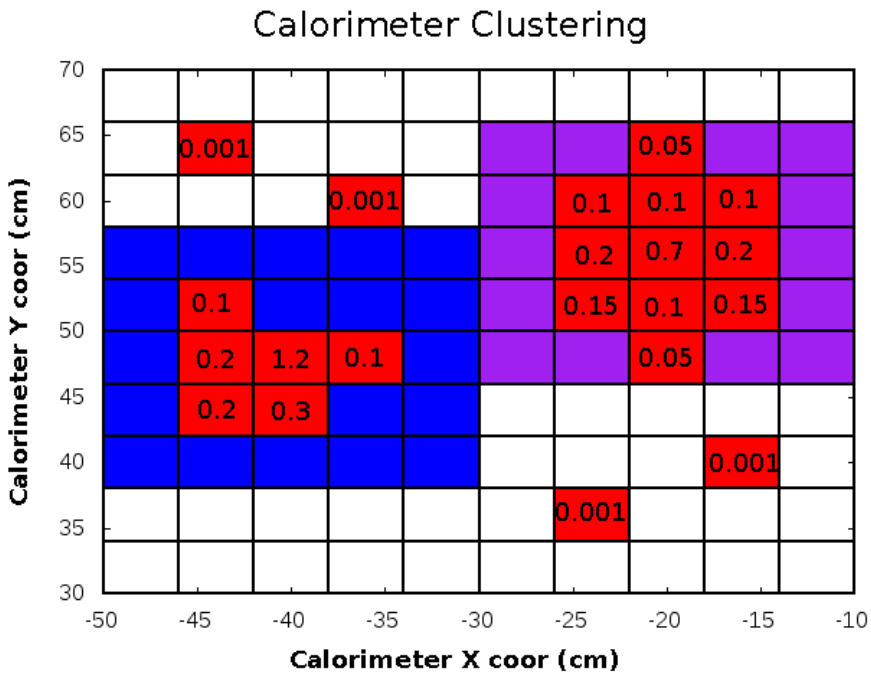

Figure 5.22: Cluster selections for a manufactured event. Red squares are blocks with energy deposits written in GeV. Blue is the region within which blocks are categorized in cluster 1. Purple is the region within which blocks are categorized in cluster 2.

to be the the starting block for the second cluster. Once again, all blocks within a 5×5 grid centered on the top block in the list are added to the second cluster (purple region in figure 5.22). This process is repeated until there are no blocks above the threshold set for starting a cluster (100 MeV). All data not included in a cluster is discarded as background.

Since the Moliere radius for an electron(positron) shower is 4.7cm, the entirety of a shower will fall well within the clustering routine's 5×5 grid. It is possible for two showers to occur within one trigger and for those showers to overlap. In that case, the first cluster may include signals from the lower energy particle shower. The cluster routine does not allow overlapping 5×5 grids, and the first cluster takes priority, so the second cluster's energy will be underestimated and the first, overestimated. For this analysis, only single cluster events are used, so such overlap is of no consequence. For analyses that include two cluster events, a cut will exclude events with less than

four block widths separating the cluster centers, thus avoiding the events with possible overlapping clusters.

There are other more complicated cluster routines, using cellular growth models or nearest-neighbor procedures, but they are useful only when categorizing clusters created from different particles or when accurate separation of nearby clusters is necessary [48]. In SANE, the Cerenkov half of the trigger is already cutting protons and mesons out of the data, and multi-cluster events only account for about 10% of the data. Later analysis can increase statistics slightly by sorting through the multi-cluster events for usable data. And the calorimeter segmentation is fine enough that nearby clusters are rare, so a more complicated routine is unnecessary.

5.7.2 Position Reconstruction

For the purpose of analysis, BigCal is assigned its own coordinate system. Unless otherwise noted, if the variables x or y are used, the coordinate system being referred to is BigCal's. When events are described in the lab frame, Cartesian coordinates are eschewed, and instead scattering angles and energies are used. In the case that the symbols x or y are used to describe something in the lab frame, the coordinate system to which they refer is stated explicitly.

BigCal's coordinate frame has the xy plane coplanar with the front face of the calorimeter. The origin is in the geometrical center of the calorimeter face, with the positive y axis pointing up, and the positive x axis being horizontal and pointing away from the beam. Position reconstruction is executed in BigCal's coordinate frame.

The electrons impinging on BigCal strike the face with an angle of incidence close to perpendicular. For these electrons the majority of its energy is deposited in the first block it strikes. Since the block the electron struck is easily identifiable, the problem in determining the hit location of a particle on the face of the calorimeter is, "How far off from the center of the block of maximum energy deposition did the

particle strike?" A neural network was set up and trained to accurately calculate the answer to that question using the the cluster data. Without the target field, the point of incidence is a function of the cluster's energy-weighted horizontal and vertical moment and the location of the cluster on the calorimeter's face. With the target field on, the problem gains momentum dependence and an additional scattering angle dependence due to the field and its spatial variation.

The complexity of the problem lent itself to a solution via a neural network. The basics of neural networks will be described here along with the composition of the one used to correct the hit position for clusters.

A neural network is a complicated function with inputs chosen based on what the desired output is expected to depend on. During the training process, function parameters are adjusted to minimize a user-defined error function. A linear fit to data can be viewed as a simple neural network. Performing a linear fit can be thought of as training a neural network with one input node (the abscissa), one bias node (the y-axis intercept), and an output node (the ordinate). A graphic depicting this network can be seen in Fig. (5.23). In a linear fit, one is trying to estimate a linear trend in a set of data points, $\{x_i^t, y_i^t\}$. An error function can be written down: $\mathrm{Err} = \sum_i (y_i^t - y(x_i))^2$, and one looks for a set of parameters, w_{12} and w_{02}, that minimizes Err for the function $y(x) = w_{12}x + w_{02}$. One then procedes iteratively, choosing for each iteration a set of parameters shifted from their previous value in such a way as to reduce Err.

The general construction and training of a neural network proceeds through similar steps. A neural network method is usually chosen to reproduce behavior exhibited in a data set when the dependencies of the data set on the inputs are expected but not well understood. For example, one may have set of stock prices that vary over time. Assume one has good reason to expect them to depend on housing prices, currency exchange rates, and market indexes, but one does not know what form that dependence might take. A neural network does not need a presumed functional

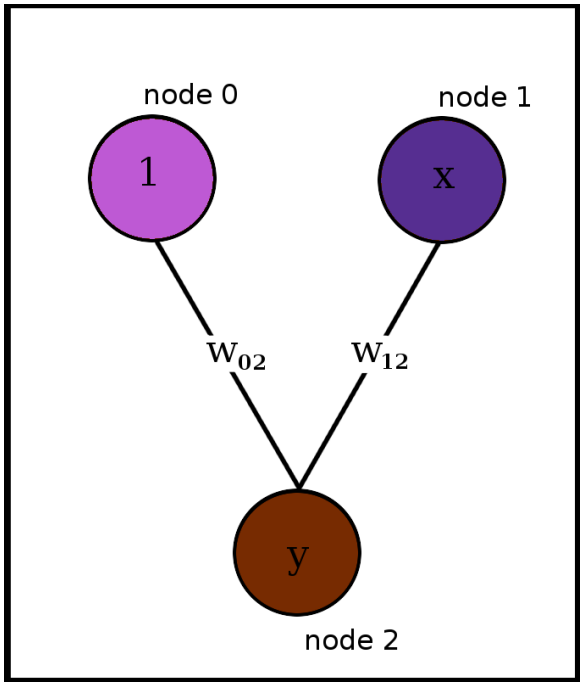

Figure 5.23: A graph of a simple neural network. It consists of one bias node, one input node, and one output node. The output of the network is $y = w_{12}x + w_{02}$.

form for the dependence of output (stock prices over time) on the inputs (indexes, exchanges etc.), which is what makes it a valuable numerical method for complicated problems.

To proceed in constructing a network (refer to Fig. 5.24 for the graphic layout), first a set of inputs are chosen, represented by a series of nodes at the top of the graph. The set of inputs includes a bias node, which is left implicit. Second, some number of "hidden" nodes are placed in a layer between the input and output layer. These nodes represent sigmoidal activation functions. A line with a corresponding weight is drawn from each input node to each of the hidden nodes. These lines indicate a value sent from the preceding layer, weighted by the coefficient, w_{ij}, associated with the line. If there are multiple lines coming from the preceding layer, the values from each connected node are summed. The hidden node then takes the weighted sum from the previous layer's connnected nodes and applies its activation function. A common activation function is hyperbolic tangent, and therefore the value sent to the

next layer from a hidden node is the hyperbolic tangent of the weighted sum of the node's inputs. The hidden nodes effectively act as switches, controlling which inputs are being combined with which and how they are applied to the output.

Any number of hidden layers may be inserted with any number of hidden nodes. Once this step is finished, an output layer is added. The output is composed of only as many nodes as needed to represent the data one is attempting to predict. Once again, weighted lines from each preceding node is drawn to each of the output nodes. Fig. (5.24) gives a general neural network and an example three layer network as an example to illustrate the input and output rules. In Fig. 5.24 the outputs would be

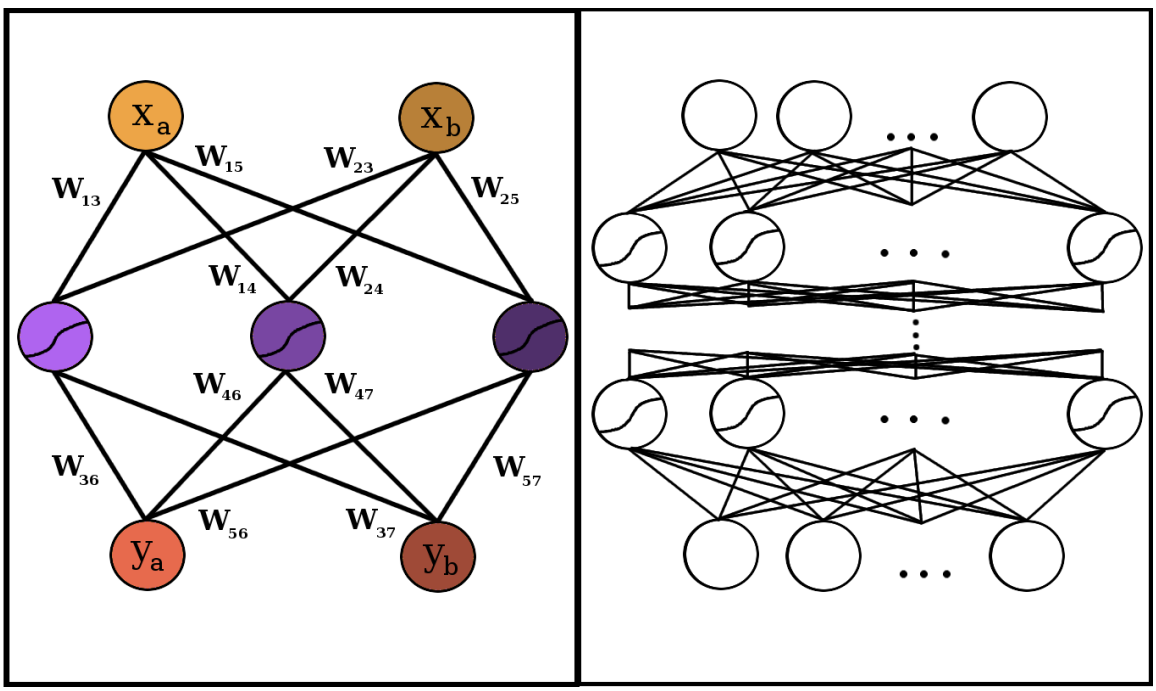

Figure 5.24: Left: An example network composed of an input layer with two nodes, x_a and x_b, a hidden layer with three nodes, and an output layer with two nodes, y_a and y_b. Right: A general neural network graph. It can be composed of one input layer with any number of inputs, any number of hidden layers with any number of hidden nodes on each layer, and one output layer with any number of outputs. In both cases a bias node exists and is implicit.

given by

$$y_a = \sum_{i=3}^{5} w_{i6} \tanh\left(w_{1i}x_a + w_{2i}x_b + w_{0i}\right) \tag{5.8}$$

where w_{0i} is the bias node weight and y_b is given by a similar equation with $w_{i6} \rightarrow w_{i7}$.

The w_{ij}'s are shifted iteratively to minimize the error function using a back propagation algorithm. It is beyond the scope of the thesis to describe the algorithm in a detailed manner. A more complete treatment of the subject of neural networks can be found in a book by R. Rojas [49].

The neural network trained to process the BigCal data and return the particle hit location relative to the center of the block of maximum energy deposition used 27 input nodes: the calorimeter coordinate of the center of the block of maximum energy deposition, and the energy deposited in the 25 blocks in a square grid centered on that point. Three output nodes are returned by the network: a shift in the horizontal and vertical position of the hit, and a shift in the energy of the cluster. The shift in energy is the estimated light lost– that is, the light not picked up by the calorimeter PMTs.

The network was trained using data generated in the SANE GEANT3 monte carlo simulation. Once the network was sufficiently trained, it was ported as a FORTRAN routine to the analysis code. The network architecture is shown in Fig. 5.25.

An estimate of the position resolution using the network was obtained in the simulation the network was trained on. The difference in the actual particle hit coordinate and the position predicted by the trained network is shown in Fig. 5.26. The work on the neural network was done by H. Baghdasaryan, and it gives a resolution of $\pm$1cm for the particle hit position on the calorimeter.

5.7.3 Energy Calibration

The signal from a PMT in the calorimeter is proportional to the amount of energy deposited by the particle in that block. Initial gain matching using cosmic events adjusted the high voltage on the PMTs, so that each ADC channel roughly corresponded to about 1 MeV– that is, a hit in a block that registered in ADC channel

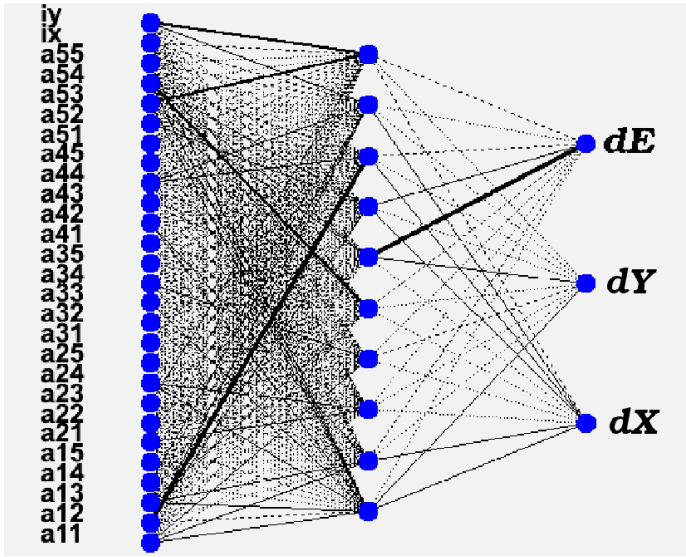

Figure 5.25: SANE neural network for calculating electron point of incidence and energy correction. It is composed of twenty seven input nodes, ten nodes in a single hidden layer, and three outputs. Boldness of lines indicates the magnitude of the weight between nodes. Diagram from Ref. [50]

1000 corresponds to about 1 GeV being deposited in that block. The precise factor that relates the ADC value to the energy deposited in the block must be calculated using well understood events. Elastic electron proton scattering can be detected in coincidence measurements using the HMS to detect protons and BigCal to detect electrons. Since the HMS is well understood, the energy of electron events in BigCal from $ep \rightarrow ep$ scattering could have been calculated using the HMS data. The gain constants for BigCal's PMTs could have been then adjusted accordingly. The elastic calibration run plan was interrupted by hardware trouble. Target magnet malfunctions delayed operations long enough that there was no time to complete an eleastic calibration. SANE was forced to look elsewhere for a calibration method.

Neutral pion decay is another process that is well understood, and, once identified in the data, provides information about the energy of the showers in BigCal. Using meson decays to calibrate detectors has been done before [51].

Neutral pions decay 98.8% of the time through $\pi \rightarrow 2\gamma$ [2]. This decay can be detected by the single arm of BETA detector. Pion production occurs in the target,

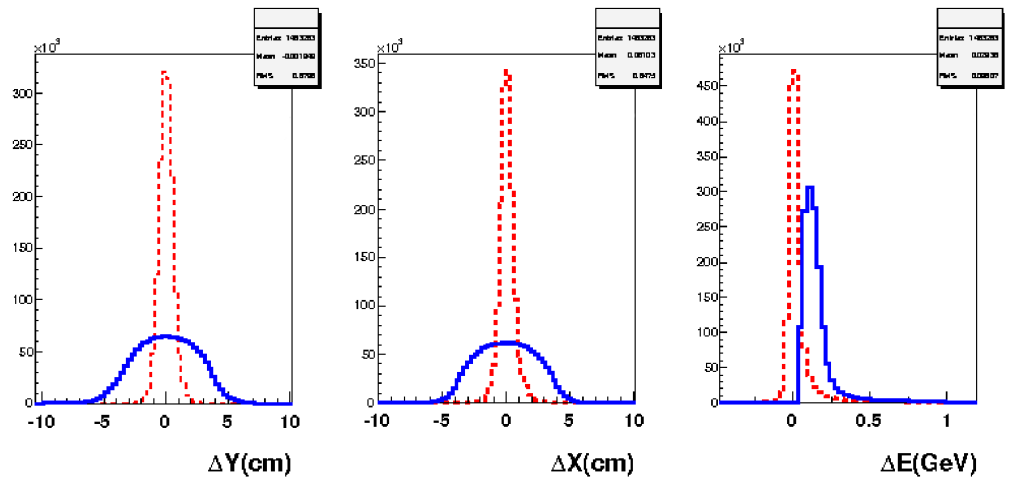

Figure 5.26: $\Delta\xi$, where ξ is some experimental quantity, is the difference between the reconstructed value for ξ and the simulation's actual value for ξ. The histograms from left to right are the difference in the vertical position coordinate, the horizontal position coordinate, and the particle energy. The blue histograms are obtained without the neural network, using the central coordinate value of the block of maximum deposition. The red histograms are obtained with the fully trained neural network. Plots from reference [50].

and since the π^0 has a very short lifetime ($8 \times 10^{-17}s$), the decay occurs while the pion is still in the target cup. The resulting photon pair leaves the target, separated by some angle θ_π, and deposits energy in the calorimeter in two distinct clusters without triggering the Cerenkov. Consequently, these events are easily identifiable as two cluster events without a Cerenkov trigger (BETA1 2 clusters or PION trigger). Once a two cluster event has been identified, the angle between the two clusters can be computed. The calorimeter gives an uncalibrated reconstructed energy for the two clusters of E_1 and E_2. The invariant mass of the decay products should be equal to the mass of the neutral pion, 135 MeV. One can calculate this:

$$m_{inv} = \sqrt{2E_1E_2(1 - \cos\theta_\pi)}. \tag{5.9}$$

Calculating this for all pion events will produce a m_{inv} distribution. Due to the initial approximate calibration of the calorimeter, the peak of the distribution will

be broad and in the region of m_π. In order to achieve a calibration, an iterative adjustment of gains was used that attempts an asymptotic approach to an ideal distribution of m_{inv}. First, a sample of events that are assumed to be due to neutral pion decays are selected from similar runs. For the beam energy SANE uses, we expect the most probable separation angle for the pion decay products to give a separation of 20 cm to 80 cm at Big Cal, and so a cut is placed to limit the minimum distance between clusters. A cut is also placed on cluster energy in order to reduce low energy background. With a set of events that are tentatively labeled as pion events, a block in BigCal is chosen for calibration. All events containing a cluster that includes the chosen block and for which at least 80% of the energy for that cluster is contained in the chosen block are selected. A distribution of m_{inv} is created from the selected events. Fitting the peak of that distribution gives some centroid m'_{π^0}. The difference between the actual π^0 mass and m'_{π^0} gives some measure of the how far off the gain of that block's PMT is. A calibration constant is then assigned to that block with the value

$$C_i = \left(\frac{m_{\pi^0}}{m'_{\pi^0}}\right) C'_i, \tag{5.10}$$

where C'_i is the previous calibration constant. This process is repeated for each block, establishing an initial set of calibration constants. Once a full set of C_i's is found, the procedure is repeated, using the new calibration constants to calculate the energy in a block i in MeV from it's ADC value, A_i, as

$$E_i = C_i A_i. \tag{5.11}$$

A single iteration will not give the correct calibration. $C_i A_i$ will not be exactly the energy deposited because C_i was calculated using the uncalibrated signals from the surrounding blocks. Multiple iterations are required to bootstrap all the calibration constants up toward their ideal value.

5.7.4 Energy Resolution

The energy resolution of the calorimeter is determined by examination of neutral pion decays following a work by R.T. Jones *et al* [51]. The energy spectra of neutral pion decays are examined and used to calculate the energy dependent resolution of the calorimeter. The overall energy resolution will first be determined. Then a brief look into how that resolution varies across the face of the calorimeter will follow.

If one could select calorimeter clusters of known energy, binning the difference of the true energy and the energy as measured by the calorimeter would give a spectrum, the width of which is the average energy resolution of BigCal. Further narrowing those events to be within a small absolute energy range would give one the calorimeter resolution within that energy range. As mentioned previously, SANE was not able to avail itself of a source of scattered particles of known energy.

In order to estimate the energy resolution, one needs to have some preexisting knowledge of the energy of the particles in a subset of detector events. One does not know anything about the energy of the individual photon energies from a neutral pion decay, but one does know of a functional relationship between the two energies and the opening angle between the two photons. That relationship is that the invariant mass of the two particle system should be the rest mass of the pion or $m_{\pi^0} = \sqrt{2E_1E_2(1-\cos\theta)}$, where $E_{1,2}$ are the energies of the photons.

Supposing a set of pion decay events, pick an energy and energy range E_1 and ϵ_1, and cut all pion decay events that don't have a photon cluster within $(E_1-\epsilon_1, E_1+\epsilon_1)$. Next, choose an energy E_2 for the second photon from the decay, but do not cut on the second cluster energy. The relationship between the separation angle, the cluster energies, and the pion mass is used to calculate the expected angle of separation for pion decay products with energies E_1 and E_2:

$$\alpha(E_1, E_2) = \cos^{-1}\left(\frac{1 - m_{\pi^0}^2}{2E_1E_2}\right). \tag{5.12}$$

Cutting on the angle between the clusters to within the range $(\alpha - \delta\alpha, \alpha + \delta\alpha)$ leaves a subset of pion decay events, and the energy spectrum of the second cluster contains a peak around the chosen energy, E_2. The width of that peak is the quadratic sum of the energy resolutions at E_1 and E_2 for the calorimeter. Fitting the peak with a Gaussian curve, one gets $\sigma = \sqrt{(\delta E_1)^2 + (\delta E_2)^2}$. By looking at symmetric pion decays in which $E_1 = E_2$, the resolution, at energies where enough symmetric decay statistics exist, can be calculated. Asymmetrical decays are more common, and once one has a set of resolutions calculated using symmetric decays, one can extend the analysis to other energies, provided decays are examined in which either E_1 or E_2 are known.

A separate resolution calculation was performed for each of the experimental settings (see Table 6.1). This was done because of concerns about how the re-oriented field might affect the calorimeter PMTs. The target field significantly changes the gain on the calorimeter PMTs, and therefore there was a separate energy calibration performed at each setting, necessitating a new resolution calculation.

5.7.5 Resolution Calculation Results

A sample of events was selected for the resolution calculation. All two cluster events with both cluster coordinates satisfying $-54\text{cm} < x < 54\text{cm}$ and $-106\text{cm} < y < 106\text{cm}$ and with cluster energies each greater than 500MeV made it through the first cut. Using the separation angle between the clusters for each event to calculate the invariant mass of the two particle system yields a clear peak at the pion mass on top of a broad background. This spectrum for the 80° field and 5.9GeV beam energy runs is shown in figure 5.27

In order to clean the background out of the sample, a cut was placed on the pion energy$(E_1 + E_2)$ versus separation angle distribution. The cut is shown in Fig. (5.28), and was determined by looking at the most probable separation angles at different

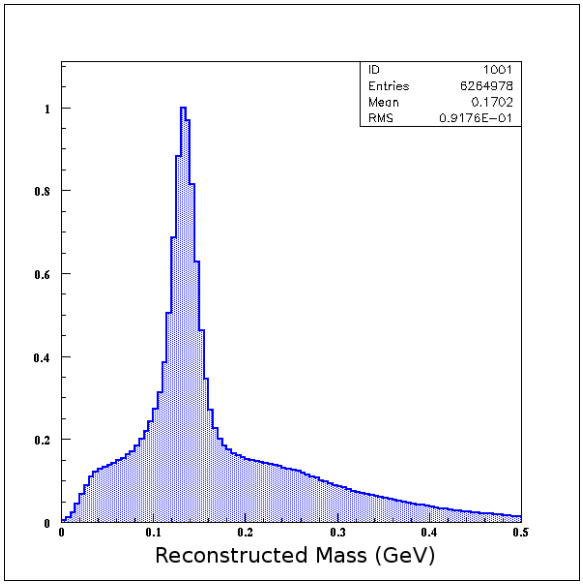

Figure 5.27: Invariant mass spectrum of 2 cluster events after initial event selection. The events are taken from good ammonia and carbon runs from 72417 to 72795. Total number of events is indicated in the legend. The histogram has been normalized so that the maximum of the peak is equal to one.

pion energies. The most probable separation angle versus energy was calculated from 0.2 GeV to 2.5 GeV, and fit with a curve of the form $a/(E^2+b)+c$. The distribution in Fig. 5.28 follows that curve. Events between the curves

$$\theta_{\text{hi}} = \frac{16.54}{E_{\pi^0}^2 + 0.36} + 6.52 \text{ and } \theta_{\text{lo}} = \frac{11.97}{E_{\pi^0}^2 + 0.22} + 3.33 \tag{5.13}$$

were used; θ_{hi} and θ_{lo} are the bounds on the separation angles at pion energy E. The upper and lower bounds were chosen by fitting points offset from the most probable separation curve in energy by an amount determined by the width of the of the peak in a slice in theta of the distribution shown in the left of Fig. 5.28.

The mass spectrum shown in Fig. 5.29 is the final set of events used in the energy resolution calculation. The spectrum for each experiment configuration are shown before and after the cuts, and a fit is given for the pion mass peak plus background.

Using the method described in the previous sections, the intial energy cut on the first cluster was within 8% of the E_1. The separation angle between the two clusters

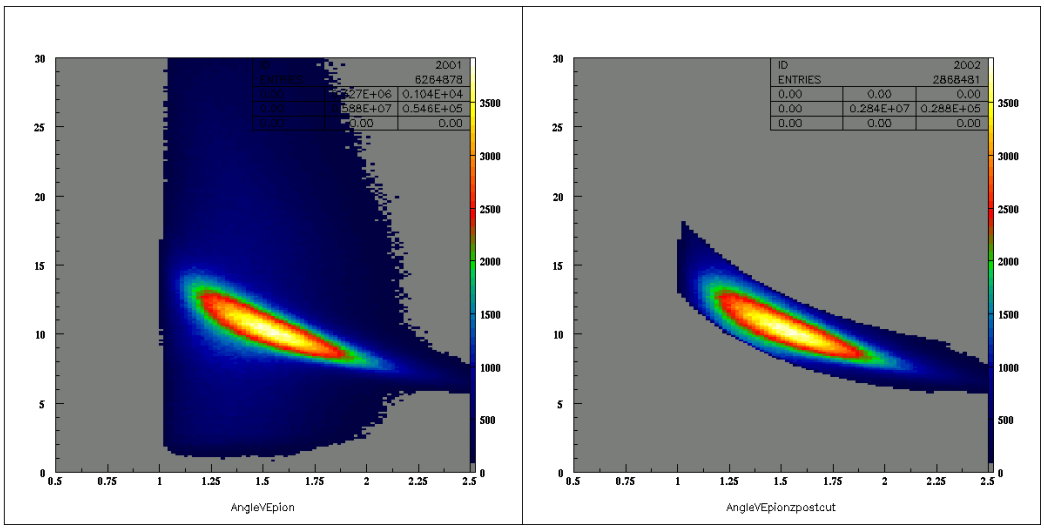

Figure 5.28: The pion decay product separation angle vs the parent pion energy. Left: Distribution for all events from the same set as figure 5.27 Right: The events selected by the cut between the curves in Eq. 5.13.

was required to be less than 4% away from the angle indicated by the chosen energy E_2 (Eq. 5.12). The spectrum of E_2 was fit with a gaussian curve on top of a wide and offset background gaussian. An example of the fit can be seen in Fig. 5.30. Symmetric decays with $E_1 = E_2$ were examined, and the resolution at E_1 was given by $\sigma/\sqrt{2}$ of the fit to the E_2 spectrum peak. The error in the resolution calculation was taken to be the error in the fit parameter σ. Asymmetric pion decays in which the resolution at E_1 is known from the symmetric decay sample, were examined and the resolution at E_2 is given by $\delta E_2 = \sqrt{\sigma^2 - \delta {E_1}^2}$. The resolution at a given energy can be calculated using different combinations of E_1 and E_2, and the final resolution estimate is taken to be the error weighted average of all calculations done for a single energy. Plots of the calorimeter energy resolution as a function of cluster energy are shown for each experimental configuration in figure 5.32. The table below (Table 5.3) shows the fits to the plots in figure 5.32, which are expected to be of the form $A/\sqrt{E}$, where A is the % is the resolution of the calorimeter at energy E [45]. The calibration at all experimental settings yielded about a $10\%/\sqrt{E}$ resolution. Scattered energies of less than 1.3GeV were not used in the analysis. The energy resolution for a cluster

at 1.5GeV is 8.25% or 124MeV.

Target Orientation	Beam Energy	% Res
80°	5.9GeV	$(9.62 \pm 0.36)/\sqrt{E(\text{GeV}))}$
80°	4.7GeV	$(10.89 \pm 1.27)/\sqrt{E(\text{GeV})}$
180°	5.9GeV	$(9.72 \pm 0.25)/\sqrt{E(\text{GeV})}$
180°	4.7GeV	$(10.19 \pm 1.33)/\sqrt{E(\text{GeV})}$

Table 5.3: Percent Energy Resolution for each Experimental Setting.

5.7.6 Tracking through the field

The electrons scattering from the target experience a Lorentz force due to the target field, bending their path. This complicates the assignment of scattering angles to hits in BigCal. Given a hit position on BigCal, the apparent angle (angle determined by the ray traced from the cluster position to the target: see Fig. 5.19) differs from the scattering angle by an amount that depends on the momentum of the particle and the particle's path through the non-uniform fringe target field. The magnet field has been mapped and extrapolated out to 100cm. Beyond 20cm, the field is weak enough that the scattered electrons above 0.5GeV experience no observable bending, so the coverage of the extended field map is more than enough to calculate the path of a particle through the field, given its charge and initial momentum vector.

The change in angle can be calculated using

$$\Delta\theta \approx \frac{e}{p} \int dlB, \tag{5.14}$$

where p is the particle's momentum, B is the field strength perpendicular to the particle's path, and dl is the infinitesimal line length along the particle path.

Calculating the particles path numerically on an event by event basis in order to determine the the initial scattering angle costs too much processing time to implement at that level of the analysis. The SANE GEANT3 monte carlo simulation contains

the field map and a routine for tracking through the field, so it can be used to generate a set of data on which a fit can be performed to use in predicting scattering angles given BETA data. A set of electron tracks were collected and a fit performed to the monte carlo data using the function

$$\begin{aligned}\theta = \theta_r \quad &+ \quad (a_1 + a_2\theta_r + a_3\phi_r + a_4\theta_r^2 + a_5\phi_r^2 + a_6\theta_r\phi_r) \\ &\times \quad (a_7 + a_8\tfrac{1}{E_r} + a_9\tfrac{1}{E_r^2}) \\ &\times \quad (a_{10} + a_{11}sr_x + a_{12}sr_x^2) \\ &\times \quad (a_{13} + a_{14}sr_y + a_{15}sr_y^2).\end{aligned} \tag{5.15}$$

The result is used in the analysis code to correct the scattering angle θ based on the reconstructed variables: where θ_r and ϕ_r are the angles of a ray traced from BigCal's cluster to the target in the lab frame, (sr_x, sr_y) are the slow raster positions, and the reconstructed particle energy is E_r. The parameters a_i were adjusted to minimize the error on the predicted scattering angle θ (or ϕ) when compared to that recorded by the simulation. A similar fit for ϕ was performed using

$$\begin{aligned}\phi = \phi_r \quad &+ \quad (b_1 + b_2\theta_r + b_3\phi_r + b_4\theta_r^2 + b_5\phi_r^2 + b_6\theta_r\phi_r) \\ &\times \quad (b_7 + b_8\tfrac{1}{E_r} + b_9\tfrac{1}{E_r^2}) \\ &\times \quad (b_{10} + b_{11}sr_x + b_{12}sr_x^2) \\ &\times \quad (b_{13} + b_{14}sr_y + b_{15}sr_y^2).\end{aligned} \tag{5.16}$$

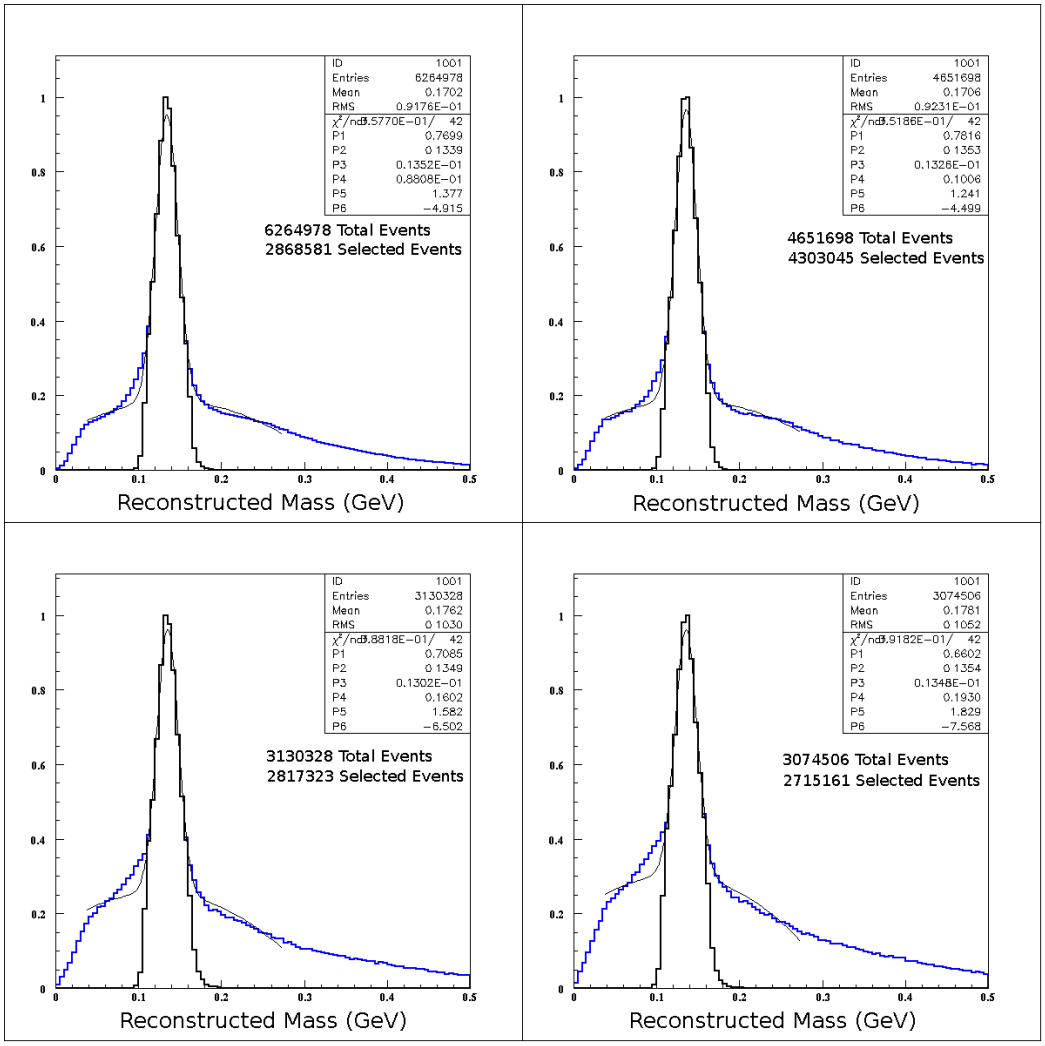

Figure 5.29: Overlay of the selected events (black) over all two cluster events (blue). A fit is also shown here to the mass peak and the adjascent background. The fit is $P_1 \exp\left(-\frac{(x-P_2)^2}{2{P_3}^2}\right) + P_4 + P_5 x^2 + P_6 x^3$ Top Left: 5.9GeV and 80°. Top Right: 4.7GeV and 80°. Bottom Left: 5.9GeV and 180°. Bottom Right: 4.7GeV and 180°.

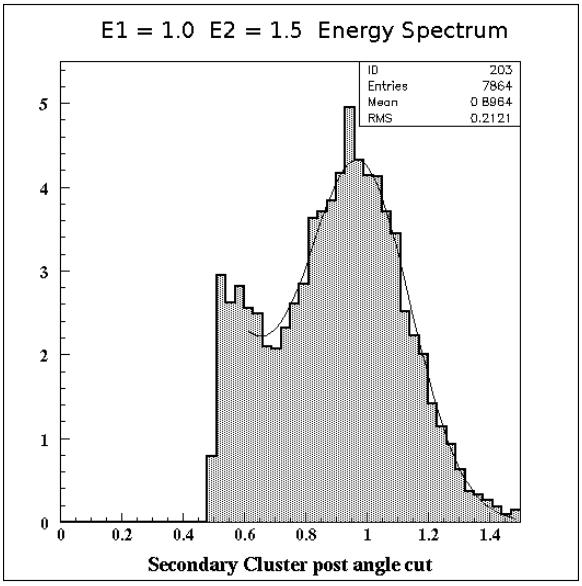

Figure 5.30: Energy spectrum of the second cluster after appropriate energy and angle cuts. The fit is the sum of two gaussians curves. The chosen cluster energies were $E_1 = 1.5$ and $E_2 = 1.0$. The already determined resolution at 1.0GeV, and the width of the peak can be used to calculate the resolution at 1.5GeV.

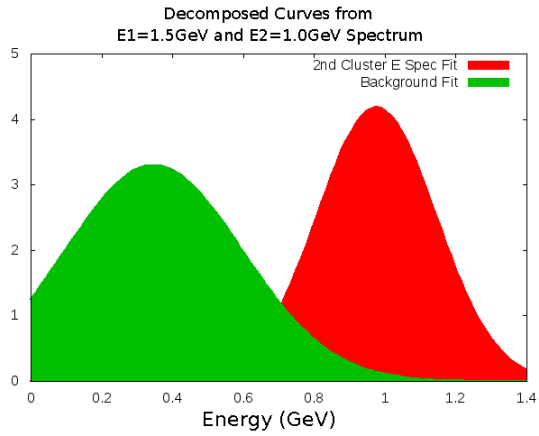

Figure 5.31: Two curves, the sum of which were used to fit the spectrum in figure 5.30. The width of the curve fit to the 2nd cluster spectrum is needed for the resolution calculation. Fits: 2nd clust peak $= 4.2\exp(-\frac{(E-0.98)^2}{2(0.17)^2})$, Background $= 3.3\exp(-\frac{(E-0.35)^2}{2(0.25)^2})$.

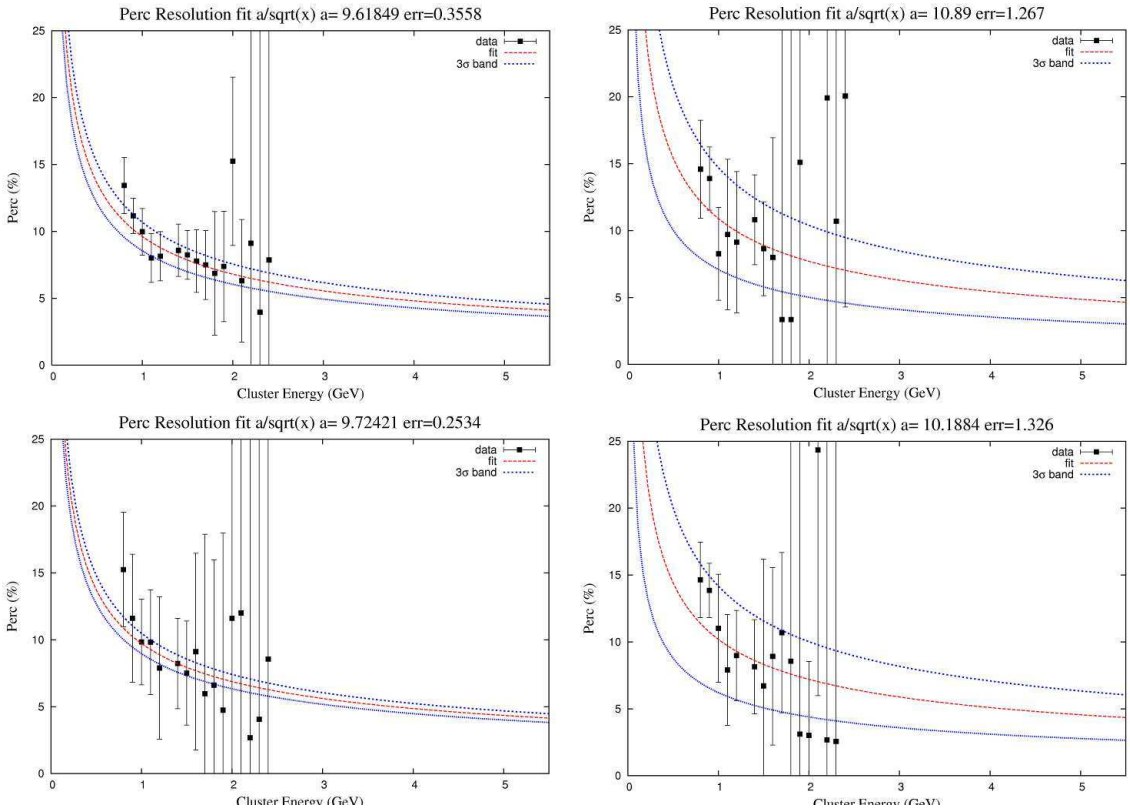

Figure 5.32: Energy resolution curves for each configuration Top Left: 5.9 GeV and 80°. Top Right: 4.7 GeV and 80°. Bottom Left : 5.9 GeV and 180°. Bottom Right : 4.7 GeV and 180°.

Chapter 6

Asymmetry Analysis: A_1^p

6.1 Calculation of A_1 from Asymmetries

The following is the calculation of A_1 in terms of the measured double spin asymmetries, starting from the cross section difference for opposite proton or beam spins. This calculation is for an inclusive process. That process is represented by Fig. 6.1, on which is labeled the incoming momenta, k and P, the outgoing momentum, k', and the spins for each state. The final state of the proton is undetected. Capital variables refer to the nucleon (proton in our case) and lower case to the electron. Primes denote variables for outgoing particles.

The calculation's starting point is the cross section difference for the same process but with opposite initial beam helicities. The sum is over outgoing electron spin states, since the detector makes no distinction. The cross section difference is

$$\Delta\sigma = \sum_{s'} \left[\frac{d^2\sigma}{d\Omega dE'}(k, s, P, S; k', s') - \frac{d^2\sigma}{d\Omega dE'}(k, s, P, -S; k', s') \right]. \tag{6.1}$$

Since these are polarized cross sections, the difference will be expressible in terms of the kinematic variables and the polarized structure functions $G_1(x, Q^2)$ and $G_2(x, Q^2)$ (refer to Eq. 2.18). Expanding the sum, one gets

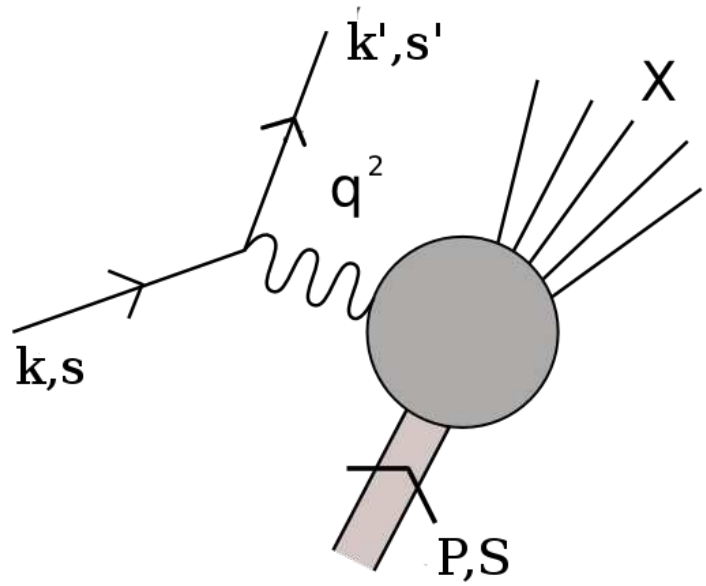

Figure 6.1: Diagram of inclusive scattering. Electron with 4 momentum k scatters from a nucleon. The detected scattered electron has momentum k' and the undetected final nucleon state is marked as X. The inital nucleon momentum is P. Spin 4-vectors are marked with s, s', and S.

$$\begin{aligned}\Delta\sigma &= \frac{8m\alpha^2 E'}{q^4 E}\left[(q\cdot S)(q\cdot s) + Q^2(s\cdot S)\right] MG_1 \\ &+ \frac{8m\alpha^2 {E'}^2}{Q}\left[(s\cdot S)(P\cdot q) - (q\cdot S)(P\cdot s)\right]\frac{G_2}{M}. \end{aligned} \tag{6.2}$$

The nucleon mass is written here as M. The 4-momentum transferred to the nucleon is q^μ, and the negative of its invariant square is Q^2. In the lab frame, using the coordinate frame from Fig. 6.2 and neglecting the mass of the electron, we can write the vectors from Eq. 6.2 as follows:

$$k^\mu = E(1,0,0,1) \text{ and } k'^\mu = (E', \vec{k'}) \text{ where}$$

$$\vec{k'} = E'(\cos\phi\sin\theta, \sin\phi\sin\theta, \cos\theta),$$

$$S^\mu = (0, \cos\beta\sin\alpha, \sin\beta, \sin\alpha, \cos\alpha),$$

$$s^\mu = \frac{E}{m}(1,0,0,1), \text{ and}$$

$$P^\mu = (M,0,0,0).$$

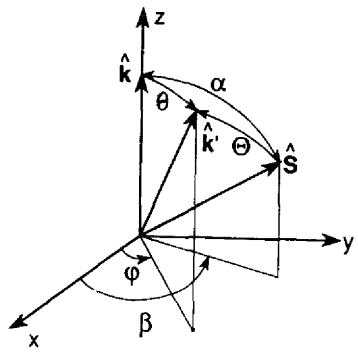

Figure 6.2: z is in the beam direction. x points to the left of the beam, which is toward Big Cal. y is up in the lab.

The necessary products for completing the calculation are:

$$q^\mu = k^\mu - k'^\mu,$$

$$k \cdot S = -E\cos\alpha,$$

$$k' \cdot S = -E'\cos\Theta,$$

$$q \cdot S = E'\cos\Theta - E\cos\alpha,$$

$$k \cdot s = \frac{E^2}{m},$$

$$q \cdot s = \frac{EE'}{m}(1-\cos\theta),$$

$$s \cdot S = -\frac{E}{m}\cos\alpha,$$

$$P \cdot q = M(E-E'), \text{ and}$$

$$P \cdot s = \frac{M}{m}E.$$

Then one can write down the difference explicitly in terms of angles and momenta measured in the lab

$$\begin{aligned}\Delta\sigma &= \frac{8m\alpha^2E'}{q^4E}\left\{\left[(E'\cos\Theta - E\cos\alpha)(-\frac{EE'}{m}(1-\cos\theta)) + (-Q^2\frac{E}{m}\cos\alpha)\right]MG_1\right.\\ &\left. + Q^2\left[(-\frac{E}{m}\cos\alpha)M(E-E') - \frac{M}{m}E(E'\cos\Theta - E\cos\alpha)\right]\frac{G_2}{M}\right\}.\end{aligned} \tag{6.3}$$

Simplifying and collecting terms in $\cos\alpha$ and $\cos\Theta$, one gets

$$\Delta\sigma = \frac{-4\alpha^2E'}{Q^2E}[(E\cos\alpha + E'\cos\Theta)MG_1 + 2EE'(\cos\Theta - \cos\alpha)G_2]. \tag{6.4}$$

It is necessary to express Θ in terms of scattering angles. If one has an arbitrary set of two vectors, $\vec{A}$ and $\vec{B}$, which are expressible as

$$\vec{A} = |\vec{A}|(\sin\theta_A\cos\phi_A, \sin\theta_A\sin\phi_A, \cos\theta_A) \tag{6.5}$$

and

$$\vec{B} = |\vec{B}|(\sin\theta_B\cos\phi_B, \sin\theta_B\sin\phi_B, \cos\theta_B); \tag{6.6}$$

one can write the cosine of the angle between them as $\sin\theta_A\sin\theta_B\cos(\phi_A - \phi_B) + \cos\theta_A\cos\theta_B$. So $\cos\Theta$ is

$$\cos\Theta = \sin\theta\sin\alpha\cos(\phi - \beta) + \cos\theta\cos\alpha. \tag{6.7}$$

Now in case where the target spin is aligned with the beam direction

$$\hat{S} \parallel \hat{z} : \alpha = \beta = 0, \cos\Theta = \cos\theta, \cos\alpha = 1, \tag{6.8}$$

and the case where the target spin is aligned with the x axis, perpendicular to the

beam direction:

$$\hat{S} \parallel \hat{x} : \alpha = 90^\circ, \beta = 0, \cos\Theta = \sin\theta\cos\phi, \cos\alpha = 0. \tag{6.9}$$

The above configurations represented by equations 6.8 and 6.9 would result in the cross section differences $\Delta\sigma_\parallel$ and $\Delta\sigma_\perp$ respectively

$$\Delta\sigma_\parallel = \frac{-4\alpha^2 E'}{Q^2 E}[(E + E'\cos\theta)MG_1 - Q^2 G_2] \tag{6.10}$$

$$\Delta\sigma_\perp = \frac{-4\alpha^2 E'^2}{Q^2 E}\sin\theta\cos\phi(MG_1 + 2EG_2). \tag{6.11}$$

By doing a general calculation of the cross-section difference without specifying the angle of the target spin vector, but assuming it is in the xz plane one can calculate it to be a linear combination of the perpendicular and parallel cross section differences:

$$\Delta\sigma_\angle = \Delta\sigma_\parallel\cos\alpha + \Delta\sigma_\perp\sin\alpha. \tag{6.12}$$

Equation 6.12 allows one to take measurements of cross section difference at α angles different than 90° and still obtain $\Delta\sigma_\perp$. This fact was taken advantage of when planning SANE. Data was taken at 80° and the relation above will be used to calculate higher level quantities requiring $\Delta\sigma_\perp$.

6.1.1 Unpolarized Cross-Section

The form of the measured asymmetries of interest is

$$A = \frac{\frac{d^2\sigma^{\Uparrow\uparrow}}{d\Omega dE'} - \frac{d^2\sigma^{\Downarrow\uparrow}}{d\Omega dE'}}{\frac{d^2\sigma^{\Uparrow\uparrow}}{d\Omega dE'} + \frac{d^2\sigma^{\Downarrow\uparrow}}{d\Omega dE'}}, \tag{6.13}$$

where the arrows indicate that the spin of the target has been flipped. We have already an expression for the numerator, and the denominator is simply twice the unpolarized cross-section, $2\sigma^{\text{unp}}$. From Eq. 2.14, one has in terms of unpolarized structure functions, $W_1(M\nu, Q^2)$ and $W_2(M\nu, Q^2)$,

$$\frac{d^2\sigma^{\text{unp}}}{d\Omega dE'} = \frac{4\alpha^2 E'^2}{q^4}\left[2W_1 \sin^2\frac{\theta}{2} + W_2\cos^2\frac{\theta}{2}\right]. \tag{6.14}$$

One can express the ratio of W_2 to W_1 using another structure function R– the ratio of longitudinal to transverse cross sections,

$$\frac{W_2}{W_1} = \frac{1+R}{1+\frac{\nu^2}{Q^2}}. \tag{6.15}$$

Using this relation and factoring out a Q^2, one has

$$\frac{d^2\sigma^{\text{unp}}}{d\Omega dE'} = \frac{2\alpha^2 E'}{Q^2 E}W_1\left[1 + \frac{1+R}{2(1+\frac{\nu^2}{Q^2}\tan^2\frac{\theta}{2})}\right]. \tag{6.16}$$

This can be expressed more compactly by using the substitutions

$$\epsilon = \frac{1}{1+2(1+\frac{\nu^2}{Q^2})\tan^2\frac{\theta}{2}} \tag{6.17}$$

and

$$D' = \frac{1-\epsilon}{1+\epsilon R} \tag{6.18}$$

to get

$$\sigma^{\text{unp}} \equiv \frac{d^2\sigma^{\text{unp}}}{d\Omega dE'} = \frac{2\alpha^2 E'}{Q^2 E}\frac{W_1}{D'}, \tag{6.19}$$

and the asymmetries are

$$A_\angle = \frac{\Delta\sigma_\angle}{2\sigma^{\text{unp}}}, \tag{6.20}$$

where the target angle at which the asymmetry is calculated is left unspecified.

6.1.2 Asymmetries and Structure Functions

For SANE, one needs the asymmetries for the target polarization anti-parallel to the beam and for the target polarization to be aligned 10° off from the x-axis in the xz plane. Remember, this is a coordinate system in which the z-axis points along the beamline towards the beam dump, the y-axis points up, and the x-axis is horizontal pointing towards the Big Cal side of the beamline. The asymmetry associated with the near-perpendicular configuration is obtained from Eqs. 6.12 and 6.19

$$\begin{aligned} A_{80^\circ} &= \frac{-D'}{W_1}\{[(E+E'\cos\theta)\cos 80^\circ + E'\sin\theta\cos\phi\sin 80^\circ]MG_1 \\ &\quad +(2EE'\sin\theta\cos\phi\sin 80^\circ - Q^2\cos 80^\circ)G_2\}. \end{aligned} \tag{6.21}$$

The asymmetry associated with a target spin directed anti-parallel to the electron beam is $-\Delta\sigma_{\parallel}/2\sigma^{\mathrm{unp}}$, which using Eqs. 6.19 and 6.11 is

$$A_{\nparallel} = -\frac{D'}{W_1}[(E+E'\cos\theta)MG_1 - Q^2G_2]. \tag{6.22}$$

One can find linear combinations of $A_{\nparallel}$ and A_{80° that yield the structure functions. These are

$$\frac{MG_1}{W_1} = -\frac{A_{\nparallel}(Q^2\cos 80^\circ - 2EE'\sin\theta\cos\phi\sin 80^\circ) + Q^2A_{80^\circ}}{D'E'\sin\theta\cos\phi\sin 80^\circ[2E(E+E'\cos\theta)+Q^2]}, \text{ and} \tag{6.23}$$

$$\frac{G_2}{W_1} = -\frac{[(E+E'\cos\theta)\cos 80^\circ + E'\sin\theta\cos\phi\sin 80^\circ]A_{\nparallel} + (E+E'\cos\theta)A_{80^\circ}}{D'E'\sin\theta\cos\phi\sin 80^\circ[2E(E+E'\cos\theta)+Q^2]}. \tag{6.24}$$

The spin asymmetries are given by the following (see Ref. [52]):

$$A_1 = \nu\frac{MG_1}{W_1} - Q^2\frac{G_2}{W_1}, \text{ and} \tag{6.25}$$

$$A_2 = \sqrt{Q^2}\left(\frac{MG_1}{W_1} + \nu\frac{G_2}{W_1}\right). \tag{6.26}$$

Doing the substitution gives

$$A_1 = \frac{Q^2(E + E'\cos\theta - \nu)(\cos 80^\circ A_{\parallel} + A_{80^\circ}) + E'(2\nu E + Q^2)\sin\theta\cos\phi\sin 80^\circ A_{\parallel}}{D'E'\sin\theta\cos\phi\sin 80^\circ[2E(E + E'\cos\theta) + Q^2]} \tag{6.27}$$

and

$$A_2 = -\sqrt{Q^2}\frac{(\nu - 2E)E'\sin\theta\cos\phi\sin 80^\circ A_{\parallel} + [Q^2 + \nu(E + E'\cos\theta)](A_{80^\circ} + \cos 80^\circ A_{\parallel})}{D'E'\sin\theta\cos\phi\sin 80^\circ[2E(E + E'\cos\theta) + Q^2]} \tag{6.28}$$

The above expressions simplify greatly :

$$A_1 = \frac{1}{D'}\left(\frac{E - E'\cos\theta}{E + E'}A_{\parallel} + \frac{E'\sin\theta\cos 80^\circ}{(E + E')\cos\phi\sin 80^\circ}A_{\parallel} + \frac{E'\sin\theta}{(E + E')\cos\phi\sin 80^\circ}A_{80^\circ}\right) \tag{6.29}$$

and

$$A_2 = \frac{\sqrt{Q^2}}{2D'E}\left(A_{\parallel} - \frac{(E - E'\cos\theta)\cos 80^\circ}{E'\sin\theta\cos\phi\sin 80^\circ}A_{\parallel} - \frac{E - E'\cos\theta}{E'\sin\theta\cos\phi\sin 80^\circ}A_{80^\circ}\right) \tag{6.30}$$

Equations 6.29 and 6.30 will be used for calculating A_1 and A_2 from the measured asymmetries. The selection of data which is to be used in the calculation of A_{80° and $A_{\parallel}$, and the calculation of coefficients in the kinematic bins requires care and will be discussed later.

6.2 Calculation of Physics Asymmetries $A_{\parallel}$ and A_{80°

Equation 6.29 shows how A_1 is calculated given the double spin asymmetries A_{80° and $A_{\parallel}$. The asymmetries A_{80° and $A_{\parallel}$ are obtained from the event per helicity count after charge normalization, trigger live time correction, application of the dilution factor for those kinematics, and the application of the beam and target polarizations. Radiative corrections need to be applied to the asymmetries as well. When writing the

dependency on these factors out explicitly, the asymmetry for either target orientation takes the form:

$$A = \frac{1}{fP_bP_t}\frac{N_c^+ - N_c^-}{N_c^+ + N_c^-} \tag{6.31}$$

where the $N_c^\pm$ are the corrected event counts for events generate by the indicated beam helicity. In order for $N_c^\pm$ to reflect the rate of the reaction at that helicity, it must be normalized by the amount of charge put on the target at that helicity $C^\pm$, and be corrected for the possibly different helicity deadtimes $l^\pm$. So the corrected counts are $N_c^\pm = N^\pm/C^\mp/l^\pm$, where $N^\pm$ are the raw counts.

Eq. 6.31 will need to be calculated for each target field orientation as well as at different values of x and Q^2. The charge per helicity, $C^\pm$; livetime per helicty (livetime will be used here instead of deadtime), $l^\pm$; and the target and beam polarizations, P_t and P_b, are independent of the kinematic variables and will have global values assigned to them on a run by run basis. The dilution factor, f, is different for each target load, and is a function of the kinematics. Therefore, f will be calculated on a bin by bin basis for each target load.

6.2.1 Binning

The count asymmetry, which is calculated using many events, can only be calculated in bins with a finite width. On a run by run basis the DIS electron events are sorted by the beam helicity signal, whether positive or negative, and by what kinematic bin they fall into. The kinematic bins are constructed in Bjorken x and Q^2 according to the minumum width that can be resolved by the energy resolution of the detector system. The Q^2 bins were $(1.89, 2.55)$,$(2.55, 3.45)$, and $(3.45, 4.67)$. Data at higher Q^2 is outside of the DIS region. In order to construct the bins for each data set, a central Q^2 value is chosen, and a starting high value of x_i is picked based on the kinematic coverage for that data set. The starting x_i value corresponds to a unique

scattering energy, $E'_i = E_{\text{beam}} - Q^2/2Mx_i$. This E'_i value is the center of the first E' bin. The bounds of the E' bin are determined by the calorimeter resolution– $(E'_i - \delta E'_i, E'_i + \delta E'_i)$, where $\delta E'_i = \text{Eres}(\%) \times \sqrt{E'_i}$. Table 5.3 shows the resolution coefficients for the diffent energy settigns. Once the bounds on the E' bin have been obtained, corresponding bounds for the x bin can be calculated. The width of an x_i bin is $\dfrac{Q^2}{M(\nu^2 - \delta E'^2_i)}$. The next $x_{(i-1)}$ bin can be calculated using the lower bound on the current bin as the upper bound on the $(i-1)th$ bin and solving for the new $E'_{(i-1)}$ bin center. Simple kinematic relations can be used to calculate bins in θ, W, ν, etc. once the x and E' bins are constructed.

A set of bins for each data set is constructed. When sets need to be combined, the bins of the set with the largest bin width is adopted. In the case when one data set's bins extend past the other's, the more extensive one's bins are used past the region of common binning.

So each kinematic bin has some number of positive and negative helicity counts, N^+ and N^-, which can then be used to calculate $\frac{N^+ - N^-}{N^+ + N^-}$. The statistical accuracy of the count asymmetry calculation is approximately $1/\sqrt{N}$ when $N^- \approx N^+$. The kinematic coverage of all events in their initial minimal bins is shown in figures 6.3 and 6.4. These are simply histogrammed DIS events, with no regard to the helicity. Bins in x can be combined in later analyses in order to improve the accuracy of the calculation of values within that region of x.

The analysis was separated in to four data sets (table 6.1). Each data set was treated and binned separately and combined at the end in order to calculate the final physics quantities.

The establishment of values for P_b and P_t on a run by run basis was already treated in sections 5.2.6 and 5.3.6 repectively. Below, the remainder of the steps of the analysis will be filled in:

- event selection: the criteria used to obtain good DIS electron events for the

calculation of the count asymmetry

- charge per helicity and the beam asymmetry
- livetime calculations (non trivial due to a DAQ setup error)
- dilution factor calculation
- combining the data sets from the different run settings

Start Run	End Run	Target Orientation	Beam Energy	Star Date	End Date
72417	72795	80°	5.9GeV	02/10/2009	02/25/2009
72815	72890	80°	4.7GeV	02/27/2009	03/04/2009
72912	72961	180°	5.9GeV	03/05/2009	03/09/2009
72970	73042	180°	4.7GeV	03/12/2009	03/16/2009

Table 6.1: Experiment Settings Date and Run Breakdown

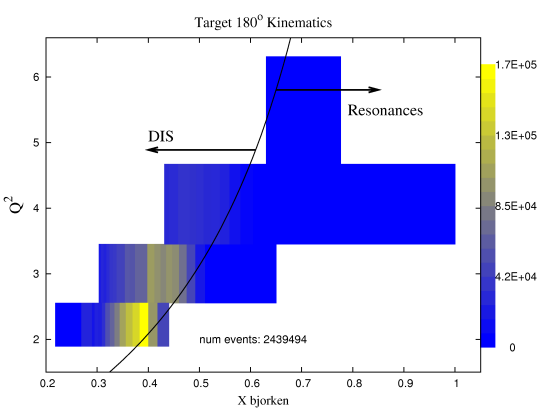

Figure 6.3: Bins in x and Q^2. All data is shown from both energy settings with the target polarization anti-parallel to the incoming electron momentum. The number of selected events that fall within each bin is indicated by the logarithmic color scale. The curve is the $W = 2$ line that separates the deep inelastic scattering region from the resonance region

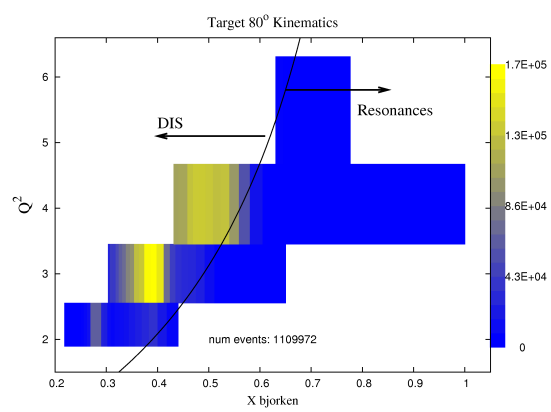

Figure 6.4: Bins in x and Q^2. All data is shown from both energy settings with the target polarization at 80° relative to the incoming electron momentum. The number of selected events that fall within each bin is indicated by the logarithmic color scale. The curve is the $W = 2$ line that separates the deep inelastic scattering region from the resonance region

6.2.2 Event Selection

Several cuts and restrictions are placed on the event population before they are available for binning and further analysis. Only events with trigger type BETA2 (section 5.4.1) were used, which is a coincidence of an above threshold ADC signal in the Cerenkov and a cluster in the calorimeter. Only single cluster events were used (see section 5.7.1). These two cuts identified the particle as an electron or positron, and eliminated ambiguity as to which cluster corresponds to the particle that caused the Cerenkov signal. An additional Cerenkov mirror dependent cut was placed on the cluster position, eliminating rare coincidences between simulataneous background hits in the Cerenkov detector and the calorimeter. Eight regions on the calorimeter are defined, each corresponding to a mirror in the Cerenkov, and a cluster in the region matching the mirror ADC that fired is required for an event to pass this cut (shown in Fig. 6.5). A cut was also placed on the time between the BigCal and Cerenkov detector signals.

The energy of a cluster was required to be above 1.3 GeV before being included in the data. Positron background dilutes the low energy data, and the 1.3 GeV cut avoids much of the region where positron dilution is significant.

A cut of $W > 2$ GeV so that only data from the deep inelastic region is being analyzed.

Because of the nature of the calorimeter calibration, its edges are not well calibrated. Events were discarded if their reconstructed calorimeter coordinate was within 10cm of the edge of the calorimeter.

Runs were included in the analysis if there were no problems reported in the experimental log during that run, and if the run had a charge averaged target polarization greater than 50%. Runs with frequent beam trips, ROC crashes, or suspected mismanagement of the target were flagged and not used in this analysis. Those runs are being saved for more careful processing and may be included for additional statistics

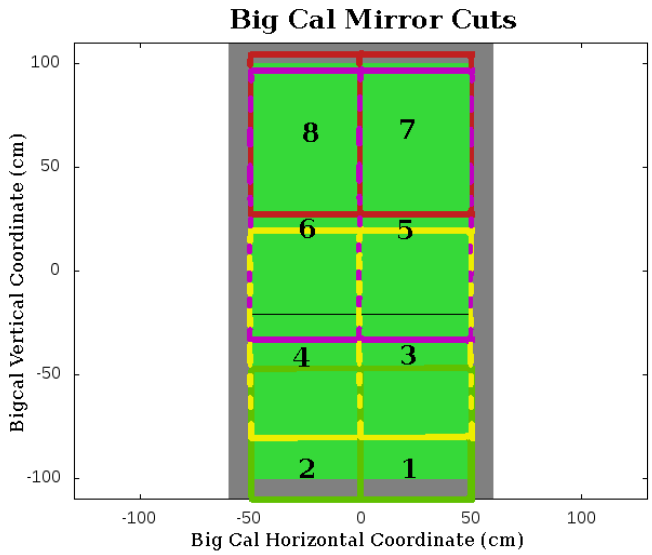

Figure 6.5: Regions in BigCal used for the correlation cut. The mirror number labels the region where a cluster must appear if an event was triggered off of that mirrors PMT. Mirrors 1 and 2 cover vertical range on the calorimeter -110cm to -47cm, mirrors 3 and 4 cover -81cm to 21cm, mirrors 5 and 6 cover -33cm to 97cm, and mirrors 7 and 8 cover 27cm to 105cm. The band around the edge is the 10cm edge cut on the calorimeter cluster position.

once it has been ascertained that the data from those runs are reliable.

6.2.3 Beam Charge

As mentioned in the accelerator chapter, the helicity of the beam is indicated by a signal from MCC to Hall C. The helicity signal is used to gate two scalers (one for positive helicity and one for negative) that record the BCM signal. The helicity gated BCM scalers are read out every two seconds with the other scalers and recorded in the data stream. The total accumulated charge per helicity is stored in the run reports and used as C^+ and C^- for the normalization of the counts in equation 6.31.

The beam charge per helicity asymmetry is small. Before run 72800 the beam charge per helicity asymmetry averaged 0.123%, and afterwards 0.0132%. The change in average helicity asymmetry occurred after a beam energy change.

There was a documentation error, and it was not recorded which scaler records

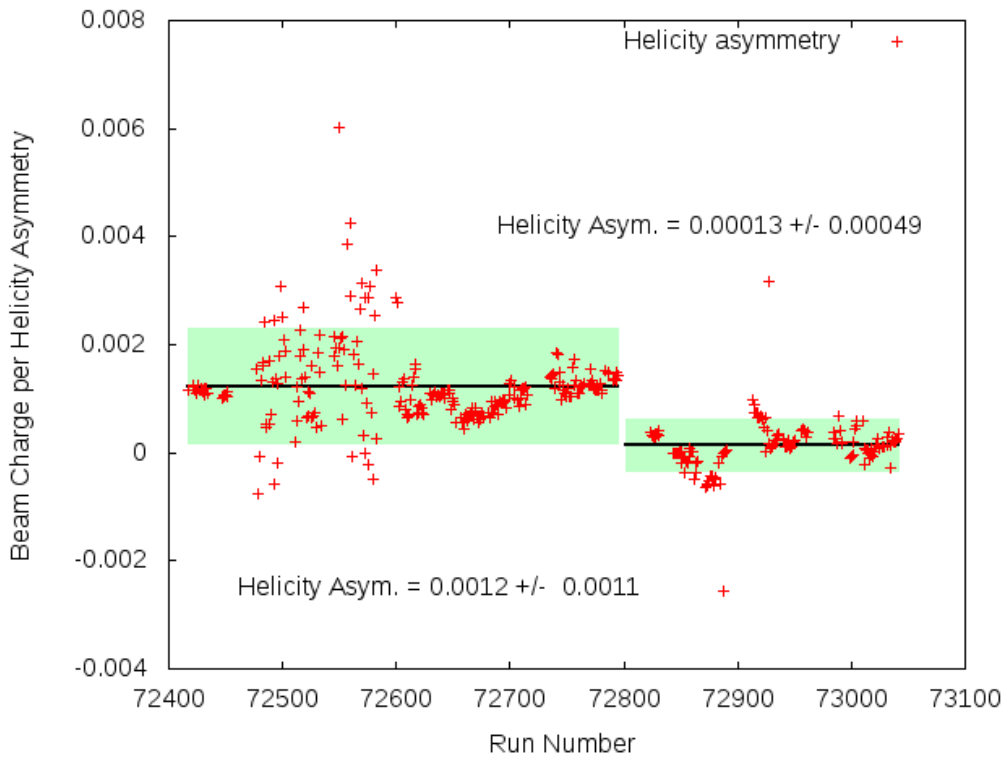

Figure 6.6: Charge per helicity asymmetry as a function runs. Averages for the different regions are indicated by a black line, with the shaded area covering one standard deviation on either side. The jump is due to a change in the accelerator after a beam energy change around run 72814. Labels on either side of the jump give the average asymmetry for that series of runs.

positive helicity charge and which negative helicity charge. In order to determine which scaler was recording which helicity, the low energy 0.5GeV $< E' < 0.8GeV$ events in the near perpendicular target data set were used to calculate a raw count asymmetry for each run:

$$A_{\text{raw}} = \frac{1}{P_b P_t} \frac{N^+/C^+ - N^-/C^-}{N^+/C^+ + N^-/C^-}, \tag{6.32}$$

where no attention is paid to the kinematics of the events, and the charge normalization is presumed. In this energy region there are farily high statistics for each run, and there is a measurable raw asymmetry. Calculating the asymmetry across runs twice with both possible charge normalization possibilities reveals which scaler

is counting which helicity.

For the near perpendicular target data set examined, the raw asymmetry is positive. To see what effect switching the charge normalization will have on the calculated asymmetry, suppose that the amount of positive helicity charge put on the target per run is greater than the negative helicity charge amount (this is in fact the case). The counts per helicity divided by the charge per helicity, if the helicity signs are correct, is proportional to the rate for that helicity. If the charge normalization is correct, the count asymmetry will have a constant value across all run. If charge normalization is incorrect, the positive helicity rates will appear lower than their true value. The runs over which the asymmetries are being calculated have different polarization signs, so the $P_b P_t$ product switches signs, and the value of the rates for positive and negative helicity events are swapped when this occurs. With the correct charge normalization, the change in sign in $P_b P_t$ matches the sign change in $N^+/C^+ - N^-/C^-$, and the asymmetry is unchanged. If the charge per helicity is misassigned, then $N^+/C^+ \rightarrow N^+/C^-$ and the rates for positive helicity events are enhanced. This would lead to an enhancement and suppression of the count asymmetry that matches the target polarization sign flip.

This is indeed what is seen in Fig. 6.7, and so the normalization assignment that produced Fig. 6.8 was taken to be correct.

6.2.4 Livetime Correction

There are scalers, which are read out and stored in the event files, that count triggers per helicity as they are sent to the Trigger Supervisor regardless of whether the DAQ ends up recording that event. A calculation of the livetime is simply the DAQ recorded positive or negative helicity events divided by the scaler recording triggers of that helicity. Unfortunately, this could only be done for the negative helicity scalers, as the positive helicity scaler was not connected to the DAQ system.

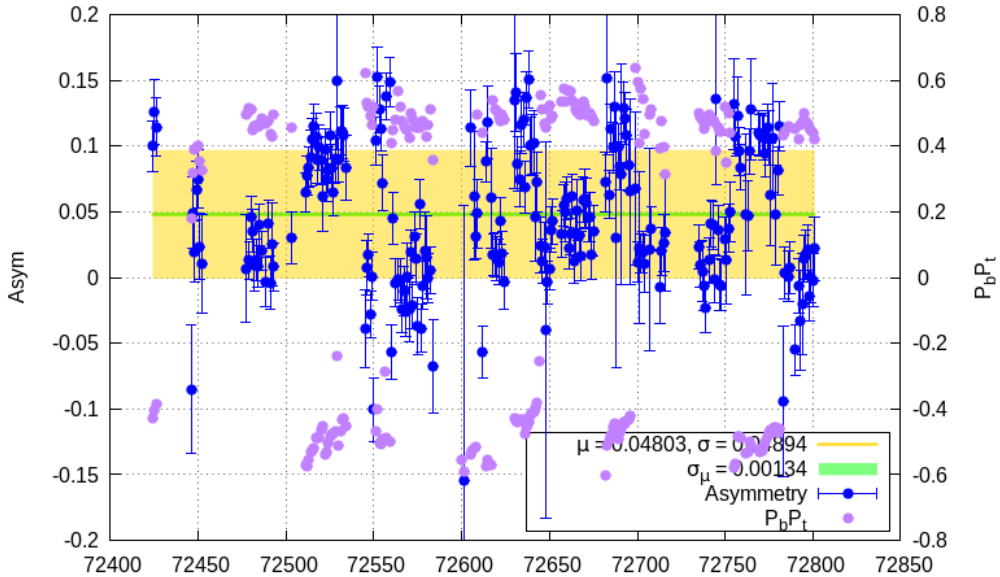

Figure 6.7: Count asymmetries from runs 72400 to 72800 with no Cerenkov Detector cut, E' cuts below 0.5GeV and above 0.8GeV, one cluster only and BETA2 trigger. Here the incorrect charge normalization is used, and the asymmetry value can be seen to clearly depend on the target polarization sign.The product P_bP_t is plotted on the right axis to indicate the target sign for each run.

However, data was stored from a scaler that counted all triggers, be they positive, negative, or unpolarized. The positive helicity scaler counts can be recovered from the total scaler count and the negative scaler count. The number of events for which there is no helicity signal is small, but the uncertainty in that number is larger than the difference between the helicity scalers. Consequently, approximating the positive helicity scaler count as the total scalers minus the negative scalers is inadequate for the purpose of determining the livetime.

The total number of scalers can be expressed as

$$S^{all} = \kappa \cdot (S^+ + S^-), \tag{6.33}$$

where κ is close to one and corresponds to the live time fraction of the all-triggers scaler. During runs with the carbon target, the physics asymmetry is zero. Con-

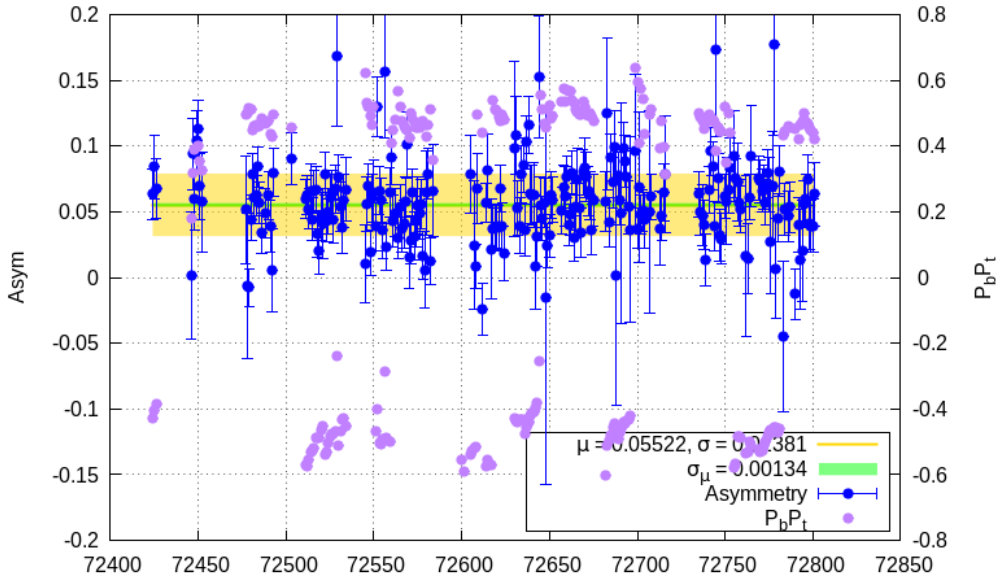

Figure 6.8: Count asymmetries from runs 72400 to 72800 with no Cerenkov Detector cut, E' cuts below 0.5GeV and above 0.8GeV, one cluster only and BETA2 trigger. Here the correct charge normalization is used, and the asymmetry value can be seen to be independent of the target polarization sign. The product P_bP_t is plotted on the right axis to indicate the target sign for each run.

sequently, any rate would be due to the asymmetry in the beam charge, and we have

$$\frac{S^+}{S^-} = \frac{C^+}{C^-}, \tag{6.34}$$

which is to say that the ratio of the scalers should be equal to the charge helicity ratio. Calculating

$$\kappa = \frac{S^{all}}{S^-(1 + \frac{C^+}{C^-})} \tag{6.35}$$

for a series of carbon target runs, an average value of 0.988 ± 0.002 was obtained. This resultant κ comes from the fact that there is zero physics asymmetry for the carbon runs.

One can also calculate the value for κ by assuming the livetime for a helicity is a function only of the rate of events for that helicity– in other words the supposition is that the electronics recording and counting either helicity were behaving identically.

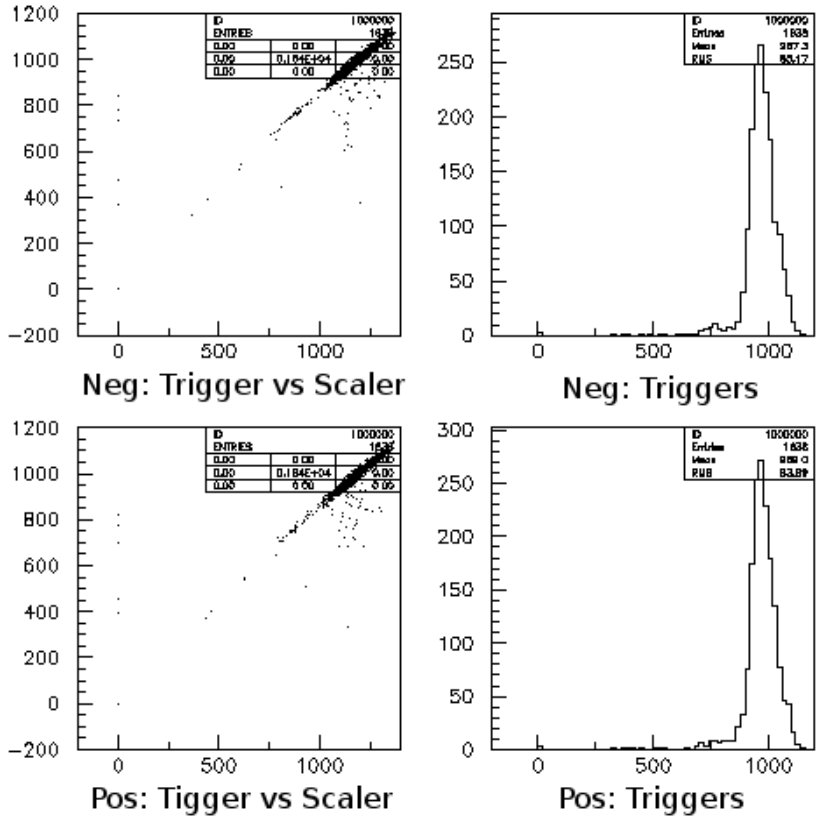

Figure 6.9: Recorded triggers versus scaler counts for both positive and negative helicities and the corresponding projection onto the trigger axis. The top is the negative helicity scalers versus triggers. The bottom is the positive helicity scalers versus triggers, using the reconstructed positive scalers counts.

The dependence of the number of recorded triggers on the scaler trigger count should be the same for each helicity. For several $^{14}NH_3$ runs the positive helicity scalers were reconstructed using κ values ranging from 0.96 to 1.0. The reconstructed scalers for run 72795 can be seen in Fig. 6.9. Linear fits to the recorded trigger versus scaler plots were made for both helicities (the reconstructed scalers being used for positive helicities). The difference between the resultant fit was characterized by the area between the lines is shown in Fig. 6.10 and also by the χ^2 over the number of degrees of freedom in Fig. 6.11 where the expected value is taken to be the negative helicity

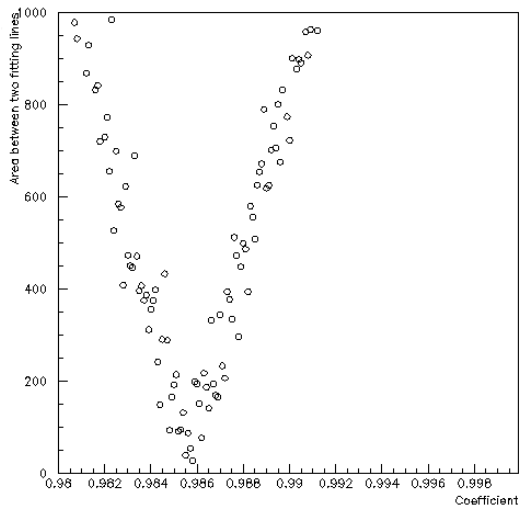

Figure 6.10: Difference in area between fit lines (y-axis) as κ (x-axis) varies.

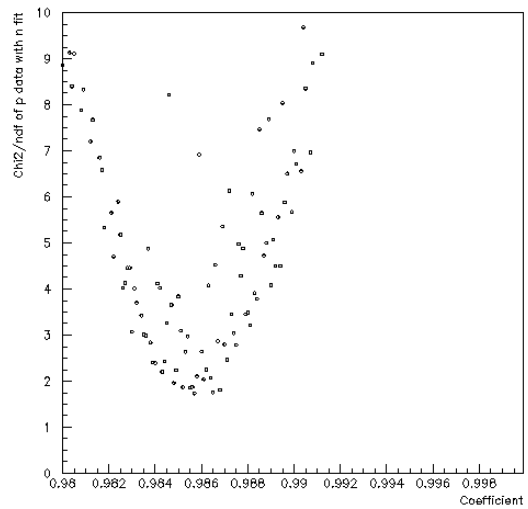

Figure 6.11: χ^2 (y-axis) of the positive scaler fit as κ (x-axis) varies

fit and the observed value taken to be the positive helicity fit. In both cases, the characterized difference between the lines was minimized clearly at a κ of 0.985.

The livetime correction work was done by collaborator Hoyoung Kang. Further information available in Ref. [53].

6.2.5 Radiative Corrections

Bremsstrahlung was mentioned when discussing the calorimeter and how energy is deposited in an electromagnetic shower. The radiation of energy by the electron through the *bremsstrahlung* process is not restricted to the calorimeter. The electron can radiate energy in any of the materials before or after the target. The radiation of energy before or after the target by the electron has the effect of shifting the energies E' and E_{beam} at which the scattering process takes place away from the values measured by the detector and the beam line respectively. Bremsstrahlung prior to the target means that the scattering takes place with a lower energy than the measured beam energy. Radiation of energy after scattering has taken place means

that the scattered particle's energy was higher than that measured in the calorimeter.

The acceleration of the electron during the scattering process results in Bremsstrahlung radiation, meaning that in addition to energy radiated away in the material prior and post-target, there are radiative effects that derive from the scattering process being measured. These are referred to as "internal" radiative effects, and the previously discussed phenomena are called "external" radiative effects. The internal radiative effects are treated as a correction to the Feynman diagram describing the scattering. An additional photon vertex is added to the electron leg before or after it emits the virtual photon that interacts with the proton.

The radiative effects act on the data in such a way as to shift the true kinematics at which the interaction takes place away from the measured kinematics. The spreading out of the elastic events in the W spectrum is pronounced enough that the data can have significant contributions from elastic events, despite the cut at $W > 2$GeV. Figs. 6.12 and 6.13 show how radiation of a photon can shift the W spectrum. States at lower W can affect the measurements at higher invariant mass. Notably, it is necessary to calculate and subtract out the radiative tail of the proton elastic peak, as it extends into the SANE data range. Discussion of the sizeable effect of the radiative tail from the elastic and quasielastic region can be found in reference [54].

The radiative effects come into play for the inelastic region as well, but to a lesser extent. This analysis will not include corrections for inelastic radiative corrects, and they will be considered as part of the systematic error. This analysis only includes a subtraction of the elastic contribution. The subtraction proceeds as follows.

The charge normalized measured asymmetry, corrected for beam and target polarization and dilution factor, is A_T^r, where r indicates that the quantity has not been corrected for radiative effects, and T indicates that it is the total measured quantity. Rather than A_T^r, the quantity of interest is A_{in}^r, which contains only contributions from the inelastic region. The superscript r will be surpressed henceforth, as the full

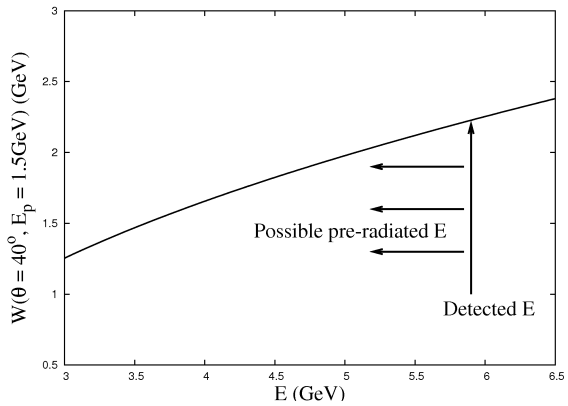

Figure 6.12: Invariant mass, W(GeV), as a function of beam energy, E(GeV), at fixed scattering angle and scattered energy. The radiative effects, which cause the scattering to take place at an energy lower than the measured beam energy, skew phenomena towards higher W.

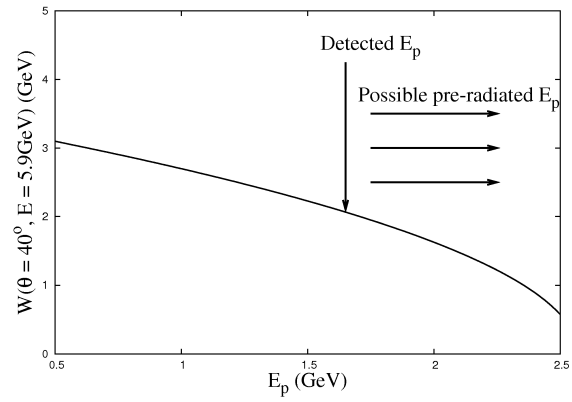

Figure 6.13: Invariant mass, W(GeV), as a function of scattering energy, E'(GeV), at fixed scattering angle and beam energy. The radiative effects cause the scattered particle to have a lower energy when detected than what it had immediately after scattering, thus skewing phenomena towards higher W.

radiative corrections will not be applied until a later analysis. A_{in} will be understood to be the radiated asymmetry from only inelastic processes.

$$A_T = \frac{\Delta_T}{\Sigma_T} = \frac{\Delta_{in} + \Delta_{el}}{\Sigma_{in} + \Sigma_{el}}, \tag{6.36}$$

where the subscripts denote whether the quantity is a contribution from elastic or inelastic processes. The Σ's are total unpolarized cross sections, and the Δ's are polarized cross sections differences. The inelastic asymmetry can be written as

$$\begin{aligned} A_{in} &= \frac{\Delta_T - \Delta_{el}}{\Sigma_{in}} = \frac{\Sigma_T A_T - \Delta_{el}}{\Sigma_{in}} \\ &= \frac{1}{f_{rc}} A_T - A_{rc}, \end{aligned} \tag{6.37}$$

where

$$\frac{1}{f_{rc}} = \frac{\Sigma_T}{\Sigma_{in}} \text{ and } A_{rc} = \frac{\Delta_{el}}{\Sigma_{in}}. \tag{6.38}$$

The inelastic asymmetry, with the elastic contribution removed, can be expressed

in terms of the total measured asymmetry, A_T, and the factors f_{rc} and A_{rc}. Previous analysis were reffered to in order to obtain the quantities necessary to calculate f_{rc} and A_{rc}. Small modifications related to the polarization angles were made to the code used to subtract the elastic radiative tail in the JLab experiment E06-001; the technote [55] goes into detail on the code.

In general, the code calculates the various cross sections necessary to for the correction factors defined above. The radiative corrections to the elastic cross section were calculated based on models in Refs. [54] and [56]. These models require as input the total thickness of material before and after the target in radiation lengths. The resulting calculations combined with existing data for unpolarized inelastic scattering give the Σ_T factor. The calculation of the radiated elastic polarized cross sections for obtaining Δ_{el} is covered in Refs. [57] and [58]. A list of radiation lengths before and after the target can be found in Table 6.2. The correction factors from the elastic tail calculation are separated by Q^2 bin and shown in Figs. 6.14 - 6.19. Most of the work done on the radiative tail subtraction was accomplished by collaborator J. Maxwell.

The calculation of the inelastic polarized radiative corrections has not begun. The the correction is expected to be small. The radiative corrections in the inelastic region for E143 [19] are quite small, less than 1% to the asymmetry. The uncertainty in the radiative correction depends on the accuracy of the model used to represent the data in the inelastic region, and on the accuracy of the structure functions in the region of interest for the elastic tail subtraction. A thorough investigation into the systematic uncertainty of the radiative corrections have yet to be performed, but for the purpose of this document, the estimate of E143 will be adopted, as the kinematic region they took their measurement at is similar to SANE's. Their estimate in addition to an expected approximate 1% correction in the inelastic region gives a 3% error contribution from the radiative corrections.

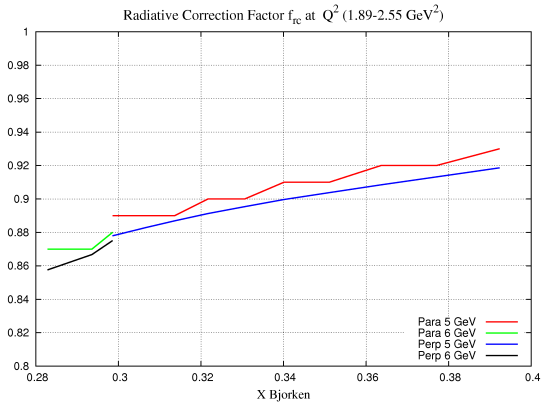

Figure 6.14: Correction factor f_{rc} for the first Q^2 bin.

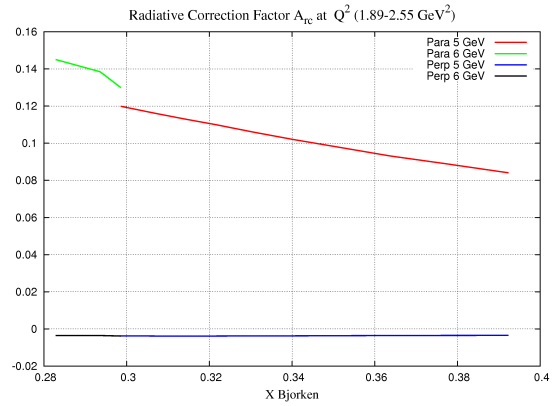

Figure 6.15: Correction factor A_{rc} for the first Q^2 bin.

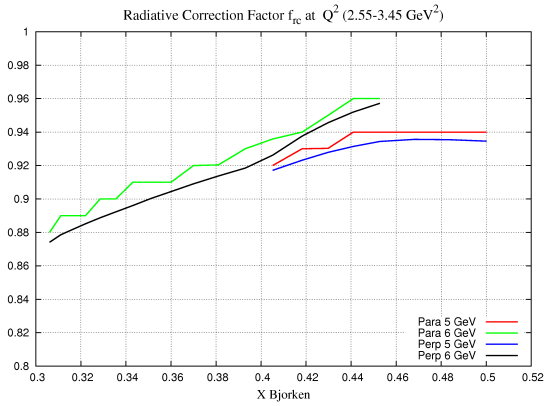

Figure 6.16: Correction factor f_{rc} for the second Q^2 bin.

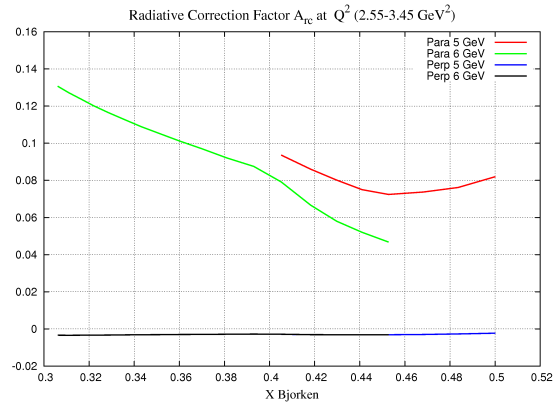

Figure 6.17: Correction factor A_{rc} for the second Q^2 bin.

6.2.6 Background Events

Any particle that can masquerade as an electron that resulted from deep inelastic scattering is a background contaminant in the data. Positrons and electrons produced from neutral pion decay are the primary source of such particles. Neutral pions decay either into γe^+e^- (1.2%) or $\gamma\gamma$ (99%). The photons then have a chance to pair convert in the target or the tracker in time to trigger the Cerenkov detector. If the pion energy was high enough for the decay product to reach the 1.3 GeV threshold, the resulting BETA4 trigger event appears to the detector system to be a good event.

To express the effect of background dilution and background asymmetry, suppose

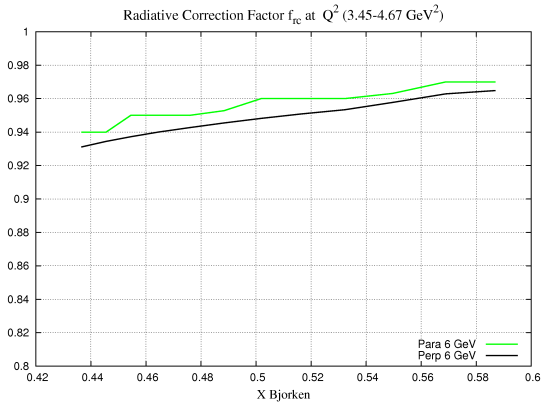

Figure 6.18: Correction factor f_{rc} for the third Q^2 bin.

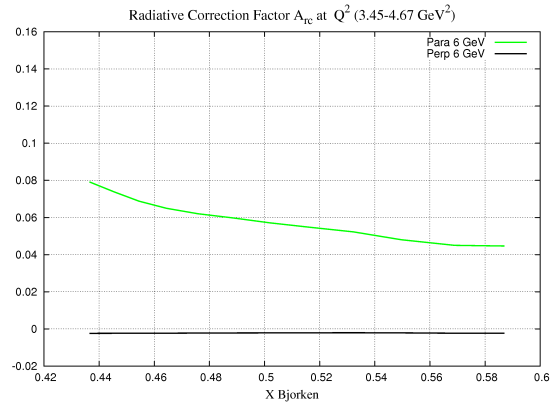

Figure 6.19: Correction factor a_{rc} for the third Q^2 bin.

	Material	Thickness (mg/cm^2)	Rad. Lengths(%)
Target Ammonia	$^{14}NH_3$	1561	3.82
Target Helium	LHe	174	0.18
NMR Coil	Cu	13	0.10
Target Cell Lid	Al	10	0.04
Fridge Window	Al	27	0.12
4K Radiation Sheild	Al	7	0.03
Nitrogen Radiation Shield	Al	10	0.04
Vacuum Chamber Entrance	Be	94	0.14
Vacuum Chamber Exit	Al	139	0.58

Table 6.2: Material thicknesses that contribute to radiative effects. The last columns gives the thickness of the particular material in percents of a radiation length.

in a run there are a number of measured events, N_m, with a contamination of N_b background events. The background has an asymmetry A_b associated with it. The true asymmetry (leaving the polarization, dilution, and other corrections implicit) is

$$A = \frac{N^+ - N^-}{N} = \frac{N_m^+ - N_m^- - (N_b^+ - N_b^-)}{N_m + N_b}, \tag{6.39}$$

where the absence of a subscript indicates that the quantity only includes DIS electrons. If one rewrites the asymmetry in terms of the measured asymmetry, A_m, and

the background asymmetry, A_b, one gets

$$A = \frac{A_m - f_b A_b}{1 - f_b}, \tag{6.40}$$

where f_b is the ration of background events to total measured events, N_b/N_m. There are two effects here – one: the dilution due to the presence of a background, and two: the apparent enhancement of the asymmetry due to the presence of a background asymmetry.

During the run time of the experiment eg1b in Hall B at JLab, the positron dilution was measured at kinematics within the range of SANE's. One of the collaborators of eg1b, V. Dhamawardane, parameterized the dilution at scattering angles of 34.7° and 41.1° with E' from $0 - 3.6$ GeV and found

$$f_b = 4.122e^{-2.442E'} \tag{6.41}$$

to match the data well within that region. The CLAS data exhibited no angular dependence from 32° to 40°. The background in SANE will be higher because of the additional radiator length for pair conversion between the target and the Cerenkov. The ratio of radiator lengths of SANE to eg1b is 2.14, and an increase in the background by the same factor is expected. There was also a measurement of the parallel asymmetry of the positron background with the CLAS detector, which gave an asymmetry of about 20% of the measured asymmetry.

Efforts are currently being made to estimate the pion asymmetry in SANE's data. Some estimate of the positron background will be made using data from the forward tracker in the near future. For the purpose of this analysis, the paramaterization of the background from eg1b will be used, and an estimate of the background asymmetry to be 20% of the measured asymmetry will be made. Large conservative systematic uncertainties will be assigned to these values until better measurements of them can

be made.

The contribution to the error due to the uncertainty in background and background asymmetry is $\left(\frac{\partial A}{\partial f_b}\right)^2 (\delta f_b)^2 + \left(\frac{\partial A}{\partial A_b}\right)^2 (\delta A_b)^2$, which using the above estimates is

$$\frac{f_b^2}{(1-f_b)^2}(0.2)^2(A_m)^2 + \frac{(.4f_b - 1.2)^2}{(1-f_b)^4}A_m^2(\delta f_b)^2. \tag{6.42}$$

The both terms contribute an error on the order to $10\% A_m$ at 1.3GeV and then tail off sharply at higher E'. A table of the error contribution is given in Table 6.3

E'(GeV)	$(\partial A/\partial A_b)^2(\delta A_b/A_{DIS})^2$	$(\partial A/\partial f_b)^2(\delta f_b/A_{DIS})^2$
1.3	$(0.145)^2$	$(0.132)^2$
1.5	$(0.073)^2$	$(0.054)^2$
1.8	$(0.030)^2$	$(0.020)^2$
2.3	$(0.009)^2$	$(0.006)^2$

Table 6.3: The contribution to the systematic error from the positron background. The contribution depends on the size of the DIS asymmetry, as the background asymmetry is estimated as a fraction of A_{DIS}.

6.2.7 Packing Fraction and Dilution Factor

The experiment's production target is not composed of pure protons. The target cavity contains liquid helium, nickel, copper, aluminum, and ammonia. Only the electron interactions with the polarized hydrogen nuclei in the ammonia molecules is of interest. It is necessary to estimate the rates coming from objects other than the free polarized protons.

The rate of events from positive and negative beam helicities, R^+ and R^-, can be written down in terms of N_A, the number of scattering nuclei with atomic number A; the corresponding polarized cross sections for electron-nuclei scattering, $\sigma_A^{+/-}$; and a factor involving the beam current and detector acceptances, Φ:

$$R^+ = \Phi\left(N_{14}\sigma_{14}^+ + N_1\sigma_1^+ + \sum_i N_i\sigma_i\right). \tag{6.43}$$

The sum over i includes all non polarized materials. The polarized cross section for nitrogen (σ_{14}^{+}) is shown above, but the contribution to the rates from the nitrogen nucleus is mostly in the form of unpolarized nucleon scattering. The DNP process causes the parasitic polarization of the nitrogen nuclei in the ammonia molecule. The magnitude of the polarization achieved in the nitrogen is only a small fraction of that created in the hydrogen atom population. Furthermore, the number of polarized nucleons in the nucleus is small, and Ref. [59] estimates the polarization of the nucleons in the nitrogen to be about 2%. The effects of polarized DIS scattering from nucleons within the nitrogen will be ignored in the main analysis and included as a systematic error.

The polarized cross section for the hydrogen can be rewritten in terms of the unpolarized cross section and the asymmetry, $\sigma_1^{+/-} = \sigma_1(1 \pm P_b P_1 A_p)$, where A_p is the proton asymmetry and $P_{b(1)}$ is the beam (hydrogen) polarization. So we have

$$R^{\pm} = \Phi \left(N_1 \sigma_1 (1 \pm P_b P_1 A_p) + \sum_i N_i \sigma_i \right), \tag{6.44}$$

and the raw counts asymmetry uncorrected for target and beam polarization would be

$$A_{\text{raw}} = \frac{R^+ - R^-}{R^+ + R^-} = \frac{P_b P_1 N_1 \sigma_1 A_p}{N_{14}\sigma_{14} + N_1 \sigma_1 + \sum_i N_i \sigma_i}, \tag{6.45}$$

where the nitrogen contribution is pulled out of the sum and stated explicitly. Factoring $N_1 \sigma_1$ allows one to express the measured asymmetry as the product of two terms:

$$A_{\text{raw}} = f P_b P_1 A_p \text{ , with } f = \frac{N_1 \sigma_1}{N_{14}\sigma_{14} + N_1 \sigma_1 + \sum_i N_i \sigma_i}. \tag{6.46}$$

The term f is known as the dilution factor, and relates the measured asymmetry to the proton asymmetry. The dilution factor is a ratio between the rates due to scattering from hydrogen nuclei and the rate due to scattering from all nuclei in the

target inclusive. The measured rates are radiated, and therefore any model Born cross sections must be radiated to match the measured quantities. The ratio of rates depends on the kinematics of the measurement, and it also depends on the packing fraction of the target. The ammonia production targets are cylindrical cups filled with beads of frozen ammonia in a bath of liquid helium. The fraction of the target cup's volume that is ammonia is not reproducible with more than 10% accuracy. This means that the relative rates of scatter between helium and ammonia change from target load to target load. A dilution factor must be calculated for each ammonia target load separately, and this factor depends on the volume fraction, which is called the "packing fraction". The packing fraction must be extracted from the data first before the dilution factor can be calculated.

The number density in equation 6.46 can be written in terms of material and target properties : $N_i = N_0 \rho_i z_i / M_i$, N_0 being Avogadro's number, ρ_i, z_i, and M_i being the ith specie's density, effective thickness, and molar mass respectively. Expressing the number density dependence on thickness explicitly, the dilution factor is

$$f = \frac{\frac{3\rho_{NH_3} z_{NH_3}}{M_{NH_3}} \sigma_1}{\frac{3\rho_{NH_3} z_{NH_3}}{M_{NH_3}} \sigma_1 + \frac{\rho_{NH_3} z_{NH_3}}{M_{NH_3}} \sigma_{15} + \frac{3\rho_{He} z_{He}}{M_{He}} \sigma_4 + \frac{\rho_{He} z'_{He}}{M_{He}} \sigma_4 + \frac{\rho_{Al} z_{Al}}{M_{Al}} \sigma_{27}}. \tag{6.47}$$

The primed z_{He} indicates the thickness of the helium external to the target cell and the unprimed z_{He} is the thickness of the helium in the target cell. The aluminum thickness (the target cell lid) and external helium thickness are determined by the geometry of the target. The interior of the target is treated as being composed of solely ammonia and helium-4. The NMR coil is ignored, as its contribution to scattering is negligible. The packing fraction is defined as the percentage of the target cavity's volume that is filled by ammonia, so $z_{NH_3} = l_t pf$ and $z_{He} = l_t(1 - pf)$ where l_t is the target length.

The denominator of Eq. 6.47 is the total scattering rate. It is expressible as a linear

function of the packing fraction. By accurately reproducing rates in a simulation, the parameters for the linear function $Y = m \cdot pf + b$ can be determined, and the experimental packing fraction determined from the rates in the data. With a beam current I and detector acceptance α, the yield (rate) is

$$\begin{aligned} Y &= I \cdot \alpha \left\{ \left[l_t(3\sigma_1 + \sigma_{14}) \frac{\rho_{NH_3}}{M_{NH_3}} - l_t \sigma_4 \frac{\rho_{He}}{M_{He}} \right] pf + (l_t + z'_{He}) \sigma_4 \frac{\rho_{He}}{M_{He}} + \sigma_{27} \frac{\rho_{Al} z_{Al}}{M_{Al}} \right\} \\ &= m \cdot pf + b. \end{aligned} \tag{6.48}$$

The HMS simulation "mc_hms_single.f" was used by collaborator H. Kang to determine the packing fraction. In order to ensure correlation between the simulation and the experiment, Carbon target runs, for which the target thickness was known, were simulated. When calculating packing fractions, the constant that normalized the carbon data to the experimental data was used for ammonia runs in closest temporal proximity. A comparison of carbon data to simulated data can be seen in figure 6.20. The simulation's correspondence to the data varies with the invariant mass, suggesting the simulations model for the cross section might have inaccuracies or that the detector's acceptance over W may be imperfectly modeled.

Simulated ammonia target yields for each load were obtained at two packing fraction values $Y_{MC}(pf = 50\%)$ and $Y_{MC}(pf = 60\%)$. These two points give slope intercept parameters that solve linear Eq. 6.48. The line interpolated or extrapolated from the two points in the simulation can be used along with experimental yields to solve for the packing fraction of ammonia target load. Example data and packing fractions are seen in Table 6.4. The table contains a sample of 5 runs with ammonia targets. Two simulation yields are given at packing fractions of 50% and 60%. The runs are taken from parts of the experiment with different field orientations and beam energy settings, and the HMS was moved during the experiment. This means that the yields collected were at different W and Q^2 values depending on the beam energy and HMS angle. This is why the yields in Table 6.4 differ despite having the same

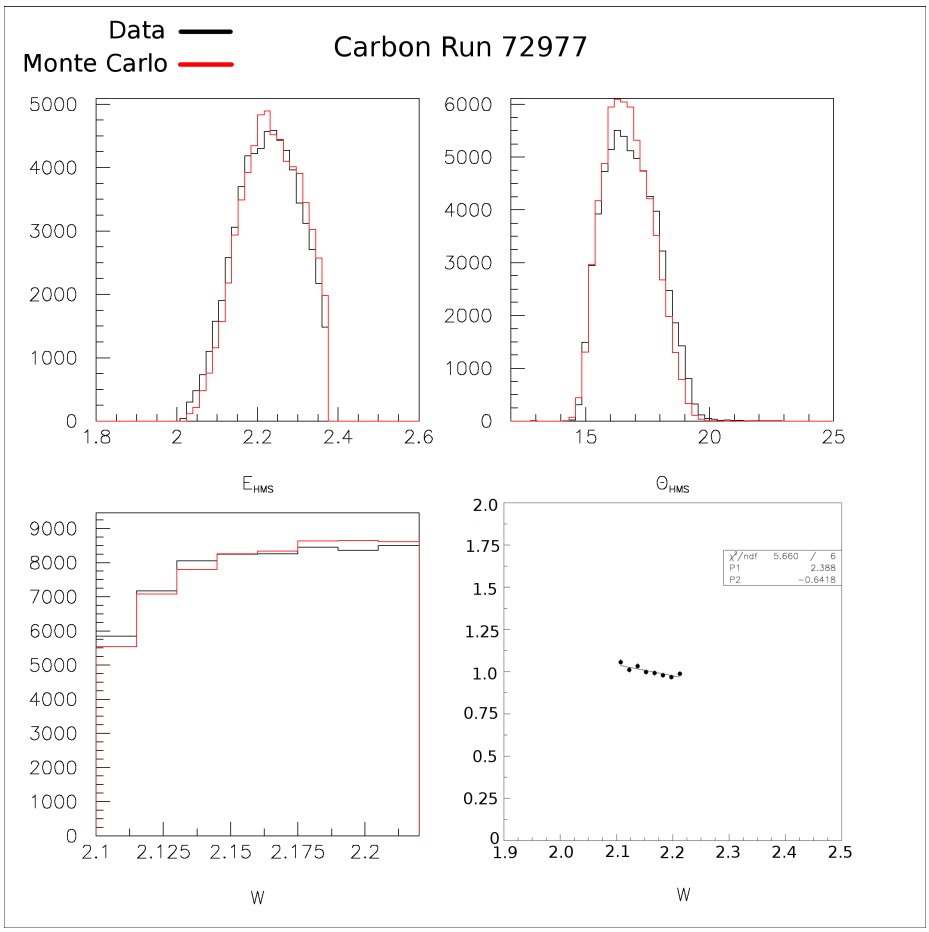

Figure 6.20: HMS Data and HMS Monte Carlo simulation for carbon run# 72977. Monte Carlo data is in color and the real data is in black. Top left: energy spectrum (GeV) Top Right: Scattering angle (degrees) of detected particles Bottom Left: Missing mass (GeV) Bottom Right: Ratio of events (Data/MC) binned.

packing fraction. The m and b columns are the slope y-intercept extrapolated from the simulation yield values. The packing fraction, which is found by locating $Y(data)$ on the extrapolated line, is shown in the last column.

A complete list of packing fractions can be found in Table. 6.5. Using these, a dilution factor can be calculated. For each target load, the Monte Carlo simulation of BETA was run with corresponding experimental settings and packing fraction. The cross sections used in the simulation are Born cross sections, and the rates obtained from it need to be radiated to match the measured rates (see section 6.2.5). The source of each event in the simulated detector was tracked, and the ratio of the rates

Run	C dat/MC	Y (data)	Y MC (50%)	Y MC (60%)	m	b	pf
72379	0.97206	133370.0	118640.0	134367.0	157270.0	40005.0	0.594
72385	0.97206	128262.0	111123.0	125853.0	147300.0	37473.0	0.616
72828	0.97206	135042.0	144639.0	163812.0	191730.0	48774.0	0.450
72957	1.03010	156509.0	137516.0	154615.0	170990.0	52021.0	0.611

Table 6.4: Packing fractions and simulated and experimental yield for sample ammonia runs.

due to hydrogen and the ratio of rates due to all nuclear species were binned in W, ala equation 6.46. Thus the W dependent dilution factor is obtained.

The dilution factor calculation is not yet complete. The packing fractions have been calculated, but work on the BETA simulation is still underway. In order to calculate preliminary asymmetries, an approximation is being used. The packing fraction given by Eq 6.47 can be written in terms of atomic weights, densities, and the ratios of cross sections. The ratio of the helium cross section to the proton cross section can be approximated in terms of the structure functions $F_2^{n,p}$ and the number of neutrons and protons in the helium nucleus:

$$\frac{\sigma_4}{\sigma_1} = 2 + 2\frac{F_2^n}{F_2^p}, \tag{6.49}$$

and similarly for the other materials. Fits of SLAC DIS data [60] for the proton and deuteron are used to calculate the structure function ratios over the DIS region. For the preliminary asymmetries shown in this work, this dilution factor approximation based on the ratio of cross sections is used, rather than that calculated with simulated yields. The dilution factors for SANE's kinematical range are shown in Fig 6.21, using a nominal 50% packing fraction. In the DIS region, the dilution factor is a very slowly varying function of x. The final dilution factors will have an error associated with them driven by the statistics in the simulation. This systematic error will be around 2.5%. Some additional error in the preliminary asymmetry calculation will be assumed due to the usage of this approximation.

Run	Target Cup	Run Range	PF(%)	PF error(%)
72213	Top	72213-72233	70.1	5.16
72247	Bottom	72244-72256	68.2	5.12
72278	Top	72271-72280	49.2	4.19
72281	Bottom	72281-72286	57.9	4.59
72379	Bottom	72378-72379	70.1	5.16
72385	Bottom	72383-72389	72.3	5.97
72658	Bottom	72657-72668	64.4*	5.30*
72672	Top	72669-72676	62.0*	4.94*
72790	Bottom	72783-72792	60.2	4.98
72795	Top	72793-72801	56.9	4.81
72828	Bottom	72824-72831	62.6	4.50
72957	Bottom	72956-72958	60.6	4.68
72959	Top	72959-72962	59.7	4.38
72984	Bottom	72984-72985	73.7*	4.86*
72991	Top	72986-72992	68.0*	4.08*
73014	Top	73013-73018	56.6	4.17
73019	Bottom	73019-73020	58.9	4.45

Table 6.5: The packing fractions calculated for various runs. The run span over which that packing fraction applies. Asterisks(*) mark packing fractions calculated with a yeild to Monte Carlo ratio of 1, because there were no good nearby carbon runs.

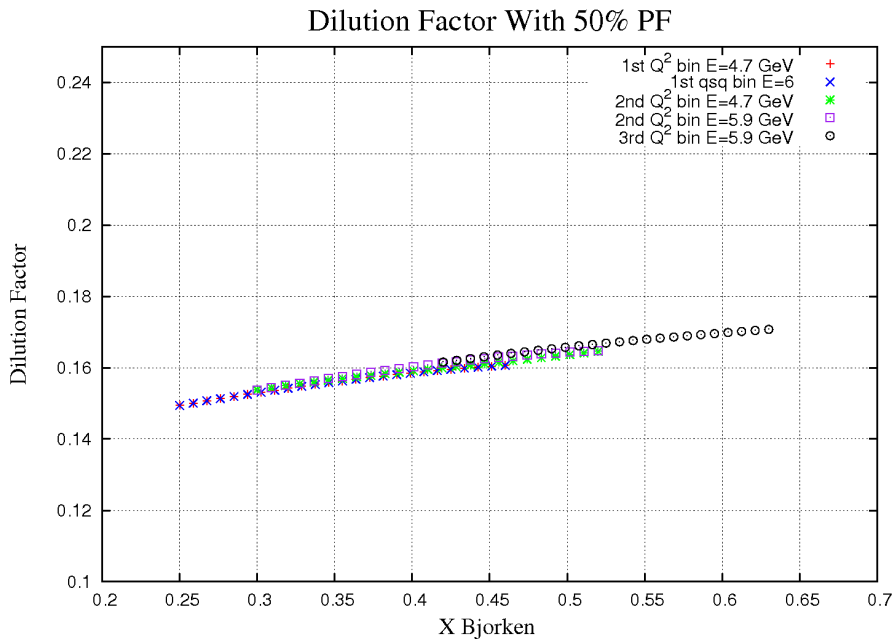

Figure 6.21: Dilution factors calculated using the SLAC structure function fits with a nominal 50% packing fraction. These dilution factors are used in this works preliminary asymmetry calculations (with the correct packing fraction).

6.3 Combining Data Sets

Something rather disingenous was done in section 6.1.2. Here it is shown that the sleight of hand was a matter of convenience, and that the assumptions swept under the rug are justified. In combining equations 6.21 and 6.22 in order to obtain the structure functions in terms of the asymmetries $A_{\parallel}$ and A_{80°, it was assumed that one is combining two functions of x and Q^2 in order to obtain another function of the two variables (don't mind the E's and functions of θ as they can all be expressed in terms of x and Q^2). This is not what is being done at all. $A_{\parallel}$ and A_{80° are measured quantities that have average values within bins of finite width. No longer dealing with continuous real functions on $\mathbb{R}^2$, one is forced to make the swap

$$A_{80^\circ}(x_i, Q_i^2) \rightarrow \{\langle A\rangle|_{(x_i-\delta x_i, x_i+\delta x_i),(Q_i^2-\delta Q_i^2, Q_i^2+\delta Q_i^2)}\}_{80^\circ\text{data}} \tag{6.50}$$

and similarly for the anti-parallel data. The $\langle\rangle$ indicate that an average over the width of the x and Q^2 bin is being taken on the value of the asymmetry. The set of data used in the average is the 80° target data. The x and Q^2 points associated with this data point are not x_i and Q_i^2 but rather the average of the x or Q^2 distribution within those bins. Likewise if one wants the E' or θ value associated with that data point, it is necessary to examine the average of the bin distribution for those variables as well.

Treating $A_{\nparallel}$ and A_{80° as sets of averaged values rather than functions means that in order to proceed from equation 6.21 and 6.22 to equation 6.23 one needs to use bin averaged values. So when one multiplies by a common factor and cancels terms from the A_{80° equality with "identical" terms from the $A_{\nparallel}$ equality, the common terms are the bin averaged values from distinct data sets; thus, and they may not be "common" at all.

Indeed the proper way to perform this extraction of A_1 would be to proceed from equations 6.21 and 6.22 on a bin by bin bases, calculating averages as one goes, and to do this for the 4.7GeV and 5.9GeV data sets separately. Below in section 6.3.1, the bin averaged values of the kinematic quantities for each data set, bin by bin is presented. The variable average values for the 180° and 80° data sets at the same energy are the same within one standard deviation. This fact is relied on in order to justify the algebra used to obtain equations 6.29 and 6.30 for the final calculation. This is not true of the data sets taken at different beam energies. The two target orientation data sets at the same energy will be combined using equations 6.29 and 6.30 to produce A_1 and A_2 for each of the x and Q^2 bins. The different beam energy results will be compared and averaged together afterwards for each bin.

Events were binned as described in section 6.2.1. Histograms for the event's calculated x, Q^2, E', θ,W^2, and ϕ values were created for each x and Q^2 bin. For each bin 6 separate histograms are generated–one for each variable of import.

An aside on ϕ: the ϕ dependence in any of the formulas originates from the perpendicular component of the target polarization, and the ϕ value used in the calculation will be the bin averaged value from the 80° data set.

6.3.1 Bin Averaged Kinematics

The equation used for calculating A_1 and A_2 from the measured asymmetries A_{80° and $A_{\Uparrow}$ has been framed as a function of E, E', θ, and ϕ. On a run by run basis, the average of E, E', θ, and ϕ kinematic variables was calculated within each x and Q^2 bin. This average and the standard deviation of the distribution was stored, and then an average over the runs performed, weighting by the count asymmetry error. This average was performed on both the bin distribution's average and its standard deviation. The variance over the runs was generally much smaller than the average of the distribution's standard deviation. The run averaged values were separated by the Q^2 bin to which they belonged and plotted against the x bin from which they came. Bars were assigned to each data point– their size equal to the quadratic sum of the variance of the average over runs and the run averaged standard deviation of the bin distribution. These bars are not error bars, but rather reflect the variance of the kinematic variable within the bin.

Examining Fig. 6.24, the Q^2 distributions overlap quite well, and the x distributions over lap precisely for the data sets with the same beam energy. This means that the point at which $A_1(x, Q^2)$ is being evaluated within a bin is similar for each target orientation data set. Distributions for other kinematic variables are shown in Figs. 6.22 through 6.25

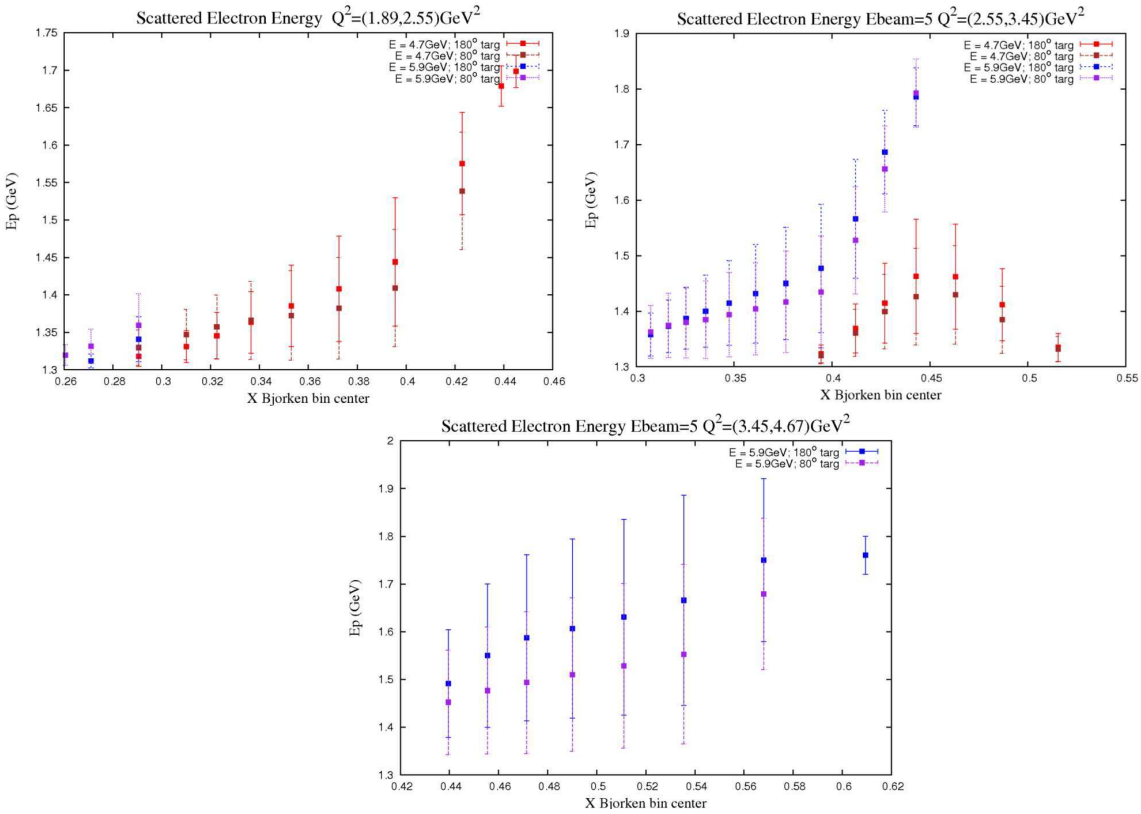

Figure 6.22: Bin distribution averages of scattered electron energy (E') for 4.7 and 5.9GeV data. Perpendicular and parallel data appear on the same plot. Each plot is a different Q^2 bin. Bars indicate the average width of the distribution.

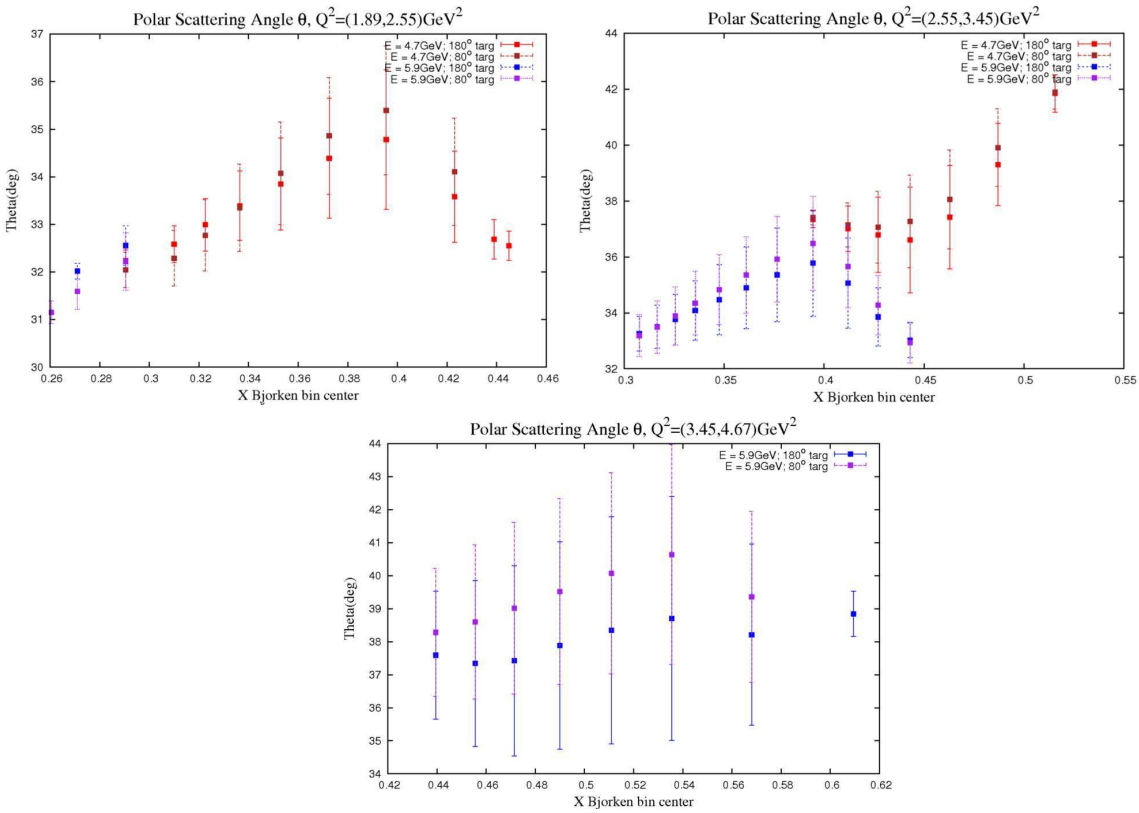

Figure 6.23: Bin distribution averages of polar scattering angle (θ) for 4.7 and 5.9 GeV data. Perpendicular and parallel data appear on the same plot. Each plot is a different Q^2 bin. Bars indicate the average width of the distribution.

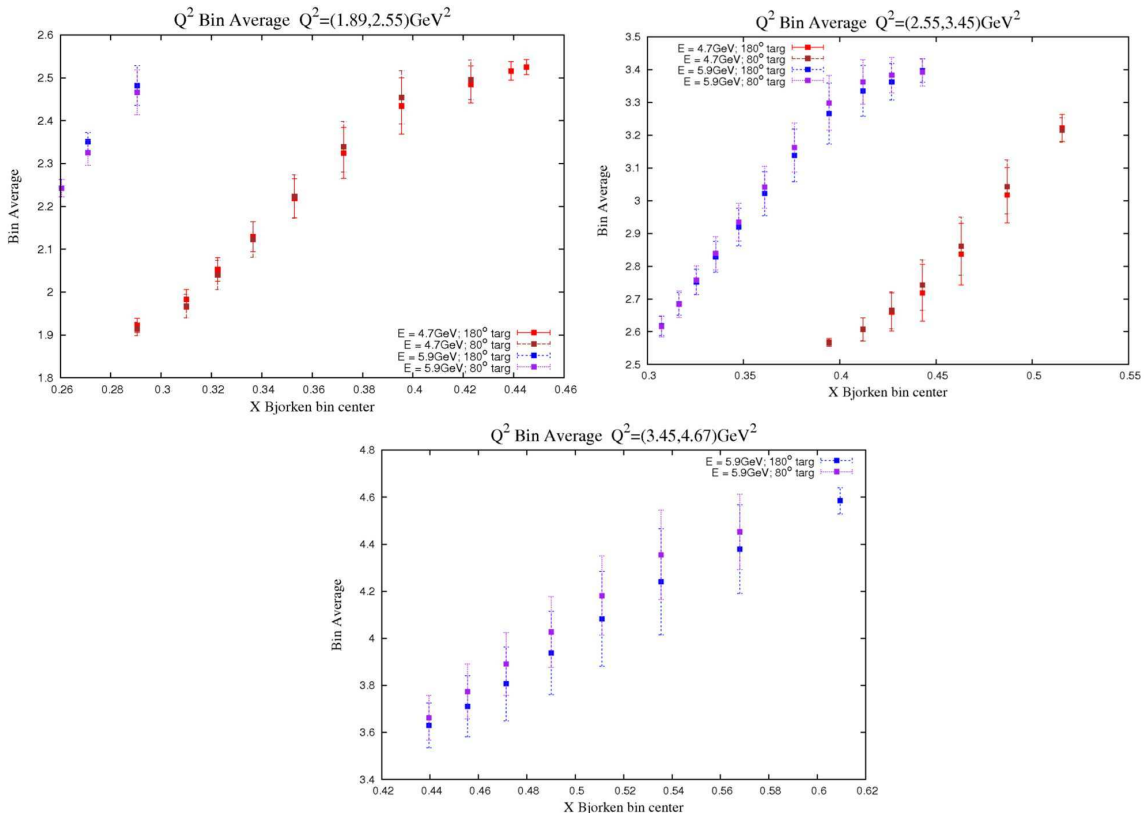

Figure 6.24: Bin distribution averages of Q^2 for 4.7 and 5.9 GeV data. Perp and parallel data for each beam energy appear on the same plot. Each plot is a different Q^2 bin. Bars indicate the average width of the distribution.

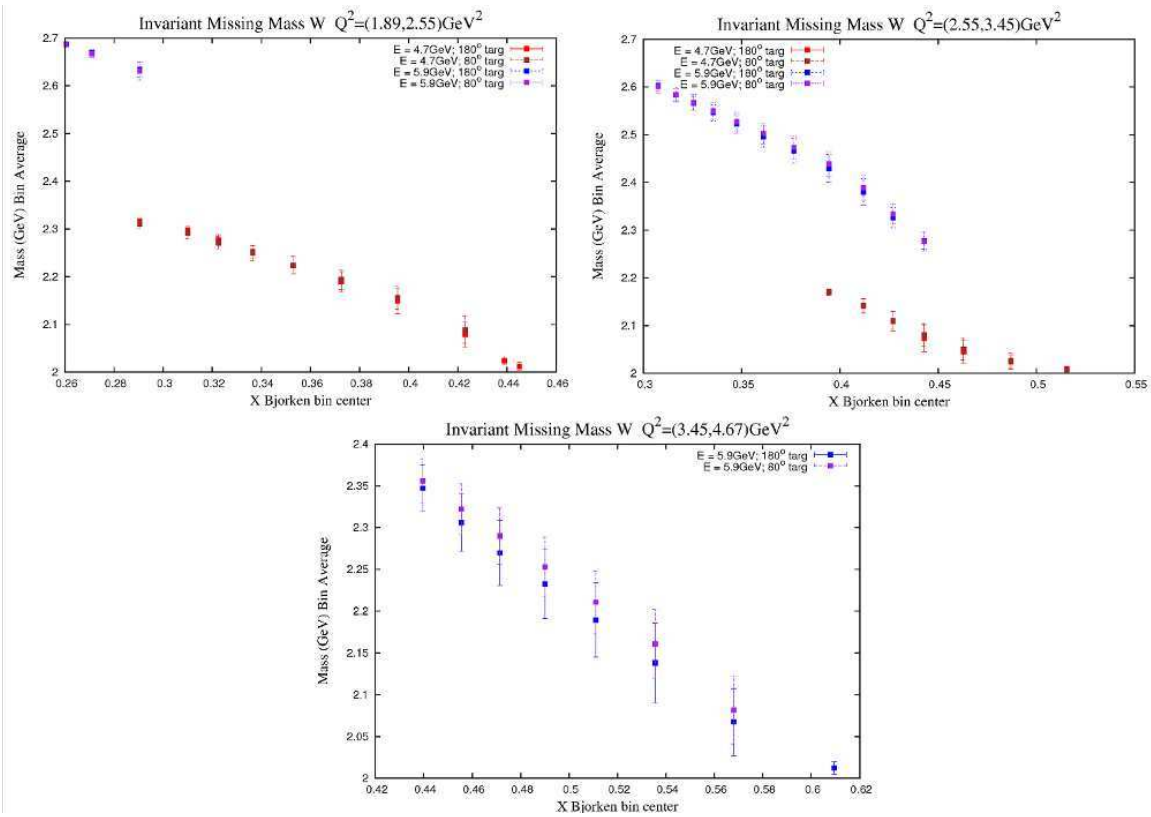

Figure 6.25: Bin distribution averages of W for 4.7 and 5.9 GeV data. Perp and parallel data for each beam energy appear on the same plot. Each plot is a different Q^2 bin. Bars indicate the average width of the distribution.

6.4 Calculation of A_1

The calculation of the virtual Compton asymmetries proceeds as follows. Once detector calibration and position and angle reconstruction are complete, medium level data files are created with the reconstructed scattering angle and calibrated reconstructed energy for the cluster inserted into each event along side of the lower level data (such as ADC and scaler data). The amount of data stored for each event in these medium level data files is fairly large. As an intermediary step towards the calculation of the virtual photon asymmetries, the data for each run is looped over event by event, and trimmed down HBOOK files are made for each run. The event selection criteria are applied to the events, and only those that pass the cuts described in section 6.2.2 are written to the new file. The data that are necessary for the present analysis include beam helicity, polar scattering angle, azimuthal scattering angle, the scattered particle's energy. Along with these data, quantities D' (see section 6.1.1), x_{bj}, Q^2, and the missing mass squared, W^2 are calculated for each event and written to file. Creating a new file with only the events that passed the event selection criteria, and only the quantities necessary for the analysis, greatly accelerates the processing of the data. At this step the information is still stored on the event level and separated by run.

In order to calculate D' for an event, the particle energy and scattering angle need to be reconstructed, and the structure function $R(W, Q^2)$ must be known at that kinematic point. An empirical fit to the inelastic cross section data in the region of SANE's data was performed in reference [61]. The authors of the work and V. Mamyan released a FORTRAN routine containing their fits; this routine was embedded in the analysis code for the calculation of $R(W, Q^2)$.

Each run is looped over, and for each bin in Q^2 a table like Table 6.6 is constructed. Since there are 3 Q^2 bins, that meanse there are $3 \times$ (# of runs) tables.

The asymmetry for each table entry is calculated along with the statistical error:

$$A = \frac{1}{P_b P_t f} \frac{N_c^+ - N_c^-}{N_c^+ + N_c^-} \text{ and} \tag{6.51}$$

$$\delta A = \frac{1}{P_b P_t f} \times 2\sqrt{\frac{N_c^+ N_c^-}{(N_c^+ + N_c^-)^2}}. \tag{6.52}$$

The beam and target polarizations for each run are stored in a look-up table along with the per helicity charge; the table is accessed when processing each run's set of data tables. The dilution factor is stored as run-dependent function of W, and a routine is called, returning f for each line in the table, using that line's $\langle W^2 \rangle_i$.

Treating the data set from each target orientation and beam energy combination separately, the individual bins are averaged together run by run for each table entry, ψ, to obtain the run averaged value for that bin:

$$\langle \psi \rangle = \frac{\sum_i \psi_i / \delta A_i^2}{\sum_i 1/\delta A_i^2}. \tag{6.53}$$

The error in the asymmetry is used for weighting the average, and the sum index, i, is over all run numbers for a particular experimental configuration. The ψ can be any quantity except $N_c^\pm$ from Table 6.6. The asymmetry as calculated in equation 6.51 is similarly averaged over runs. The error on the asymmetry average value is

$$\delta \langle A \rangle = \sqrt{\frac{1}{\sum_i 1/\delta A_i^2}}. \tag{6.54}$$

Once the runs have been averaged over, the asymmetries can be looked at as a function of x. The parallel asymmetries are shown for beam energy 4.7GeV and 5.9 GeV in figures 7.3 and 7.4 respectively. The perpendicular asymmetries are shown in 7.1 and 7.2. There are a few aberrant values from bins with low statistics towards

Run # x^{cent}	N^+	N^-	$\langle x \rangle$	σ_x^2	$\langle Q^2 \rangle$	$\sigma_{Q^2}^2$	$\langle \theta \rangle$	σ_θ^2	$\langle \phi \rangle$	σ_ϕ^2	...
x_1^{cent}	N_1^+	N_1^-	$\langle x \rangle_1$	$(\sigma_x^2)_1$	$\langle Q^2 \rangle_1$	$(\sigma_{Q^2}^2)_1$	$\langle \theta \rangle_1$	$(\sigma_\theta^2)_1$	$\langle \phi \rangle_1$	$(\sigma_\phi^2)_1$	...
x_2^{cent}	N_2^+	N_2^-	$\langle x \rangle_2$	$(\sigma_x^2)_2$	$\langle Q^2 \rangle_2$	$(\sigma_{Q^2}^2)_2$	$\langle \theta \rangle_2$	$(\sigma_\theta^2)_2$	$\langle \phi \rangle_2$	$(\sigma_\phi^2)_2$	...
x_3^{cent}	...	...	...	...	...	...	...	...	...	...	...
x_4^{cent}	...	...	...	...	...	...	...	...	...	...	...
...	...	...	...	...	...	...	...	...	...	...	...

Table 6.6: Data table structure for run-level data processing. A table like this is made for each Q^2 bin. The table continues with entries for E', W^2, and D', but they are not displayed here in order to make the graphic legible.

either end of the x range for a given Q^2.

The asymmetries are ready to be combined using equations 6.29 and 6.30. Call the coefficients of A_{80° and $A_{\nparallel}$ in equation 6.29 α, β, and γ . Equation 6.29 is re-written as

$$A_1 = \alpha A_{\nparallel} + \beta A_{\nparallel} + \gamma A_{80^\circ}, \text{ with} \tag{6.55}$$

$$\alpha = \frac{E - E' \cos\theta}{D'(E + E')}, \tag{6.56}$$

$$\beta = \frac{E' \sin\theta \cos 80^o}{D'(E + E') \cos\phi \sin 80^o}, \text{ and} \tag{6.57}$$

$$\gamma = \frac{E' \sin\theta}{D'(E + E') \cos\phi \sin 80^o} \tag{6.58}$$

The coefficients are calculated in bins at the run level, and averaged over the runs like the other kinematic variables. The coefficients in Eq. 6.55 are taken from different data sets. The α coefficient is taken from the parallel data set, and the β and γ coefficients were constructed using the 80° data set. With the exception of these coefficients are shown in figure 6.26. One can see that the largest contribution to A_1 comes from $A_{\nparallel}$. The contribution from A_{80^o} is small, as the near-perpendicular asymmetry magnitude is significantly less than that of the parallel data, and it is surpressed by γ, which is around 5 times smaller than α.

The 5 GeV and 6 GeV data sets have been individually processed, and A_1 is calculated for each x and Q^2 bin, using Eq. 6.55. Bins which are empty for either

A_{80° or $A_{\nparallel}$ are discarded. The statistical error on A_1 is

$$\delta A_1 = \sqrt{\alpha^2(\delta A_{\nparallel})^2 + \beta^2(\delta A_{\nparallel})^2 + \gamma^2(\delta A_{80^\circ})^2}. \tag{6.59}$$

So for each bin there are now two calculations for A_1– one for each beam energy data set. The final value for A_1 is taken to be

$$A_1 = \frac{\{A_1\}_{4.7GeV}/\{(\delta A_1)^2\}_{4.7GeV} + \{A_1\}_{5.9GeV}/\{(\delta A_1)^2\}_{5.9GeV}}{1/\{(\delta A_1)^2\}_{4.7GeV} + 1/\{(\delta A_1)^2\}_{5.9GeV}}. \tag{6.60}$$

Now the second virtual photon asymmetry A_2 can also calculated using a different set of coefficients for combining the parallel and near-perpendicular asymmetries:

$$A_2 = \alpha_2 A_{\nparallel} + \beta_2 A_{\nparallel} + \gamma_2 A_{80^\circ}, \text{ with} \tag{6.61}$$

$$\alpha_2 = \frac{\sqrt{Q^2}}{2D'E}, \tag{6.62}$$

$$\beta_2 = \frac{-\sqrt{Q^2}(E - E'\cos\theta)\cos 80^o}{2D'EE'\sin\theta\cos\phi\sin 80^o}, \text{ and} \tag{6.63}$$

$$\gamma_2 = \frac{-\sqrt{Q^2}(E - E'\cos\theta)}{2D'EE'\sin\theta\cos\phi\sin 80^o}. \tag{6.64}$$

The results and an estimate of the systematic error will be given in the next chapter.

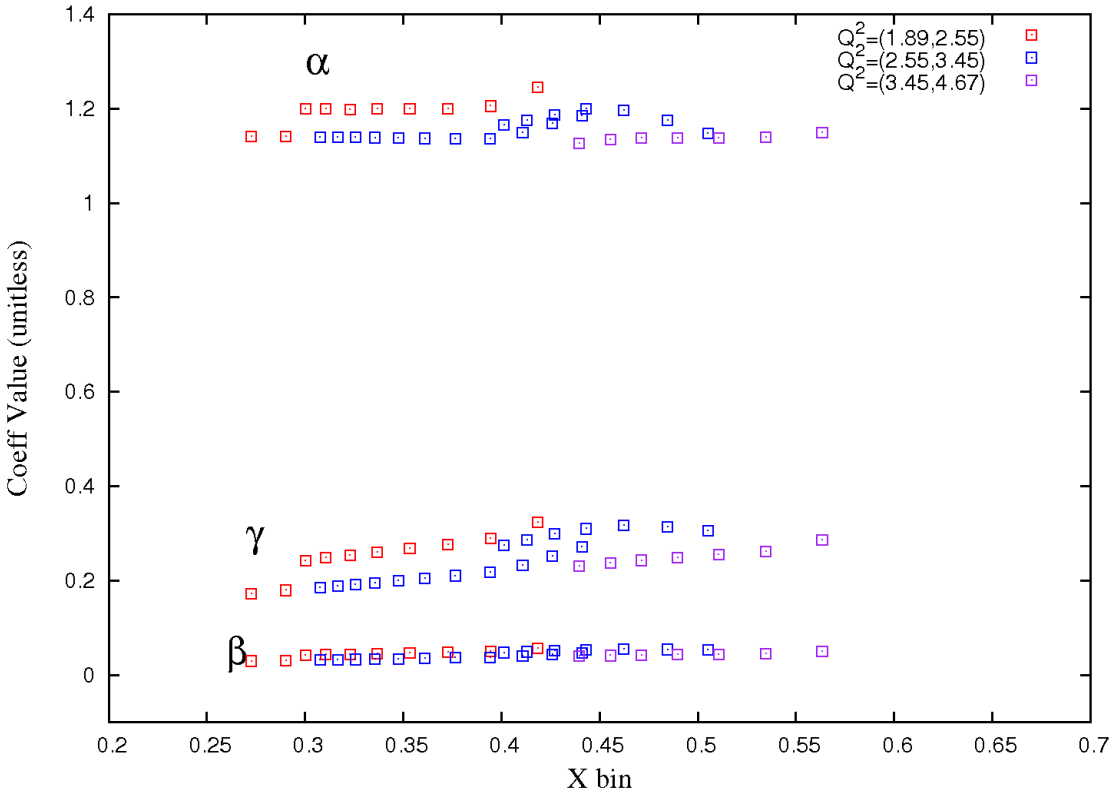

Figure 6.26: The coefficients are neatly separated vertically on the plot and labeled. The Q^2 bin to which each data point belongs is indicated by the legend.

Chapter 7

Results and Discussion

7.1 Systematic Error

Most of the contributions to the systematic error have already been mentioned in previous chapters. Here they will be summarized, and those errors that have not been dealt with previously will be discussed. A final estimatation of the systematic errors will have to wait for a study of the background contribution to complete and more work is to be done on the dilution factors and the inelastic radiative corrections. Below are some conservative bounds on the error based on the current state of the analysis.

The error in the target polarization was discussed in section 5.3.7, and is estimated at 4% based on the fluctuations of the calibration constants between thermal equilibrium measurements.

The statistical error on an individual Møller measurement is about 1%. The fit to the experiment's Møller data that was used to extrapolate the beam polarization at any Wien angle and beam energy contributes at most a 0.5% uncertainty to the beam polarization. See section 5.2.6 for details.

The dilution factor calculation is described in section 6.2.7. The error in the

dilution factor along with the uncertainty due to neglecting the nitrogen polarization was estimated at 3%.

The dilution due to background positrons and electrons is sizable at low scattering energies. An analysis to directly measure parts of this background is currently being performed. Once the background is better understood, the uncertainty in the dilution due to the background can be more accurately estimated. Estimates based on simulations and measurements taken by other experiments at similar kinematics are offered in section 6.2.6.

The model of $R(W, Q^2)$ (see section 6.1.1 and Ref. [61]) used in the calculation of the unpolarized cross section adds an additional uncertainty of 1.5%.

The elastic tail subtraction contributes another 1.5% uncertainty to the asymmetry.

7.2 A_1 Results

The runs selected for analysis are shown in Figs. 7.1 - 7.4. These plots show the count asymmetry for each run with corrections for livetime, charge, and beam and target polarization. On a run-by-run basis the asymmetries exhibit a statistical fluctuation about the mean. The by-run asymmetries were used to check for systematic consistency and proper application of the corrections used to calculate the electron asymmetry from the count asymmetry. Most notably, larger than expected fluctuations or trends in the asymmetry over a series of runs indicated target polarization analysis problems and livetime helicity misassignment, which were immediately corrected.

As described in the previous section, the events from the runs are separated and binned by their kinematics. The asymmetries binned in x and Q^2 for these data sets are shown in Figs. 7.5 - 7.8. These are the DIS electron asymmetries, A_{180° and A_{80°,

used to calculate the virtual Compton asymmetry A_1.

Combining the data sets to form the virtual Compton asymmetry yields the results shown in Fig. 7.9. In the plot, color distinguishes which Q^2 bin the data belongs to. The results in Fig. 7.9 are decomposed into contributions from $A_{\parallel}$ asymmetry and $A_{\perp}$, and shown in Fig. 7.10. The contribution from the term originating from the perpendicular asymmetry remains below 10% of the parallel asymmetry term for almost all of the SANE data. A band at the bottom of the plot shows the parallel to perpendicular asymmetry ratio, with a line at the perpendicular constribution's 10% point.

The results of this experiment are plotted alongside the world's data in Fig. 7.11 The current stage of the analysis is enough to suggest that SANE's data are consistent with previous measurements. The systematic errors discussed in section 7.1 are shown as an orange band on the plot. It amounts to about 6% relative error on A_1. In addition to this error, there is an uncertainty associated with the background dilution and the background asymmetry, discussed in section 6.2.6. Assuming that the background and its asymmetry can be estimated as given in that section, the additive correction that would need to be applied to A_1 is shown as a pink band behind the systematic error band. A discussion of the results follows.

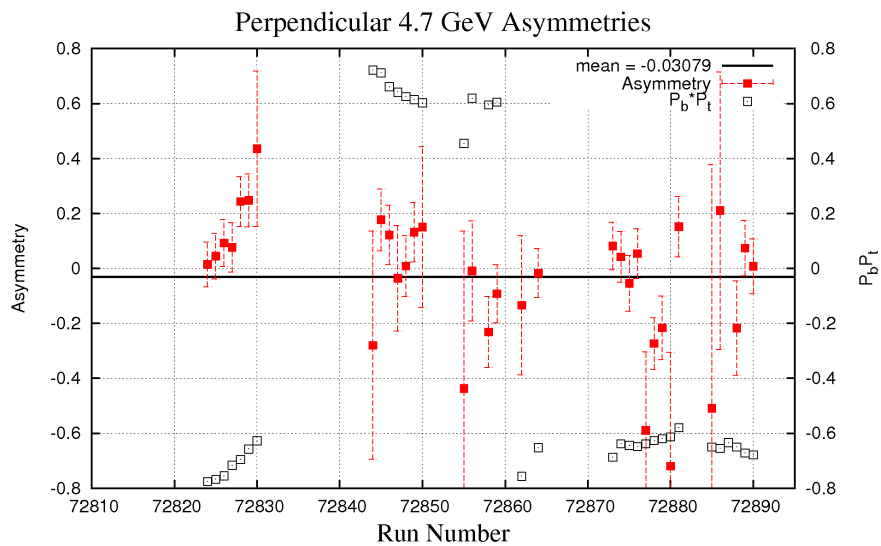

Figure 7.1: Count asymmetries for each run. The mean is noted in the legend. This plot is from the near-perpendicular 4.7GeV beam energy data set. The product P_bP_t is also plotted. Error bars are statistical.

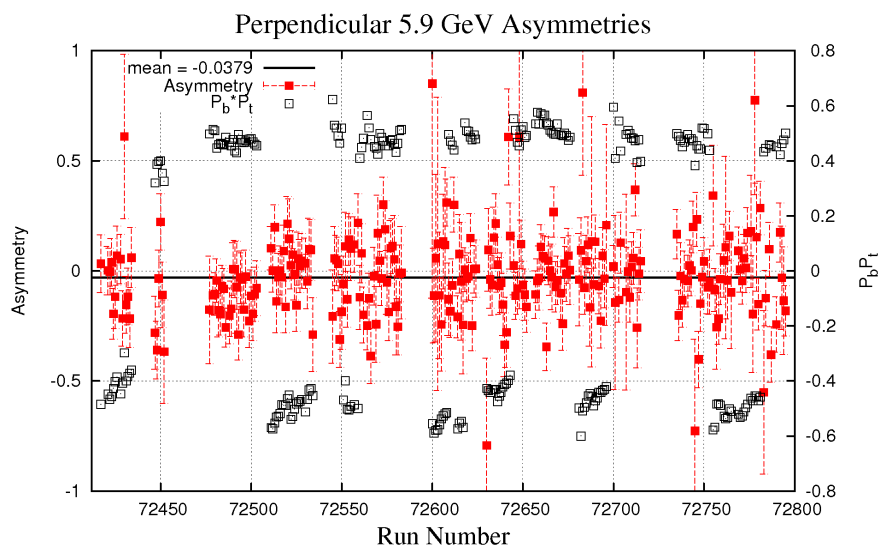

Figure 7.2: Count asymmetries for each run. The mean is noted in the legend. This plot is from the near-perpendicular 5.9GeV beam energy data set. The product P_bP_t is also plotted. Error bars are statistical.

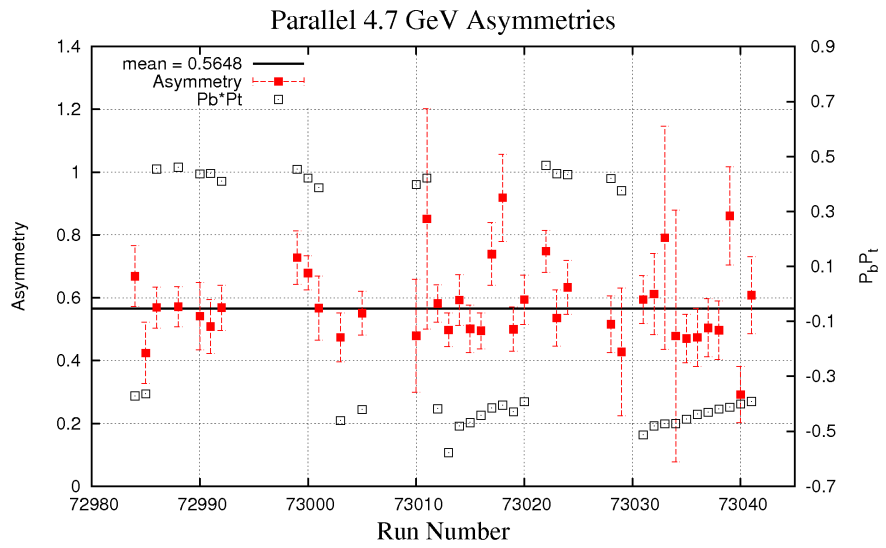

Figure 7.3: Count asymmetries for each run. The mean is noted in the legend. This plot is from the parallel 4.7GeV beam energy data set. The product P_bP_t is also plotted. Error bars are statistical.

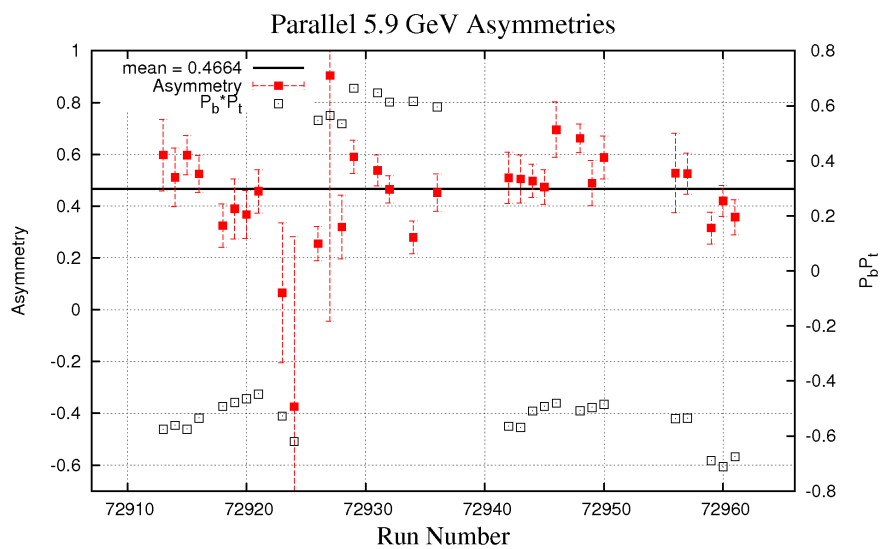

Figure 7.4: Count asymmetries for each run. The mean is noted in the legend. This plot is from the parallel 5.9GeV beam energy data set. The product P_bP_t is also plotted. Error bars are statistical.

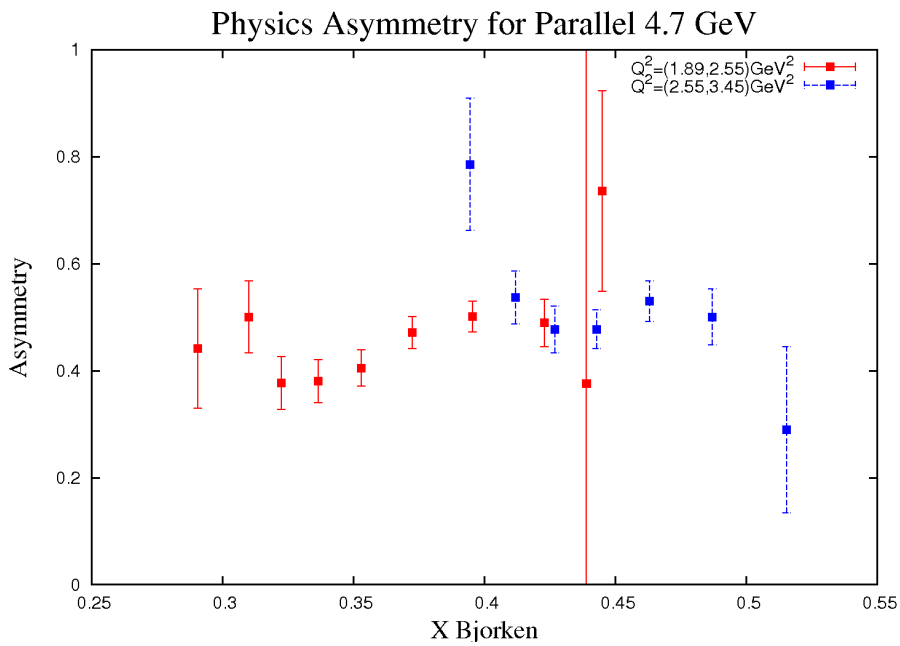

Figure 7.5: The run averaged physics asymmetries binned in x and Q^2. The target orientation is anti parallel to the beam, and the beam energy is 4.7GeV. Error bars are statistical.

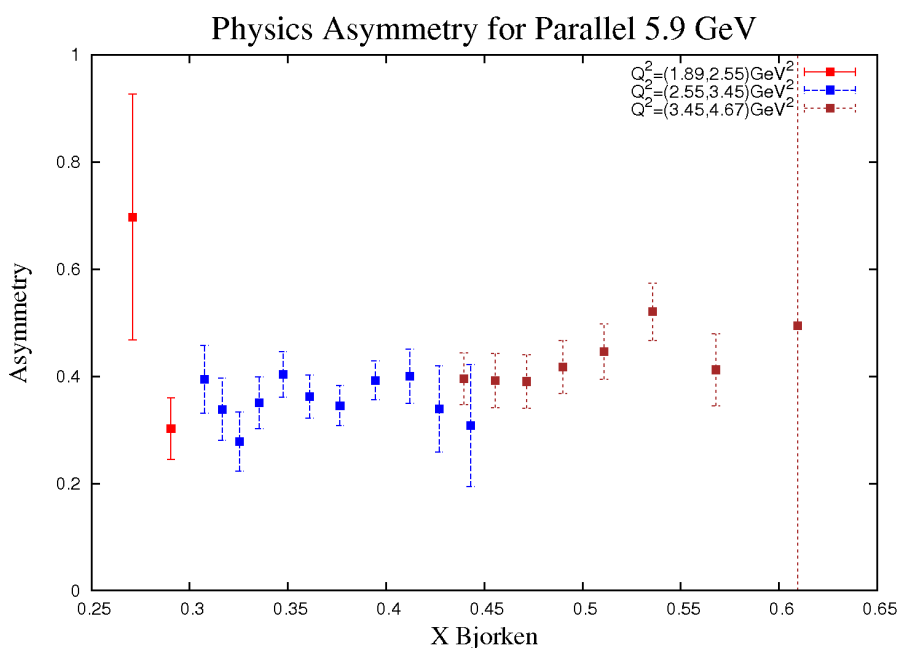

Figure 7.6: The run averaged physics asymmetries binned in x and Q^2. The target orientation is anti parallel to the beam, and the beam energy is 5.9GeV. Error bars are statistical.

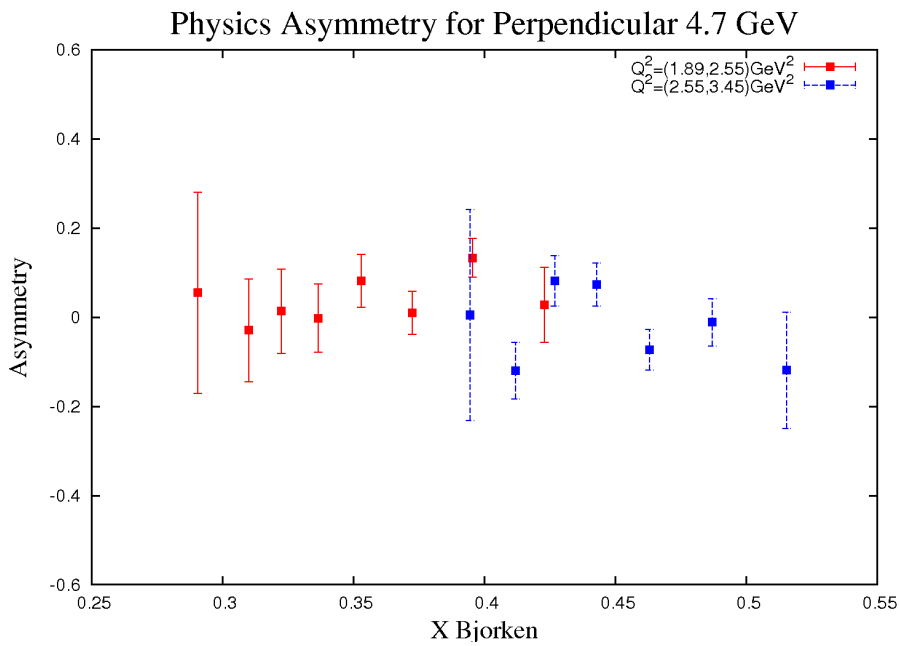

Figure 7.7: The run averaged physics asymmetries binned in x and Q^2. The target orientation is anti perpendicular to the beam, and the beam energy is 4.7GeV. Error bars are statistical.

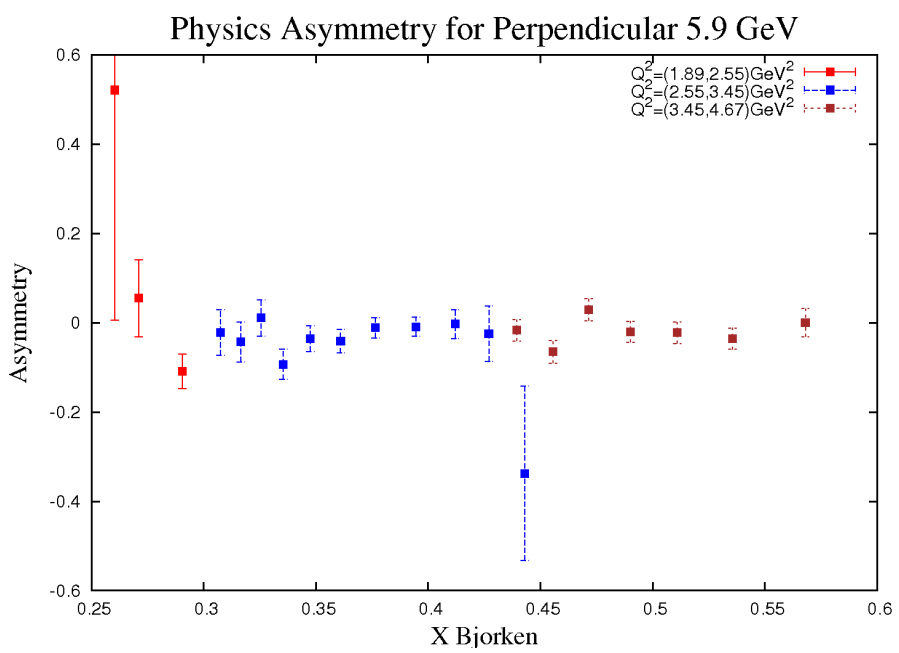

Figure 7.8: The run averaged physics asymmetries binned in x and Q^2. The target orientation is anti perpendicular to the beam, and the beam energy is 5.9GeV. Error bars are statistical.

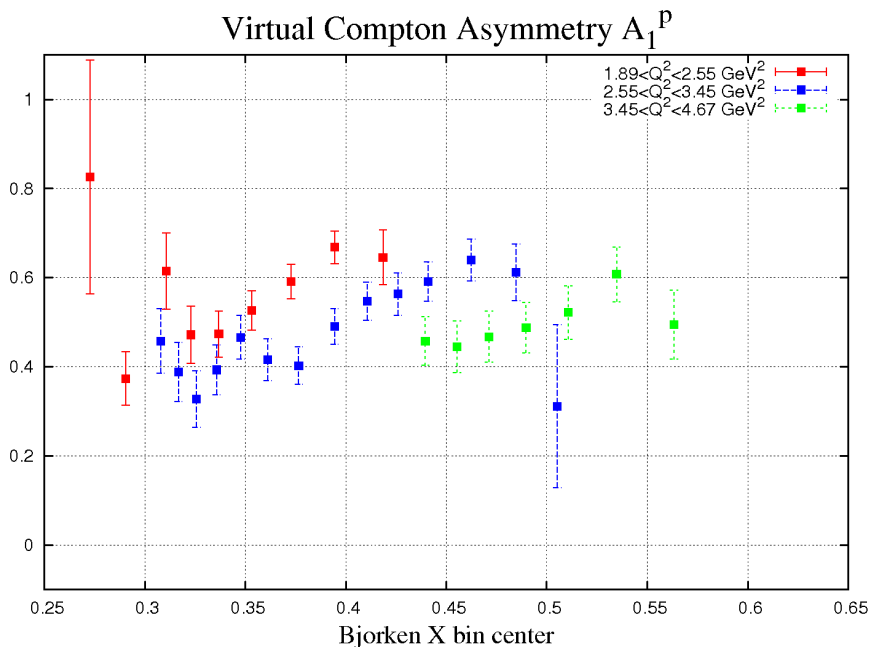

Figure 7.9: Virtual Compton asymmetry A_1 separated by color into Q^2 ranges.

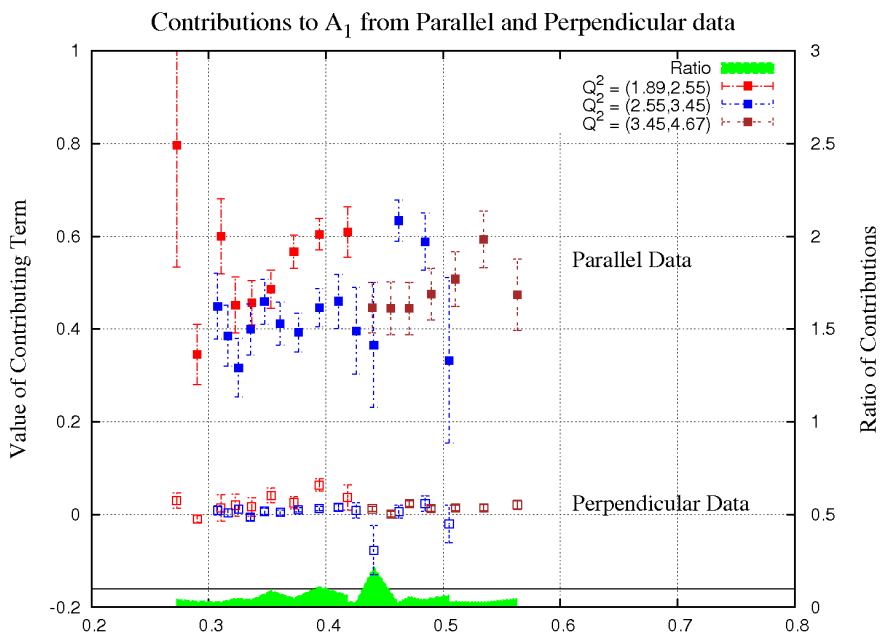

Figure 7.10: Contributing terms to A_1 from the parallel and perpendicular proton asymmetries. The solid squares are the values of the term due to the parallel asymmetries, and the open squares are those due to the perpendicular asymmetries. The absolute value of the ratio of the two terms is shown on the bottom as a filled curve. A line is drawn where the ratio would reach 10%.

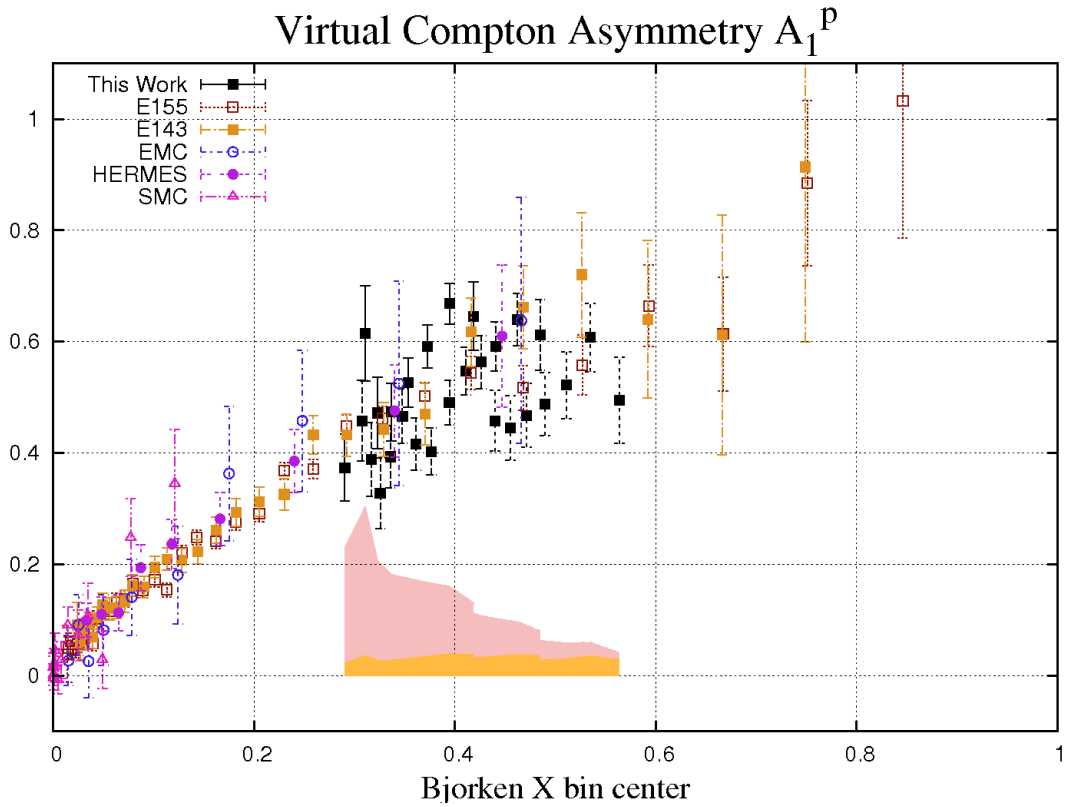

Figure 7.11: Result from this work alongside the world's data for A_1 (CLAS g_1/F_1 measurements excluded). Systematic uncertainty is shown as an orange band at the bottom of the plot. The pink band is an estimate of the correction to the A_1 value due to the positron background: see section 6.2.6 for details.

7.3 Discussion

The results in Fig 7.9 display display a wide variation in A_1 values for similar values of x. This can be traced back to the disparate plots in Figs 7.5 and 7.6, which show the parallel asymmetries for the different beam energy data sets. It is possible to reconcile these two data sets by applying a pion background that is dependent on ν rather than E', as described in section 6.2.6. That is, the exponent in Eq 6.41 becomes $-2.442\times(5.7\text{GeV}-\nu)$. Applying a correction of this form yields the A_1 values shown in Fig 7.12. While applying a correction of this form produces a compelling

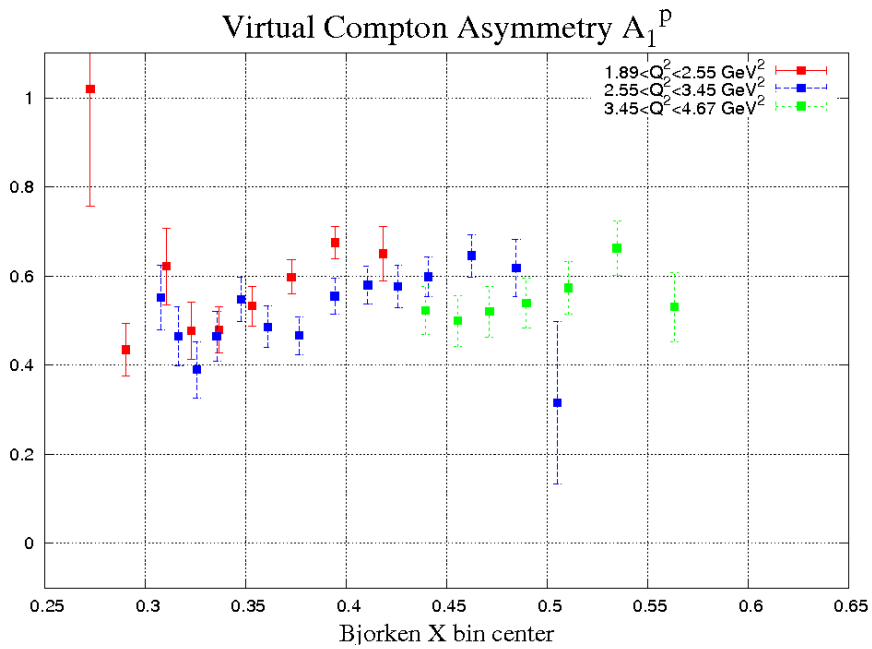

Figure 7.12: Results with a *nu* dependent background dilution corrections. Compare to Fig 7.9, which has no background correction applied.

reconcilliation of the data sets from the different beam energies (which improves if one uses a larger background than given in section 6.2.6), not very much work has been done to justify this. More investigation into the CLAS measurement of the positron background is needed. It is unclear whether the quoted E' dependence was measured at only one beam energy or two (in which case the correction would be E' and not ν

dependent). Very preliminary work on extracting background from the SANE data has also suggested a scattering angle dependence in the background events. A careful study of the background has to be completed before the collaboration is capable of quoting results with good accuracy.

The ultimate goal of this analysis is to find better constraints on $A_1(x)$ as $x \to 1$. To this end we will adopt as an empirical model of $A_1(x)$ the function

$$A_1^{\text{emp}}(x) = x^a(b + cx^2), \tag{7.1}$$

where a, b, and c are parameters to be deterimined by a fit to the data. Refer to Fig. 7.13 and its caption to see the results of the fit. The preliminary results for the SANE A_1 analysis are mostly consistent within error with the world data. A fit of $A_1^{\text{emp}}(x)$ was performed both to the world data alone as well as to the world data with SANE's preliminary results included. The SANE preliminary results have a rather flat trend compared to the world data, and consequently predict a lower $A(x \to 1)$ value.

These results are very preliminary, and the fit is performed on data to which an untested background correction has been applied. Once the analysis is finished, the results from this work will play a significant role in distinguishing between different quark interaction models. For example, should the trend of the SANE results persist in the final analysis as they do in 7.13, it would seem unlikely that the PQCD prediction is correct. However, it is not possible to make that distinction at the current stage of the analysis.

Accurate background corrections and better dilution factors are being worked on currently. Internal radiative corrections and corrections to the inelastic spectrum are still pending. Once the effects of these corrections are well understood, the neighboring x bins may be combined for better statistical precision.

While preliminary, the results shown here are an indication that experiment was

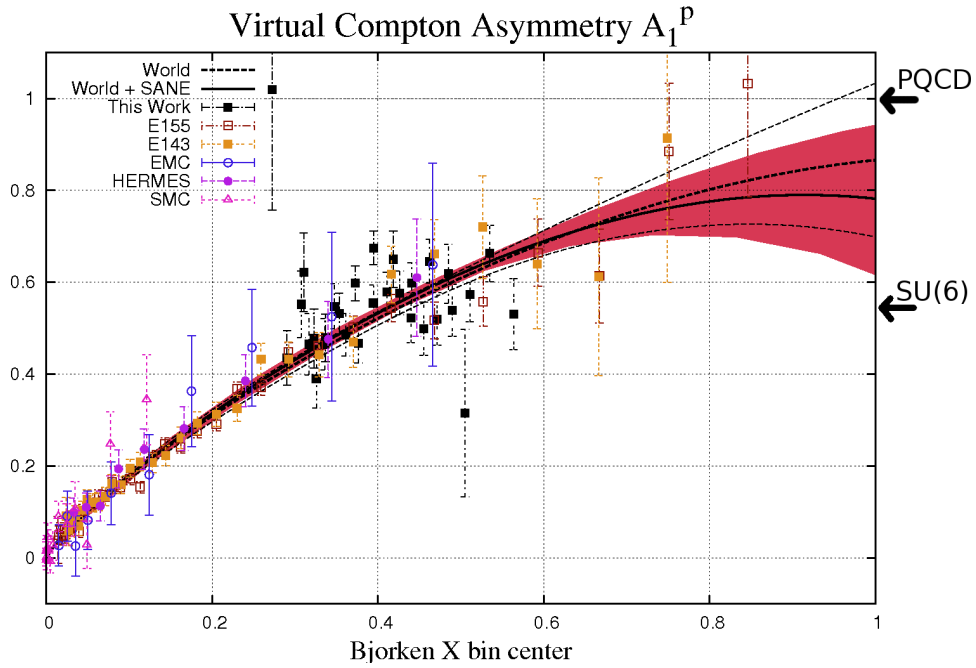

Figure 7.13: SANE preliminary results alongside other A_1 measurements. The preliminary background corrections have been applied. A fit of the form $A_1(x) = x^a(b+cx^2)$ was made to the world data shown and to the world data and SANE inclusive. Dashed lines indicate the world fit, the thin dashed lines marking the upper and lower error to the fit. The solid line shows the fit to the SANE and world data with the error depicted as a red band.

a success. The detector package used was unique and mandated a completely novel approach to the analysis. The presence of a strong target field provided additional challenges. The experiment was able to gather data over a wide kinematic range in a span of time far shorter than that possible had a magnetic spectrometer had been used. The collection of perpendicular target polarization data not only allows for a true measurement of A_1, but it also allows the extraction of the sparsely measured spin structure function g_2. This has significant implications for the study of the role of QCD in DIS. The coverage of the DIS portion of the experiment analyzed here will be extended using the resonance data. Using duality, the average results for A_1 in the resonances can be used to extend the measurement of the DIS A_1 values in Bjorken x.

Furthermore, a more precise knowledge of A_1 at high x is crucial to the understanding of the polarized parton densities [9] [62]. There are perturbative QCD models that predict the value $A_1(x = 1)$ [12] [13] , and models that use the presumed value of $A_1(x = 1)$ as a parameter [25]. Relevant $A_1(x = 1)$ values are shown for two models in 7.13. All of the groups in this field will benefit from the constraints on high x values of A_1 that this analysis will provide.

Appendix A

Target Lifetimes

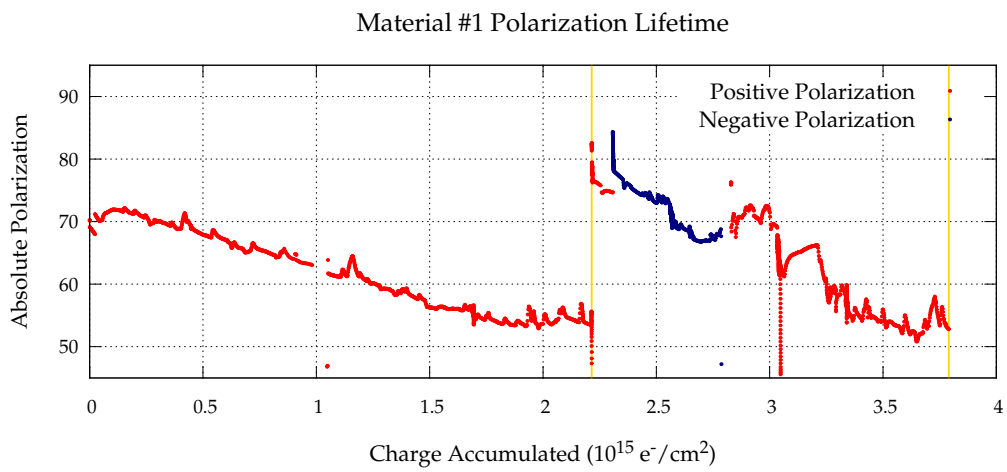

Figure A.1: Target Load 1 lifespan. Shown is the offline calculated polarization as a function of incident beam charge on the target. Anneals are marked with yellow vertical bars.

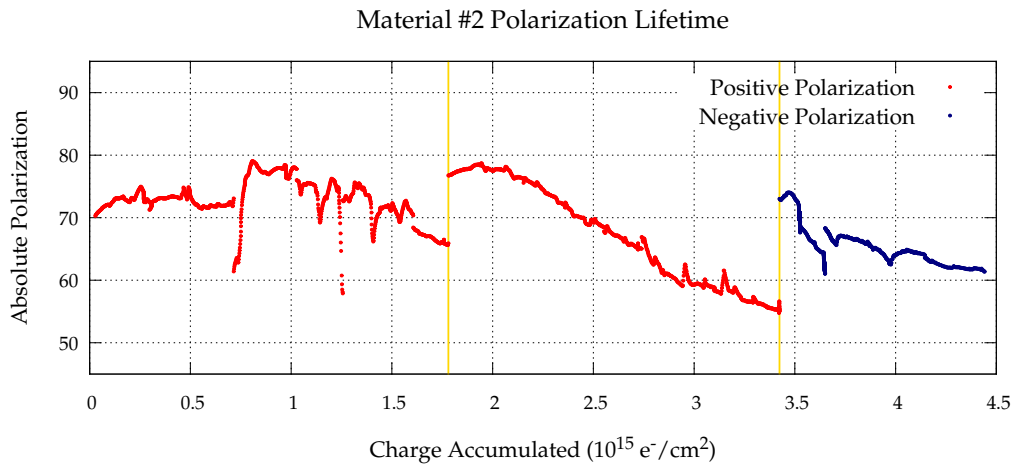

Figure A.2: Target Load 2 lifespan. Shown is the offline calculated polarization as a function of incident beam charge on the target. Anneals are marked with yellow vertical bars.

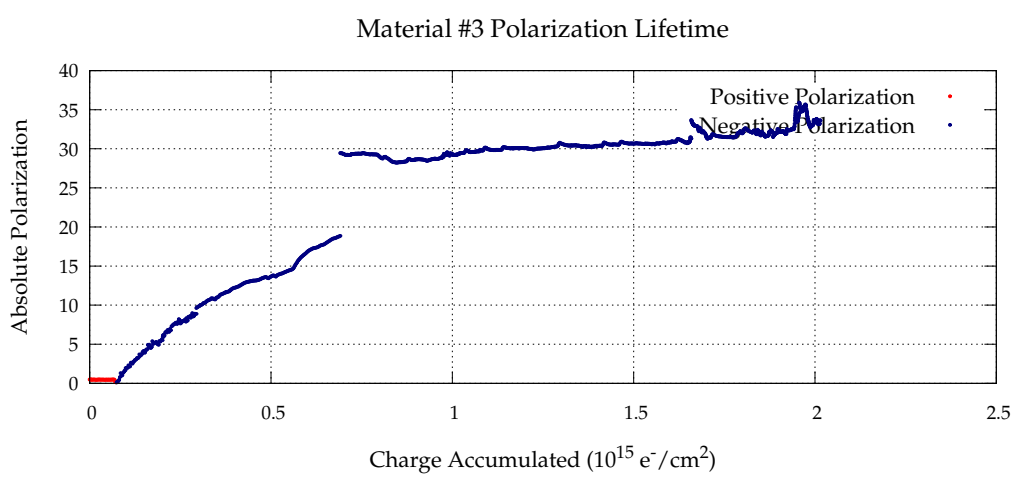

Figure A.3: Target Load 3 lifespan. Shown is the offline calculated polarization as a function of incident beam charge on the target. Anneals are marked with yellow vertical bars.

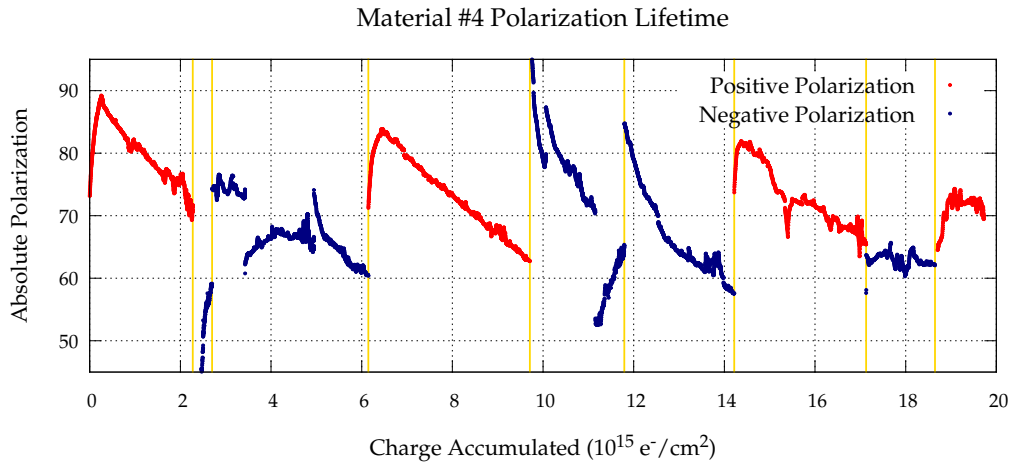

Figure A.4: Target Load 4 lifespan. Shown is the offline calculated polarization as a function of incident beam charge on the target. Anneals are marked with yellow vertical bars.

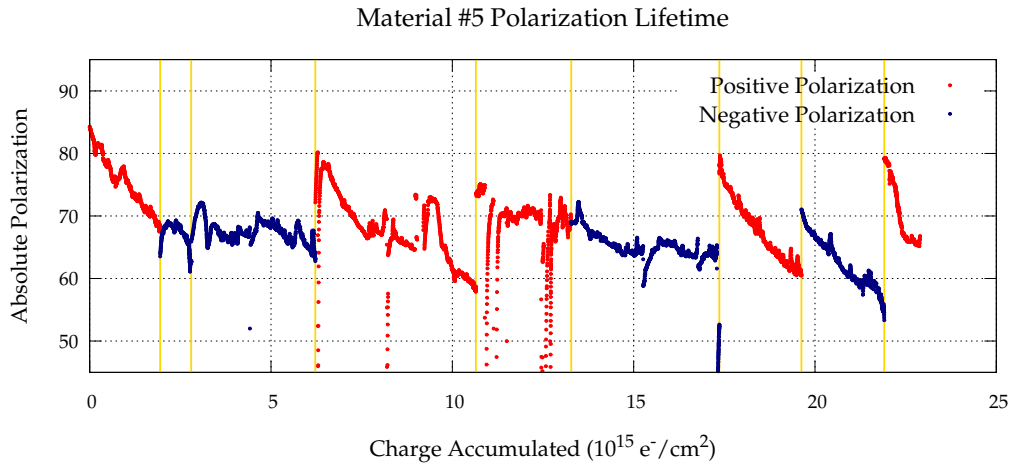

Figure A.5: Target Load 5 lifespan. Shown is the offline calculated polarization as a function of incident beam charge on the target. Anneals are marked with yellow vertical bars.

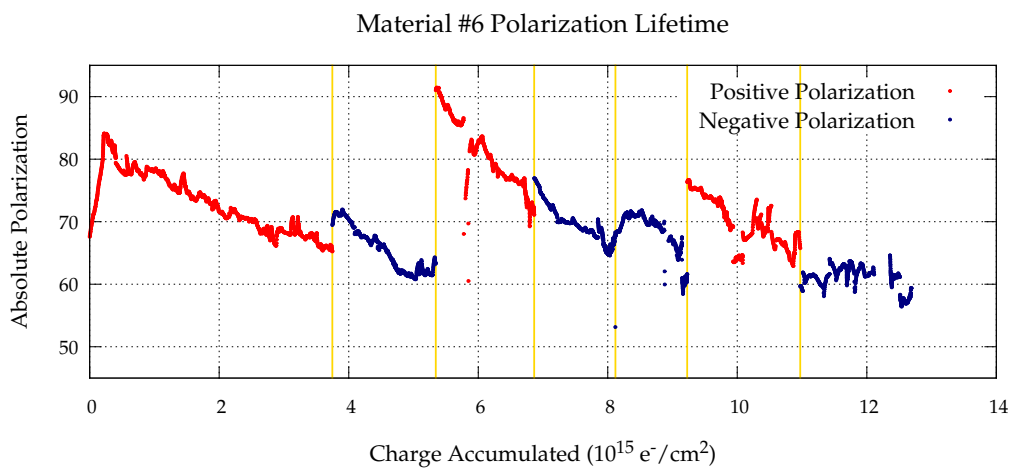

Figure A.6: Target Load 6 lifespan. Shown is the offline calculated polarization as a function of incident beam charge on the target. Anneals are marked with yellow vertical bars.

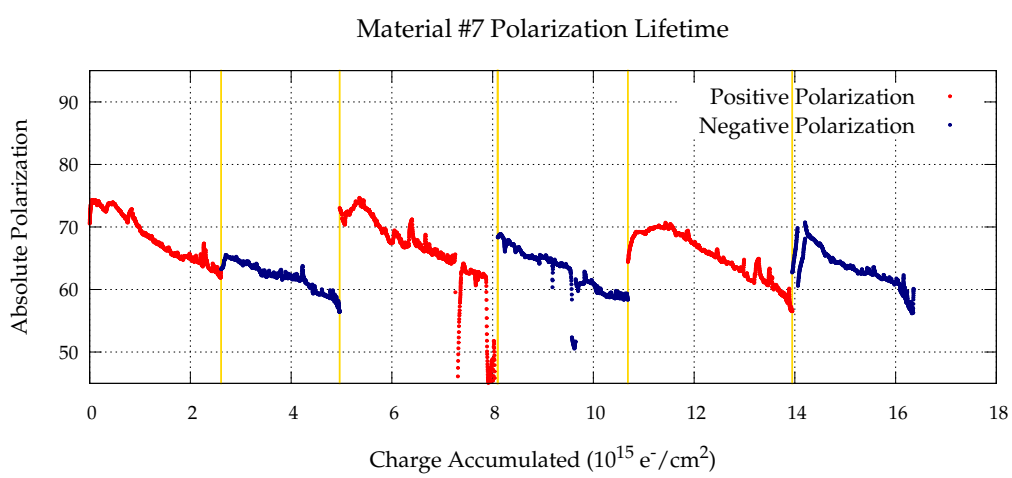

Figure A.7: Target Load 7 lifespan. Shown is the offline calculated polarization as a function of incident beam charge on the target. Anneals are marked with yellow vertical bars.

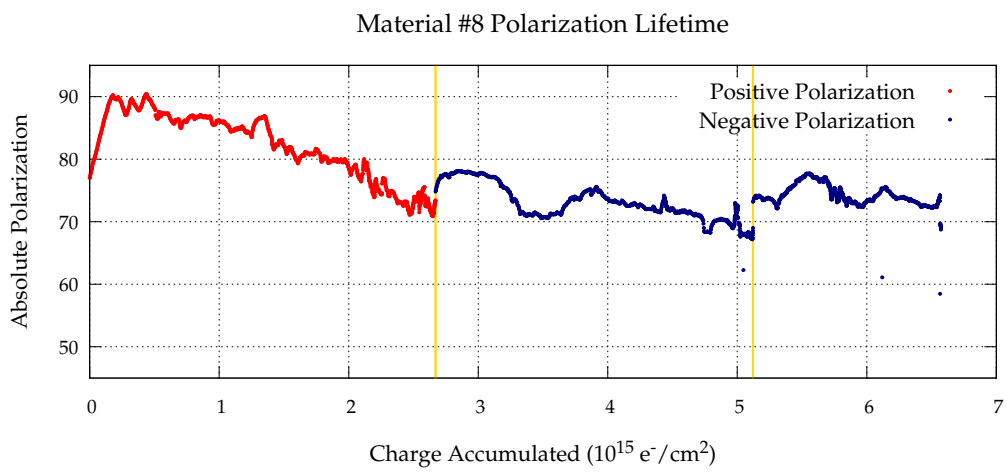

Figure A.8: Target Load 8 lifespan. Shown is the offline calculated polarization as a function of incident beam charge on the target. Anneals are marked with yellow vertical bars.

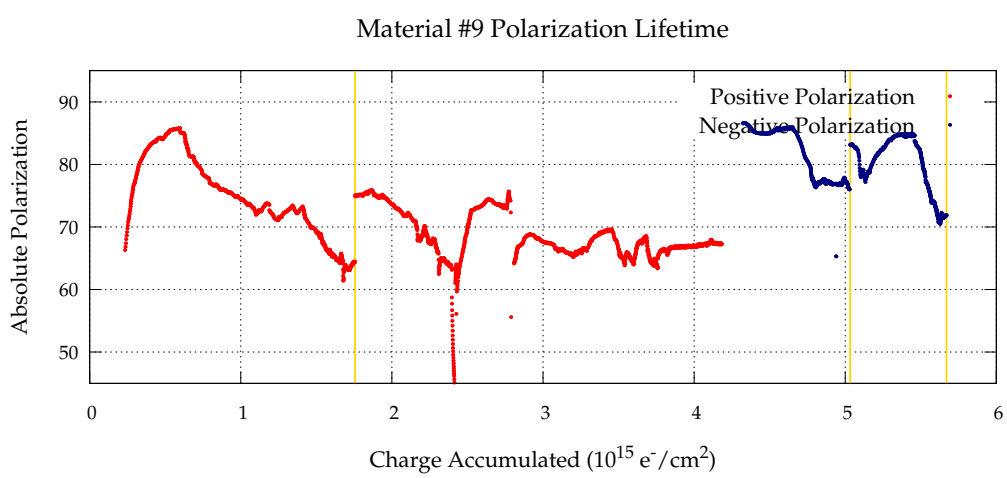

Figure A.9: Target Load 9 lifespan. Shown is the offline calculated polarization as a function of incident beam charge on the target. Anneals are marked with yellow vertical bars.

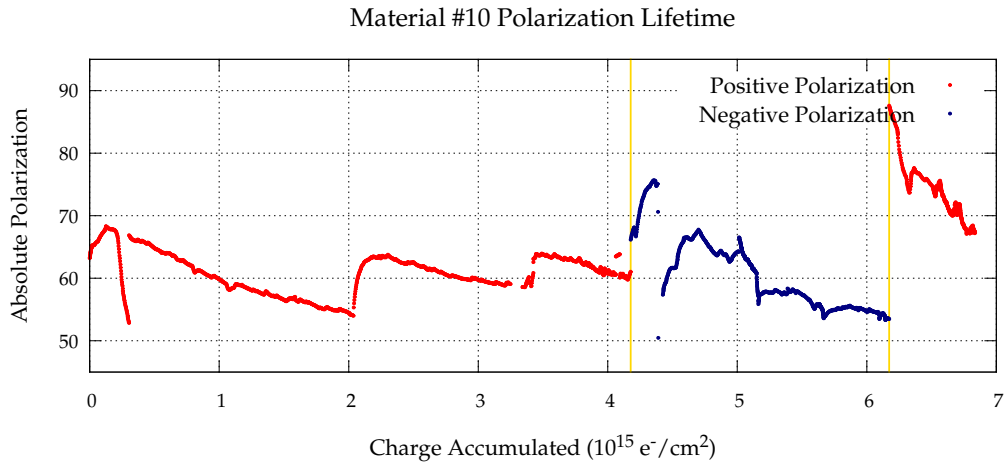

Figure A.10: Target Load 10 lifespan. Shown is the offline calculated polarization as a function of incident beam charge on the target. Anneals are marked with yellow vertical bars.

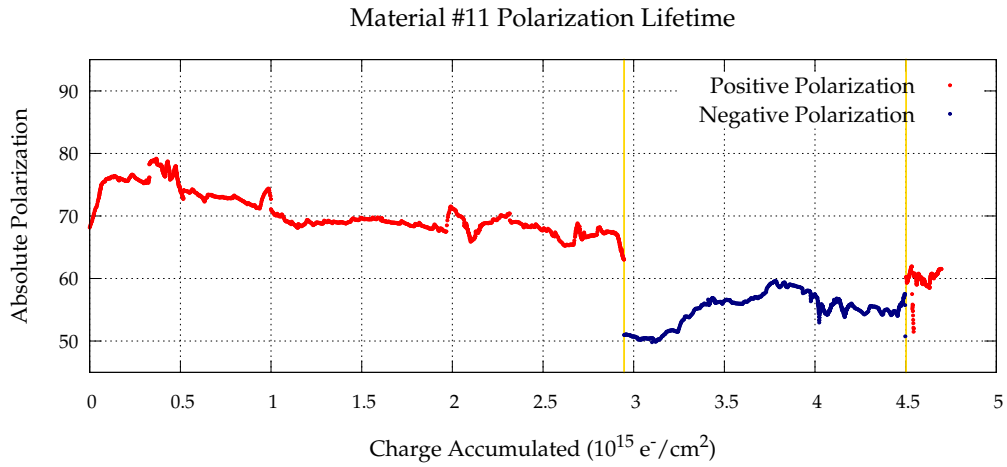

Figure A.11: Target Load 11 lifespan. Shown is the offline calculated polarization as a function of incident beam charge on the target. Anneals are marked with yellow vertical bars.

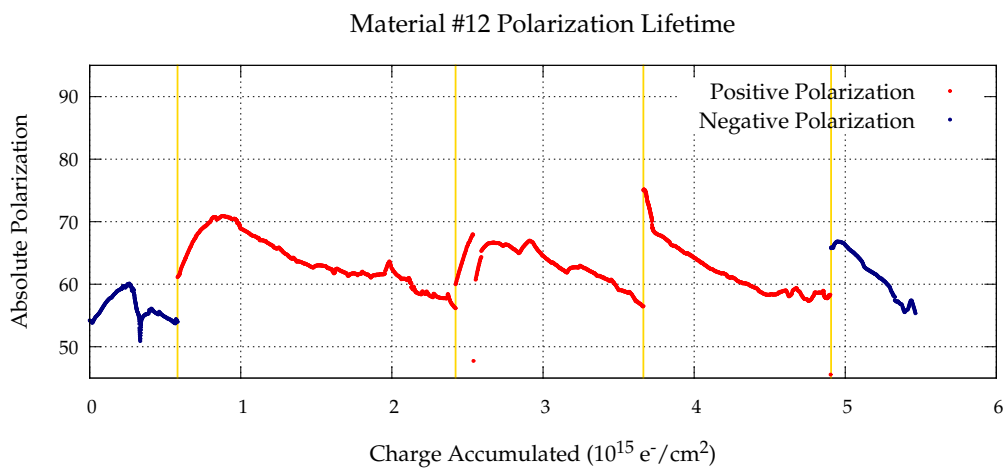

Figure A.12: Target Load 12 lifespan. Shown is the offline calculated polarization as a function of incident beam charge on the target. Anneals are marked with yellow vertical bars.

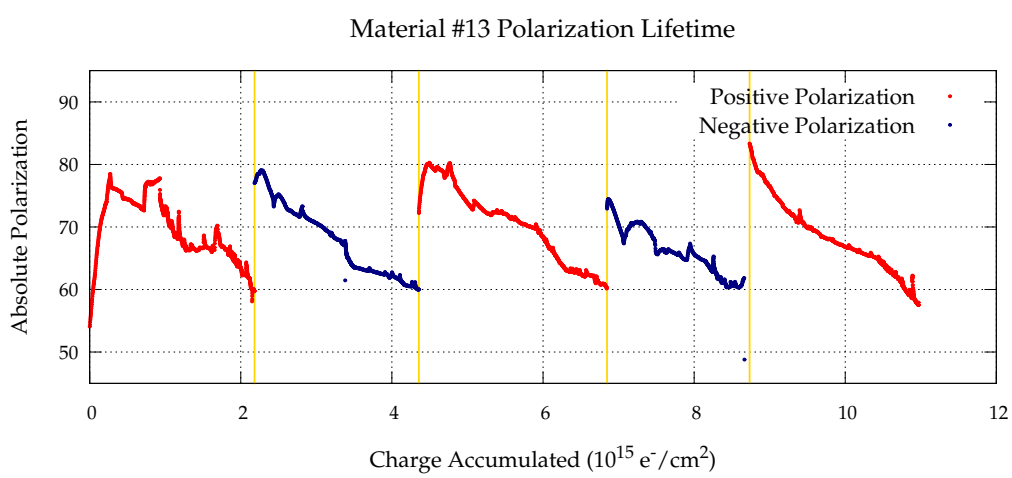

Figure A.13: Target Load 13 lifespan. Shown is the offline calculated polarization as a function of incident beam charge on the target. Anneals are marked with yellow vertical bars.

Bibliography

[1] D.G. Crabb and W. Meyer. Solid polarized targets for nuclear and particle physics experiments. *Annual Review of Nuclear and Particle Science*, 47:67–109, 1997.

[2] K. Nakamura *et al* (Particle Data Group). PDG Reviews and Summary Tables. *J. Phys.*, G:075021, 2010.

[3] A. Bodek and J. L. Ritchie. Fermi Motion Effects in Deep Inelastic Lepton Scattering from Nuclear Targets. *Phys. Rev.*, D23:1070, 1981.

[4] W. Greiner. *Quantum Chromodynamics*. Springer, 2007.

[5] M. Peksin and D. Schroeder. *An Introduction to Quantum Field Theory*. Westview Press, 1995.

[6] J. D. Bjorken. Asymptotic sum rules at infinite momentum. *Phys. Rev.*, 179:1547–1553, Mar 1969.

[7] R. L. Jaffe. Deep inelastic scattering with application to nuclear targets. Technical Report CTP-1261. MIT-CTP-1261, Cambridge, MA, Jul 1985.

[8] E. Leader and E. Predazzi. *An introduction to gauge theories and modern particle phsyics*. Cambridge University Press, 1996.

[9] E. Leader, A. Sidorov, and D. B. Stamenov. Longitudinal polarized parton densities updated. *Phys. Rev. D*, 73:034023, Feb 2006.

[10] A. Accardi *et al.* Uncertainties in determining parton distributions at large x. *Phys. Rev. D*, 84:014008, Jul 2011.

[11] M. Anselmino, A. Efremov, and E. Leader. The theory and phenomenology of polarized deep inelastic scattering. *Physics Reports*, 261:1–124, 1995.

[12] S. J. Brodsky, M. Burkhardt, and I. Schmidt. QCD constraints on the shape of quark and gluon distributions. *Nuclear Physics B*, 441:197–214, 1995.

[13] G. Farrar and D. Jackson. Pion and nucleon structure functions near $x = 1$. *Phys. Rev. Lett.*, 35:1416–1419, 1975.

[14] J. Gunion, P. Nason, and R. Blankenbecler. Power-suppressed contributions to deep-inelastic processes. *Phys. Rev. D*, 29:2491–2511, 1984.

[15] J. Ashman *et al.* An investigation of the spin structure of the proton in deep inelastic scattering of polarised muons on polarised protons. *Nuclear Physics B*, 328(1):1–35, 1989.

[16] A. Airapetian *et al.* Quark helicity distributions in the nucleon for up, down, and strange quarks from semi-inclusive deep-inelastic scattering. *Phys. Rev. D*, 71(1):012003, Jan 2005.

[17] K. V. Dharmawardane *et al.* Measurement of the x- and q^2-dependence of the asymmetry A_1 on the nucleon. *Physics Letters B*, 641(1):11–17, 2006.

[18] A. Airapetian *et al.* Evidence for quark-hadron duality in the proton spin asymmetry A_1. *Phys. Rev. Lett.*, 90(9):092002, Mar 2003.

[19] K. Abe *et al.* Measurements of the proton and deuteron spin structure functions g_1 and g_2. *Phys. Rev. D*, 58(11):112003, Oct 1998.

[20] B. Adeva *et al.* Spin asymmetries A_1 of the proton and the deuteron in the low x and low q^2 region from polarized high energy muon scattering. *Phys. Rev. D*, 60(7):072004, Sep 1999.

[21] K. Abe *et al.* Measurement of the neutron spin structure function g_n^2 and asymmetry A_n^2. *Physics Letters B*, 404(3-4):377–382, 1997.

[22] K. Abe et. al. Measurements of the proton and deuteron spin structure function g_2 and asymmetry A_2. *Phys. Rev. Lett.*, 76(4):587–591, Jan 1996.

[23] F. R. Wesselmann *et al.* Proton spin structure in the resonance region. *Phys. Rev. Lett.*, 98:132003, Mar 2007.

[24] O. A. Rondon. The spin structure of the nucleon measured in slac experiment 155. *Nuclear Physics A*, 663-664:293–296, 2000.

[25] N. Isgur. Valence quark spin distribution functions. *Phys. Rev. D*, 59(3):034013, Jan 1999.

[26] B. Adeva *et al.* The spin-dependent structure function $g_1(x)$ of the proton from polarized deep-inelastic muon scattering. *Physics Letters B*, 412(3-4):414–424, 1997.

[27] J. Ashman *et al.* A measurement of the spin asymmetry and determination of the structure function g_1 in deep inelastic muon-proton scattering. *Physics Letters B*, 206(2):364 – 370, 1988.

[28] Jefferson Lab Hall B CLAS collaboration. `http://clasweb.jlab.org/physicsdb/intro.html`.

[29] A.C. Benvenuti *et al.* A high statistics measurement of the deuteron structure functions $F_2(x, Q^2)$ and R from deep inelastic muon scattering at high Q^2. *Physics Letters B*, 237(3-4):592 – 598, 1990.

[30] P. Amaudruz *et al.* The ratio F_2^n/F_2^p in deep inelastic muon scattering. *Nuclear Physics B*, 371(1-2):3 – 31, 1992.

[31] M. Arneodo *et al.* Reevaluation of the gottfried sum. *Phys. Rev. D*, 50:R1–R3, Jul 1994.

[32] J. Maxwell. *Probing Proton Spin Structure: A measurement of g^2 at four momentum transfer of 2 to 6 GeV^2*. PhD thesis, UVA, 2010.

[33] C. Hernandez-Garcia, P.G. O'Shea, and M. L. Stutzman. Electron sources for accelerators. *Physics Today*, 61:44–49, 2008.

[34] K.B. Unser. The parametric current transformer, a beam current monitor developed for lep. *A.I.P. Conference Procedings*, 252:266, 1992.

[35] C. Yan et. al. Superharp – a wire scanner with absolute position readout for beam energy measurement at cebaf. *Nuclear Instruments and Methods in Physics Research Section A: Accelerators, Spectrometers, Detectors and Associated Equipment*, 365(2-3):261 – 267, 1995.

[36] P. Gueye. Status of the actual beam position monitors in the Hall C beamline. Technical report, Jefferson Lab Hall, 1994.

[37] C. Yan, R. Carlini, and D. Neuffer. Beam energy measurements using the arc beam line as a spectrometer. Technical Report TN 93-004, Jeffereson Lab, 1993.

[38] M. Hauger et. al. A high-precision polarimeter. *Nuclear Instruments and Methods in Physics Research Section A: Accelerators,Spectrometers,Detectors and Associated Equipment*, 462(3):382 – 392, 2001.

[39] D. Gaskell and J. Maxwell. `https://hallcweb.jlab.org/experiments/sane/wiki/index.php/Moller_Polarimeter`.

[40] Chen Yan. Slow raster system for polarized target experiments. Technical Report Hall C User How To, Sane Tech Note March 6, Jefferson Lab.

[41] Insert creation. UVA Solid Polarized Target Group Internal Documentation.

[42] J.D. Maxwell. Radiation damage and recover in polarized $^{14}NH_3$ ammonia targets at jefferson lab. In *Polarized Sources, Targets, and Polarimetry Proc. of the 13th Int. Workshop*, pages 146–153, 2009.

[43] Ed Jastrzembski. Trigger supervisor version 2. Technical report, Jefferson Lab, 2009. Unpublished JLab Data Acqusition Group Document.

[44] J. Arrington. *Inclusive electron scattering from nuclei at $x > 1$ and high Q^2*. PhD thesis, Caltech, 1998.

[45] R. Fernow. *Introduction to experimental physics*. Cambridge University Press, 1986.

[46] GEP III collaboration. Jefferson lab gep iii wiki. access can be obtained by contacting the collab.

[47] A. Puckett. *Recoil Polarization Measurements of the Proton Electromagnetic Form Factor Ratio to High Momentum Transfer*. PhD thesis, MIT, 2010.

[48] V. Breton *et al.* Application of neural networks and cellular automata to interpretation of calorimeter data. *Nuclear Instruments and Methods in Physics Research Section A: Accelerators, Spectrometers, Detectors and Associated Equipment*, 362(2-3):478 – 486, 1995.

[49] R. Rojas. *Neural Networks a Systematic Introduction*. Springer, 1996. `http://page.mi.fu-berlin.de/rojas/neural/index.html`.

[50] D. Crabb, D. Day, and O. Rondon. A proposal for the renewal of contract no de-fg02-96er40950. University of Virginia.

[51] R. T. Jones *et al.* A bootstrap method for gain calibration and resolution determination of a lead-glass calorimeter. *Nuclear Instruments and Methods*, 566:366–374, 2006.

[52] R. Roberts. *The Structure of the Proton.* Cambridge University Press, 1990.

[53] SANE Collaboration. Livetime analysis page. `https://hallcweb.jlab.org/experiments/sane/wiki/index.php/Deadtime`.

[54] L. W. Mo and Y. S. Tsai. Radiative corrections to elastic and inelastic *ep* and *up* scattering. *Rev. Mod. Phys.*, 41(1):205–235, Jan 1969.

[55] K. Slifer. Radiative corrections to the rss elastic proton asymmetry. *technical report, University of Virginia*, 2005.

[56] S. Stein. Electron scattering at 4° with energies of 4.5-20 gev. *Phys. Rev. D*, 12(7):1884–1919, Oct 1975.

[57] A. Afanasev, I. Akushevich, and N. Merenkov. Model independent radiative corrections in processes of polarized electron-nucleon elastic scattering. *Phys. Rev. D*, 64:113009, Nov 2001.

[58] T. V. Kuchto and N. M. Shumeiko. Radiative effects in deep inelastic scattering of polarized leptons by polarized nucleons. *Nuclear Physics B*, 219(2):412 – 436, 1983.

[59] O. A. Rondon. Corrections to nucleon spin structure asymmetries measured on nuclear polarized targets. *Physical Review C*, 60:035201, 1999.

[60] L. W. Whitlow. SLAC-report-357. Stanford PhD Thesis.

[61] P. E. Bosted and M. E. Christy. Empirical fit to inelastic electron-deuteron and electron-neutron resonance region transverse cross sections. *Phys. Rev. C*, 77:065206, Jun 2008.

[62] E. Leader, A. V. Sidorov, and D. B. Stamenov. Determination of polarized parton densities from a QCD analysis of inclusive and semi-inclusive deep inelastic scattering data. *Phys. Rev. D*, 82:114018, Dec 2010.